

Dissertation
submitted to the
Combined Faculty of Natural Sciences and Mathematics
of the Ruperto Carola University Heidelberg, Germany
for the degree of
Doctor of Natural Sciences

Presented by:
Martine Ballinger (B.Sc.)
Born in: Westminster, London
Oral examination: 4th October

Establishing microfluidics-based drug screening methods to determine drug sensitivities of cancer cells.

Referees:

Prof. Dr. Benedikt Brors

Dr. Martin Jechlinger

Table of Contents

Abstract (English)	9
Abstract (German)	11
Acknowledgements	13
1. Introduction	15
Cancer	17
Properties of cancer	19
Drugs for cancer treatment	25
Drug combinations.....	28
Determining drug-sensitivity (personalized treatments).....	30
Microfluidics	35
Overview	35
Droplets: surfactant-stabilized emulsions and 3-phase plug systems	39
Transcriptomics in microfluidics	42
Cross-contamination between surfactant-stabilized droplets.....	43
Drug-screening in droplets.....	44
Aims of this work	49
2. Results	51
Evaluating feasibility of fluorescence-based cytotoxic T-lymphocyte activity screens to determine cell-specific immune checkpoint inhibitor efficacy	53
Selecting and activating primary cytotoxic T lymphocytes	54
Assays to detect activity of cytotoxic T lymphocytes on target cells	57
Outlook	62
Developing a microfluidic workflow for combinatorial drug screens on cancer cells with transcriptomic readout	63
Overview of proposed workflow.....	63
Introducing reagents into plugs	66
Chemical agents for lysis in plugs	71

qPCR to assess microfluidics workflow	73
Preliminary drug screening on K-562 cells	79
Outlook	84
3. Discussion	87
Unifying themes	89
CTL activity screens.....	89
Transcriptomic drug response workflow	90
4. Methods.....	99
Experiments with primary human cytotoxic T-lymphocytes (CTLs).....	101
Source of primary human CTLs	101
Isolation of buffy coats from whole blood	101
Isolation and activation of CD8+ T-lymphocytes	101
Flow cytometry analysis of activated CTLs.....	102
CTL activity assays.....	103
Fabrication of microfluidic chips.....	104
Photo-masks for production of molds	104
Soft-lithography for mold fabrication	104
Epoxy mold copies to ensure reproducibility of chip production	105
Preparation of PDMS membranes	106
Fabrication of PDMS chips	106
Reagents for drug screens	107
Culturing cell lines.....	107
DNA barcodes	108
Preparation of cells for plug-production.....	108
Preparation of drugs	109
Microfluidic operations.....	110
Operation of pumps and Braille Display for plug-production	110
Fluorescence measurements from plugs	111
Operation of droplet-injection chip for introduction of reagents into plugs.....	112
Extracting cDNA from plugs	113

qPCR	113
Library PCR	114
Tagmentation and sequencing.....	115
Analysis	115
Analysis of fluorescence data from plug-based experiments	115
Analysis of RNA-seq data from K-562 drug screen	116
Reaction mixtures, barcode sequences, primers and PCR programs.....	117
Cell lysis, barcode ligation and reverse transcription mixtures	117
Barcode sequences	118
Primers	119
5. Appendix.....	121
Abbreviations	121
Supplementary figures.....	122
6. References	125

Abstract (English)

Success rates of cancer treatment have continually increased as new targeted therapies have been approved and stratification of patients has developed. Much work remains however, as only 13% of US patients responded to immune checkpoint inhibitor therapies in 2018, and a mere 4.9% responded to targeted therapies. To further increase treatment success, systematic methods for quickly, cheaply and accurately determining new patient-specific drug combinations are essential. Drug combinations provide a unique opportunity to quickly develop new treatments, increase treatment efficacy and prevent relapse. This will eventually allow treatments to be chosen which reflect the complexity of the cancer itself, by targeting multiple clones or targetable aberrations within a cancer. One promising approach for more complete patient stratification is via drug-perturbation screens directly on patient cancer cells, in which patient-specific drug sensitivity is determined without requiring any biomarker information. Such screens can help doctors to choose between available treatments and could even suggest new combinations of those. In addition, data from perturbation screens are essential to build more accurate mathematical models of drug response and identify new biomarkers which indicate drug sensitivity.

One area where perturbation screens would be incredibly useful, is in the prescription of Immune Checkpoint Inhibitors (ICIs). In the first part of this thesis, work towards this goal is presented. A robust workflow was established for selection and activation of cytotoxic T-lymphocytes (CTLs), and subsequent induction of CTL-mediated target cell death. Two different methods were tested to enable quantification of CTL activity and the outlook for development of such ICI screens is discussed.

Another important focus of personalized medicine research is the development of high-throughput screens of targeted therapies with high-content readouts. Unfortunately, such approaches usually require large numbers of cells, so are incompatible with screening directly on patient cells due to the low number of cells which are typically available. Use of droplet microfluidics allows very significant reduction in volume per sample, and therefore cell numbers required. Transcriptomics is an ideal candidate for a high-content readout, as it has proven to be one of the techniques with the best predictive capacity for patient stratification. In the second part of this thesis, I build on previous work in the group which used droplet microfluidics and combinatorial DNA barcoding to identify cell line-

specific drug combinations via a transcriptomic readout. In the previous workflow, the drugs which could be used were severely limited due to exchange of hydrophobic drugs between droplets. To address this issue and bring the workflow closer to one which could feasibly be used to inform decisions made in the clinic, I adapted and integrated different microfluidic components, ensuring a robust and rapid workflow. Specifically, in order to perform experiments in plugs rather than surfactant-stabilized droplets, I further developed a microfluidic device for consistent injection of reagents into microfluidic plugs. I also identified a detergent which was compatible with plugs, as standard cell lysis agents led to cross-contamination of contents between microfluidic plugs. Next I validated the workflow by developing a qPCR-based approach for quantifying differential expression of target genes, by incorporating qPCR barcodes during reverse transcription. Finally, I ran a preliminary experiment to treat target cells in microfluidic plugs, then perform reverse transcription and sequencing to determine whether differences in gene expression could be identified in the barcoded cDNA.

Abstract (German)

Seit der Zulassung neuer, zielgerichteter Medikamente und der Etablierung von Methoden zur Patientenstratifizierung sind die Erfolgsraten der Krebsbehandlung kontinuierlich gestiegen. Dennoch sprachen 2018 nur 13 % der US-Patient*innen auf eine Immun-Checkpoint-Therapie und 4,9 % auf andere zielgerichtete Therapien an. Um den Behandlungserfolg weiter zu steigern, sind demzufolge systematische Methoden zur schnellen, kostengünstigen und genauen Bestimmung neuer patientenspezifischer Medikamentenkombinationen unerlässlich. Die Kombination verschiedener Medikamente bietet eine einzigartige Möglichkeit, schnell neue Behandlungsstrategien zu entwickeln, deren Wirksamkeit zu erhöhen und Rückfälle zu verhindern. Dies wird es schließlich ermöglichen, Behandlungen anzuwenden, die die Komplexität der Krankheit selbst widerspiegeln, indem sie auf mehrere Klone oder adressierbare Aberrationen innerhalb eines Krebses abzielen. Ein vielversprechender Ansatz für eine umfassendere Patientenstratifizierung sind Perturbation-Screens direkt an Krebszellen von Patient*innen, welche ohne Kenntnis über potentielle Biomarker möglich ist. Solche Screens können Ärzt*innen im Entscheidungsprozess bezüglich der Art der Therapie unterstützen beziehungsweise neue Ansätze für diese liefern. Langfristig werden Perturbations-Screens unerlässlich sein, um neue Biomarker zu identifizieren, die die Empfindlichkeit gegenüber Medikamenten anzeigen.

Ein potentieller Anwendungsbereich der Perturbations-Screens ist die Verschreibung von Immun-Checkpoint-Inhibitoren (ICIs). Im ersten Teil dieser Arbeit wird der Fortschritt in Bezug auf dieses Ziel vorgestellt. Es wurde ein robuster Arbeitsablauf für die Selektion und Aktivierung von zytotoxischen T-Lymphozyten (CTLs) und die anschließende Induktion des CTL-vermittelten Zielzelltodes etabliert. Es wurden zwei verschiedene Methoden zur Quantifizierung der CTL-Aktivität getestet sowie die Perspektiven für die Entwicklung solcher ICI-Screens diskutiert.

Ein weiterer Schwerpunkt der Forschung im Bereich der personalisierten Medizin ist die Entwicklung von Hochdurchsatz-Screens für zielgerichtete Therapien. Solche Ansätze benötigen in der Regel jedoch eine große Anzahl von Zellen, welche typischerweise nicht zur Verfügung steht. Die Verwendung von Tröpfchen basierter Mikrofluidik ermöglicht eine sehr deutliche Reduzierung des Volumens pro Probe und damit der benötigten Zellzahlen. Die Transkriptomik ist eine ideale Hochdurchsatz-

Analysemethode, welche bereits als eine der Techniken mit der besten Vorhersagekapazität für die Patientenstratifizierung etabliert ist. Im zweiten Teil dieser Arbeit baue ich auf früheren Arbeiten der Gruppe auf, bei denen Tröpfchen basierte Mikrofluidik und kombinatorisches DNA-Barcoding eingesetzt wurden, um zelllinienspezifische Medikamentenkombinationen über eine transkriptomische Analyse zu identifizieren. Im bisherigen Workflow waren die verwendbaren Medikamente aufgrund des Austauschs von hydrophoben Medikamenten zwischen den Tröpfchen stark eingeschränkt. Um dieses Problem zu adressieren, habe ich eine Methode für die konsistente Injektion von Reagenzien in mikrofluidische Plugs anstelle von Tensid stabilisierten Tröpfchen weiterentwickelt. Außerdem identifizierte ich ein Detergens, das mit den Plugs kompatibel ist und validierte den Arbeitsablauf durch die Entwicklung eines qPCR-basierten Ansatzes zur Quantifizierung der differentiellen Expression von Zielgenen, indem ich qPCR-Barcodes im Zuge der reversen Transkription einführte. In einem vorläufigen Experiment behandelte ich weiterhin Zielzellen in mikrofluidischen Plugs, wobei die anschließende Sequenzierung und Transkription Aufschlüsse über Unterschiede in der Genexpression in der barcodierten cDNA liefern sollte.

Acknowledgements

This thesis is the result of four years hard work and learning. It would not have been possible without all of the support I received from my excellent colleagues, friends and family.

Firstly, I would like to thank Prof. Dr. Christoph Merten for the opportunity to carry out my PhD in his group. His vision and drive have been the foundation of these projects. I sincerely appreciate that he has consistently made time to discuss this work when requested, despite starting a new group in Lausanne and always having to meet by video call. I would also like to thank my thesis advisory committee for their support and guidance: Dr. Martin Jechlinger, Prof. Dr. Benedikt Brors, Prof. Dr. Monika Wolkers and Dr. Wolfgang Huber. I am particularly grateful to Dr. Martin Jechlinger and Prof. Dr. Benedikt Brors for being part of my thesis defense committee. Prof. Dr. Monika Wolkers' kind instructions and advice were invaluable for the T-cell portion of this thesis. Dr. Wolfgang Huber and all of the Huber group were extremely generous in inviting me to their group meetings, so that I could have direct contact with a research group in Heidelberg for the last year and a half of my PhD.

I am grateful to all of the past and present members of the Merten group for their valuable input and teaching. In particular, Dr. Lukas Mathur has been extremely patient and knowledgeable. Ramesh Utharala has provided valuable microfluidic skills. Dr. Samantha Seah has been an invaluable friend and colleague who has not only taught me many things about how to do better science (including the power of organization!), but has also inspired me to be a better person.

I would next like to thank the Genomics and Flow Cytometry Core Facilities for their friendly expertise. In particular Jelena Pistolic and Dr. Jonathan Landry, your work has been invaluable. To Dr. Vladimir Benes, Dr. Diana Ordonez and Beata Ramasz, your teaching and advice have been extremely appreciated. I would also like to thank my collaborator Olga Ivanova, for rigorous analysis of sequencing data and clear explanations of bioinformatics.

Ein hertzliches schankedön to my friends in Heidelberg, especially Tim, Jakob, Rita and Lena, you are all role models in hard-work and enthusiasm. You have consistently supported me and reminded me who I strive to be. To Valentin, I cannot imagine how I would have gotten through the last year without you. You've taught me so much, you make me laugh and give me the confidence to trust myself and expect

more from myself. I'm so excited for our next steps together.

To my family, who always believe in me and encourage me to do what I love. Thanks to my parents for showing me that a job should be inspiring and exciting. And especially thanks to my brilliant sisters Isabelle and Amelia. I'm so grateful to have you in my life and to be able to laugh together even in the difficult moments.

Last, but definitely not least, thank you to all of the amazing staff at the EMBL canteen, your constant cheerfulness was always encouraging and the food was incredible!

1. Introduction

Cancer

Cancer is the collective term for diseases in which a patient's cells undergo abnormal cell growth. For cancers in solid tissues, this eventually leads to the cells spreading into other tissues of the body, and continuing to replicate there. It is this latter process, termed metastasis, which actually causes the majority of patient mortality (Fidler, 2003). The rate of cancer diagnosis worldwide is increasing, as a result of increased population, decreased mortality from other diseases and improved diagnostic approaches. For example in 2008 there were 12.7 million diagnosed cases worldwide (Ferlay et al., 2010), which increased approximately 152% to 19.3 million diagnosed cases in 2020 (Sung et al., 2021). The number of deaths only increased by 132% in this time, indicating a slight improvement in treatment. Although the number of cancer treatments has significantly increased over time, the remaining issues are that large numbers of patients either do not respond at all to treatment, or they undergo relapse and the relapsed cancer is not sensitive to the initial treatment. To overcome these issues, it is essential that treatment is better matched to each individual cancer, and that combination treatments are used.

To understand how changes to DNA sequence can lead to cancer, it is first important to summarize some basic principles of biology. The central dogma of molecular biology (Crick, 1958) is that sequences of DNA-bases (genes) are copied into sequences of messenger RNA (mRNA) via a process called transcription. Each mRNA sequence is then used to produce a protein, via a process called translation in which the order of amino acids in that protein is determined by the mRNA sequence. Specifically, each set of three base pairs (a codon), instructs the use of a particular amino acid. A protein is therefore produced (expressed) by the sequential decoding of the DNA sequence into an amino acid chain. Each protein can be folded into a particular shape based on the amino acid sequence, and in turn enact a particular function based on protein shape and the location of different charges (Alberts, 2014). Through variation in the genetic sequences making up the genome and regulation of gene expression, different proteins are made and in different amounts. Since proteins perform structural, catalytic, signaling and regulatory roles, as well as many others, this variation allows nature to produce the full breadth and complexity of different organisms.

Genetic variation occurs primarily because of mistakes (mutations) in the copying of DNA during replication of cells. If these mutations occur within the germlines (gametes) and the effect of that mutation is not lethal, then the mutations can be passed on to future offspring, where they will be present in all nucleated cells (Alberts, 2014). This process is essential for the evolution of life on earth. If instead the mutations occur in somatic cells (body cells), the mutations normally only affect a small number of cells (depending on when in the development of that organism the mutation occurred). Somatic mutations can lead to cancer if they affect the expression level or activity of particular proteins. The effects of such mutations can either be increased promotion of cell division (the affected genes become oncogenes e.g. RAS, MYC), or loss of prior restrictions to cell division (the affected genes are tumor-suppressor genes e.g. TP53, PTEN). Mutations which actively contribute to the cancerous phenotype are termed “driver mutations”. These are usually observed alongside mutations which do not confer a selective advantage: “passenger mutations” (Pon and Marra, 2015). Due to the complex redundancy of the signaling networks regulating cell division, multiple genetic alterations are needed together for neoplastic cells with increased proliferative activity to transform into malignant cancer (Martincorena et al., 2017). By the time of diagnosis of colon cancer for example, patient cancer cells have accumulated on average fifteen driver mutations (Wood et al., 2007). It was found that cancer cells have on average four driver mutations: one in an oncogene and three in tumor-suppressor genes (Davoli et al., 2013). This is in combination with various aneuploidies.

The types of genetic alterations which lead to driver mutations are diverse. The most common type of genetic alteration in human cells is a Single Nucleotide Variant (SNV), which is substitution of a single base pair (Genomes Project et al., 2012). Because some amino acids can be encoded by multiple redundant codons, it is possible to have synonymous SNVs in which a new codon doesn't actually encode a new amino acid (Ramensky et al., 2002). Changes in regions which do not encode proteins can also lead to cancer, by affecting gene expression (Khurana et al., 2016). Insertions and deletions (Indels) can affect single base pairs or larger numbers of bases. They are more likely to have significant effects because they can cause frameshifts, in which a base pair is added or removed from a codon and the reading frame is therefore shifted. This can produce premature stop codons and therefore truncated proteins, or can result in loss of function of that protein (Lin et al., 2017). On a larger scale, Structural Variations (SVs) are when more than a thousand base pairs are deleted, duplicated,

translocated (moved within the genome) or inverted (orientation changed) (Feuk et al., 2006). Translocations and inversions can affect gene expression due to the change in local regulatory environment of that gene (Rodriguez-Revena et al., 2007). The general term for these changes in genetic sequence is mutations. Aside from genetic mutations, there can also be chemical modifications to the DNA (e.g. methylation) which do not change the DNA sequence, but which affect the accessibility and expression of the targeted genes (epimutations) (Berdasco and Esteller, 2010; Wiesner et al., 2015) and changes to the number of whole or large parts of chromosomes (aneuploidies).

Properties of cancer

Despite the incredible complexity and variation in genetic and epigenetic drivers of cancer, a number of key phenotypic features are consistently found in cancerous cells, which enable their survival, proliferation and dissemination. These features were summarized in the 2000 and 2011 “Hallmarks of Cancer” papers (Hanahan and Weinberg, 2000; Hanahan and Weinberg, 2011). The six hallmarks identified in the initial “Hallmarks of Cancer” paper, and their two emerging hallmarks from 2011 are described in the following section.

Sustained proliferative signaling

Signals which normally precisely control whether and how cells undergo growth and division are deregulated in cancer cells, allowing them to proliferate in excess. This is achieved through a number of means. Some cancer cells can increase production of growth factors which they themselves can respond to (autocrine stimulation). For example, sarcomas and glioblastomas produce tumor growth factor alpha (TGF- α) (Hanahan and Weinberg, 2000). It is also possible for some cancer cells to upregulate receptors for growth factors, such that low levels of growth factor ligand still have a powerful effect (e.g. overexpression of Her2 (Moasser, 2007)). Another method is for cancer cells to induce neighboring cells to increase production of growth factors. Mutant signaling receptors can also mediate constitutive activation of one or more of the signaling pathways downstream from the growth factor receptor.

Evasion of growth suppressors

Healthy cells continually monitor genomic damage and levels of oxygen, nucleotides, glucose and growth signals. Information about these indicators of cell health is integrated by tumor-suppressors like TP53, which coordinate an appropriate response based on the severity of homeostatic failure. By having mutations in genes which coordinate these responses, cancer cells are able to disregard growth repression signals, where healthy cells would normally halt proliferation until internal signals are resolved, or even undergo programmed cell death (apoptosis). The importance of this ability to suppress proliferation is made clear by the high rates of TP53 mutation in a wide range of cancers. For instance in larynx, ovarian, head and neck, colorectal and esophageal cancers, TP53 is mutated in over 40% of cases (Olivier et al., 2010).

Resistance to cell death

Closely linked to growth suppression and often governed by TP53, normal cells should initiate apoptosis as a result of signals indicating cancerous development (Adams and Cory, 2007; Evan and Littlewood, 1998; Lowe et al., 2004). These signals include excessive DNA damage, insufficient survival factor signaling, or hyperactive signaling by certain oncogenes. Cancer cells can forgo apoptosis if they have mutated DNA-damage sensors, overexpressed survival factors, downregulated proapoptotic factors or overexpressed antiapoptotic regulators.

Replicative immortality

The number of successive growth and division cycles which normal cell lineages can undergo is limited, resulting in either cell death or senescence (a permanent state of nonproliferation). Cancer cells can undergo unlimited rounds of replication without entering either of these two states. In non-immortal cells, the ends of each chromosome are protected by sequences of random hexanucleotide repeats, termed telomeres. These progressively shorten with each cell division, thus indicating when cells have reached the limit of their replicative lifetime. Cancer cells almost all express significantly higher levels

of telomerase (Shay and Bacchetti, 1997). This is the DNA polymerase specialized in adding telomere repeats to DNA telomere ends, which allows them to replicate continuously.

Ability to induce angiogenesis

Growth of new blood vessels from the local vasculature into nearby tissues only occurs infrequently in healthy tissue (e.g. during wound healing). Many solid tumors are able to continually induce this process, termed angiogenesis, in order to ensure a greater supply of nutrients and oxygen to the growing mass. One way in which this is achieved is through increased expression of the VEGF ligand (Carmeliet, 2005), which is produced by cells requiring increased blood supply. When it binds to epithelial cells in the target vasculature, it results in growth of new blood vessels by the targeted epithelial cells.

Activation of invasion and metastasis

Cancer cells metastasize. This means that they detach from their original environment, migrate to another site, and attach and form new tumors there. This occurs through a number of different processes, many of which must occur at once. One key alteration is reduced expression of cell-cell adhesion molecules, for example E-cadherin (Birchmeier and Behrens, 1994; Hirohashi, 1998), or reduced expression of cell-to-extracellular matrix adhesion molecules. In contrast, adhesion molecules which mediate cell migration are also often upregulated in cancers. N-cadherin for example, is normally expressed only in a few contexts (e.g. by migrating neurons during embryogenesis), but is upregulated in many invasive cancers (Cavallaro and Christofori, 2004). Epithelial-mesenchymal transition (EMT) is a complex developmental program which normally only occurs during organism development, wherein epithelial cells undergo loss of Adherens Junction protein expression, together with other changes (e.g. expression of matrix-degrading enzymes). This process has been implicated as one of the key ways that cancerous epithelial cells acquire the invasive phenotype (Iwatsuki et al., 2010; Thiery, 2002).

Reprogramming energy metabolism

Counterintuitively, cancer cells often swap from producing the majority of their ATP aerobically in the mitochondria, to the less efficient, oxygen-independent method called glycolysis (Warburg, 1930). This is sometimes explained by the hypoxic environment often present in the center of a tumor, but this effect is also observed in cancer cells receiving normal levels of oxygen. This results in an increased glucose requirement and uptake by cancer cells, often via upregulation of the GLUT1 glucose transporter (DeBerardinis et al., 2008; Hsu and Sabatini, 2008). One explanation for the advantage gained by pursuing this type of metabolism, is that this allows cancer cells to meet the increased requirement for production of macromolecules (Vander Heiden et al., 2009; VR, 1958). In addition to ATP, rapidly dividing cells require nucleosides and amino acids, which can be produced from the glycolytic intermediates produced by glycolysis.

Evading immune destruction

The role of the immune system in preventing the development of cancer is complex and not yet fully understood. Patients with high rates of cytotoxic T-lymphocyte (CTL) or Natural Killer (NK) cell infiltration into their colon or ovarian tumors tend to have a better prognosis than those without (Nelson, 2008; Pages et al., 2010). A large body of work, mostly in mice, led to the conclusion that cells can usually detect and destroy nascent cancer cells, and development of cancer requires evasion of immune responses via a number of mechanisms (Kim, 2007; Teng et al., 2008).

One approach for immune evasion is via downregulation of various proteins involved with processing and displaying antigens by the major histocompatibility complexes (MHC) of transformed cells (Garrido et al., 1997; Hicklin et al., 1999; Johnsen et al., 1999; Restifo et al., 1993; Rotem-Yehudar et al., 1996; Seliger et al., 1997). Cancer cells also undergo the process of immunoediting, in which immunogenic cancerous cells are routinely found and destroyed by CTLs or NK cells, such that the remaining cancerous cells are less immunogenic. Furthermore, tumors can use various cytokines to dampen immune responses, for instance TGF- β is found in higher levels in a wide range of tumors (Pasche, 2001).

There is currently immense interest in the ability of immune checkpoints to mediate immune evasion. These are ligands on the surface of cancer cells or immune cells, which regulate immune response and which can therefore be manipulated to influence cancer progression. The first immune checkpoint was identified in 1996, when researchers found that inhibition of cytotoxic T lymphocyte-associated protein-4 (CTLA-4), a receptor molecule on the surface of cytotoxic T-lymphocytes (CTLs), could lead to long-term remission of cancer (Leach et al., 1996). Following on from this, the first drug to inhibit CTLA-4, Ipilimumab, was approved in 2011 for the treatment of melanoma (Cameron et al., 2011). CTLA-4 negatively regulates CTL activation by binding B7-family receptors (CD80 and CD86) on antigen-presenting cells (APCs) (Figure 1.1, from (Alard et al., 2020)). CD28 is a positive regulator of CTL activity also expressed on CTL membranes. CD28 binds the same B7-family receptors as CTLA-4, but with lower affinity (Collins et al., 2002), so it can be outcompeted by CTLA-4. In the absence of cancer, CTLA-4 adjusts the delicate balance between recognition of foreign antigens and prevention of autoimmunity by preventing self reactivity (Chen and Mellman, 2013). CTLA-4 is also upregulated following CTL activation, and is constitutively expressed by T-regulator cells (Rowshanravan et al., 2018). As such, CTLA-4 inhibitor treatment is limited by severe immune-related toxicities as a result of the generic higher rate of CTL activation (Hodi et al., 2010). Other immune checkpoint targets with successful clinical inhibition include PD-L1 which is upregulated on the surface of certain cancer cells (Meyers et al., 2018), and it's cognate receptor PD-1 on the surface of CTLs.

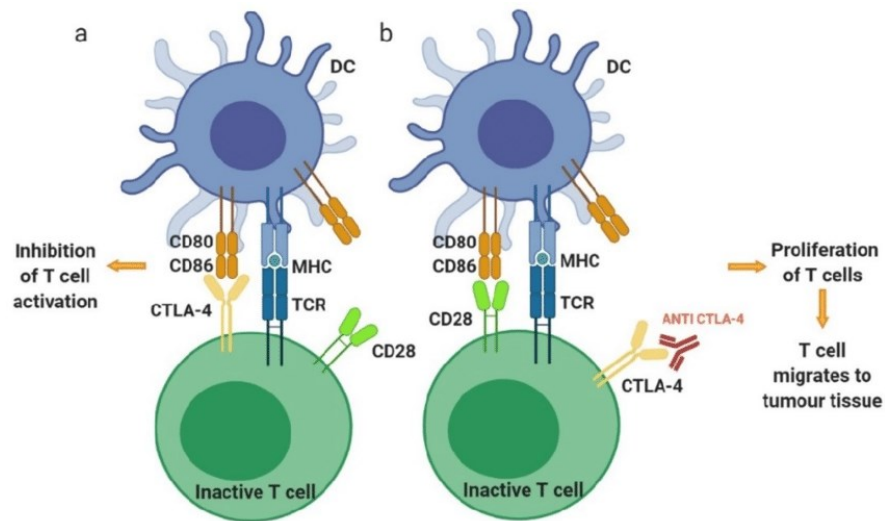


Figure 1.1 From Alard et al., 2020. CTLA-4 competes with CD28 for binding of the B7-family receptors CD80 and CD86. A) CTLA-4 activation causes CTL inactivation. B) Inhibition of CTLA-4 allows CTLs to be activated.

Enabling characteristics for cancer development

Development of cancer within a patient is driven by natural selection. Cancer cells progressively accumulate genetic alterations which provide replicative advantages. These alterations can in themselves lead to further alterations, if they occur in genes involved with DNA damage detection and repair, or increase the sensitivity of the affected cells to mutagens (Negrini et al., 2010). This increased likelihood of acquiring further genetic alternations is termed “genomic instability”. In addition, some cancer treatments can induce further mutations (McLendon et al., 2008). As cancer cells replicate, different genetic alterations occur in different daughter cells, and the population branches off into different subpopulations. These genetically and epigenetically diverse populations are subjected to selective pressure, for example by poor oxygen infiltration to cells in the center of a tumor, or drug treatment targeting clones with a particular mutation. Selection pressure can also simply be whether the tumor cells are able to replicate faster than other cells in the same niche, which would eventually allow them to dominate that niche. This selection leads to highly adapted and rapidly dividing populations of cancer cells.

Another positive feedback loop which often provides a driving force for cancer development is chronic inflammation. It is estimated that infection, autoimmunity or chronic inflammation of the affected site precedes 15-20% of all cancers (Grivennikov et al., 2010). The main effect of chronic inflammation is the alteration of the tumor microenvironment (TME), such that various signaling molecules which enhance tumorigenesis and metastasis are consistently present. Furthermore, chronic inflammation can induce genomic instability, through release of mutagenic reactive-oxygen species (ROS) (Grivennikov et al., 2010).

A common theme with these hallmarks is that the aberrant characteristics observed in cancerous cells are often not newly invented abilities. For example, glycolysis is a ubiquitous metabolic process, which is particularly relevant in muscle cells, but cancer cells use it in excess. Genetic dysregulation allows cancer cells to take advantage of a wider toolkit of genetically encoded abilities, which gives them a selective advantage over neighboring cells, or attempts by the immune system to inhibit cancerous growth. This makes cancer both very adaptable and difficult to specifically treat, without damaging healthy cells.

Drugs for cancer treatment

Chemotherapeutics

The beginning of modern chemotherapy for cancer treatment is often traced back to research during World War I, in which sulfur mustard gas was investigated as a chemical weapon (Gilad et al., 2021). Its toxic properties are as a result of DNA-alkylation, which prevents transcription of DNA into RNA, thus preventing protein synthesis. It was found that the extent of mustard gas' lethal properties was directly proportional to proliferation rate of treated cells, which led to the development of nitrogen mustard as a chemotherapeutic drug (Goodman et al., 1946). Although the first-generation nitrogen-mustards are no longer used in the clinic, less toxic derivatives and alkylating-like platinum-based chemotherapeutics (for example cisplatin and oxaliplatin) are still in use. Antimetabolites were also developed around the same time, with the first being used in 1948 (Farber and Diamond, 1948). These also target proliferating cells by mimicking a key metabolite (e.g. a nucleoside), such that they bind in the active site of metabolic enzymes and inhibit their activity (e.g. DNA replication) or are incorporated into nascent macromolecules, where they impede the function of those macromolecules. Examples of antimetabolite drugs developed at this time and still in use today include 5-fluorouracil (5-FU) (a pyrimidine analog) and Methotrexate (an antifolate). The general approach of targeting proliferating cells was further developed in the mid-1960s with the release of DNA intercalators, for instance Doxorubicin. Although the development of chemotherapeutic drugs was a big breakthrough, relapse still frequently occurred, and the side-effects of broadly targeting all replicating cells are highly damaging. As such, research continued in search of treatments which more selectively target cancer cells, such that they can be used at a higher concentration without damaging healthy cells.

Targeted drugs (aka genome-driven therapies)

The concept of targeted therapies which would act as a "magic bullet", selectively targeting cancer cells, whilst sparing healthy ones, was first suggested by Paul Ehrlich over 100 years ago (Strebhardt and Ullrich, 2008). Despite this early vision, the first truly targeted therapy, Imatinib, was only approved in 2001 (Druker et al., 2001). Imatinib targets the BCR-ABL oncogene (a result of reciprocal translocation

between chromosome 9 and 22), which characterizes chronic myeloid leukemia (CML) (Hungerford and Nowell, 1960). The mutant BCR-ABL protein is a tyrosine kinase which is constitutively active, but can be inactivated through Imatinib binding in the ATP binding pocket. Imatinib remains one of the most successful targeted therapies, with over 90% of CML patients today undergoing long-term remission, in contrast to roughly 20% before the introduction of Imatinib (Pui and Evans, 2013). Since 2001, the development of targeted therapies has rapidly increased, for instance there were 48 new kinase inhibitors approved by the FDA in 2019 (Roskoski, 2019). The surge in development of targeted therapies is largely due to the rise of “omics” technologies, which enable researchers to acquire large amounts of data about the molecular mechanisms driving different cancers. This in turn allows the identification of targetable cellular pathways which are commonly dysregulated in cancer.

Rather than directly targeting the aberrant signaling pathway, increasing knowledge about molecular mechanisms driving cancer can be used to create synthetic lethality. This is when a non-lethal cancer-specific aberration which is normally compensated for by an internal process, can be made lethal by inhibition of the compensatory process. Synthetic lethality is particularly useful therefore for treating cancers where reduced expression or activity of tumor suppressor genes are the main drivers, which can be very hard to directly target. By exploiting weaknesses which result from absence of normal protein activities, cancer cells can be specifically targeted. The classic example involves Breast cancer type 1 susceptibility protein (BRCA1), which is a tumor-suppressor gene which usually mediates repair of double-strand breaks in DNA. Poly [ADP-ribose] polymerase 1 (PARP1) is a protein involved with the repair of single-strand breaks in DNA. When patients with BRCA1 mutated cancer are treated with PARP1 inhibitors, the single-strand breaks accumulate into multiple double strand breaks, which cannot be repaired in the cancer cells, thus resulting in specific death of cancer cells. Synthetic lethality will likely be heavily exploited in future, as CRISPR-Cas9 technologies are developed further, allowing libraries of genes to be cheaply and specifically knocked out or inhibited (Castells-Roca et al., 2021). By correlating phenotypic response to CRISPR-Cas9 perturbation, with pre-existing genetic background of targeted cells, pairs of synthetic lethal genes can be identified and drugs can be chosen to exploit that dependency.

Despite the initial success of targeted therapies, only 8.33% of US cancer patients were eligible in 2018 for targeted therapies, and only 4.9% of patients benefited from them (Figure 1.2, from (Marquart et al., 2018)). The patients which do not respond to targeted therapies, despite indications that their cancer did have mutations or aberrations in the targeted proteins (40% of 8.33% who are eligible), suggests that many cancers make use of compensatory mechanisms through redundant signaling pathways to overcome targeted treatments. In order to overcome such compensation and achieve full, long-term remission for more patients, it will be essential to simultaneously target multiple oncogenic pathways used by cancer cells, using combination therapies.

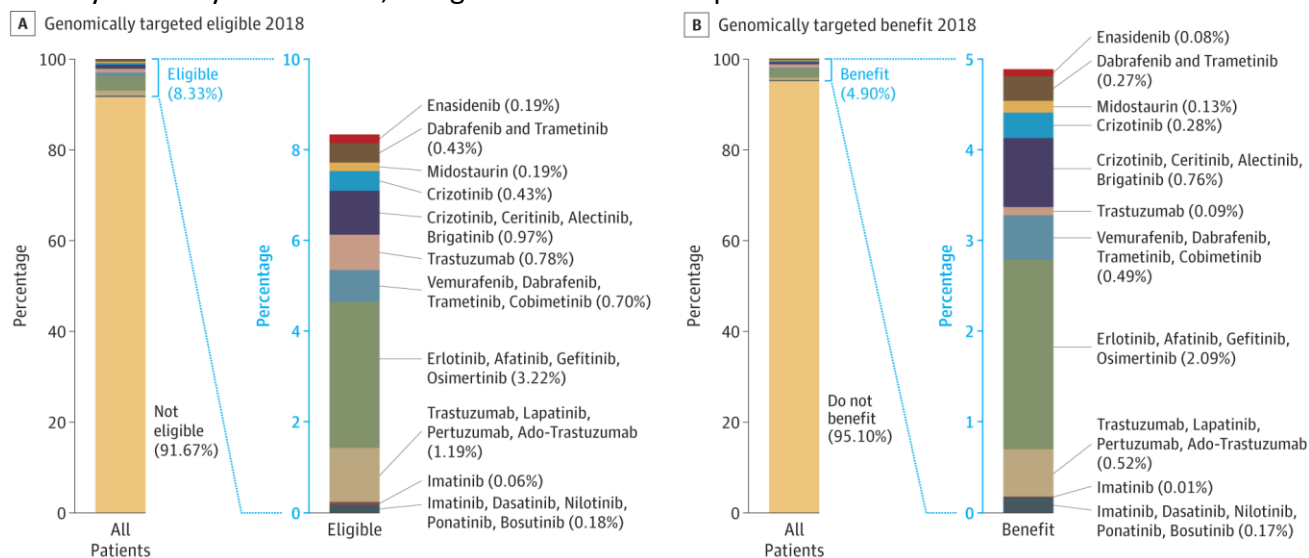


Figure 1.2 From Marquart et al., 2018. A) Percentage of US patients eligible in 2018 for genome targeted therapies. B) Percentage of US patients in 2018 who benefited from genome targeted therapies.

Immune checkpoint inhibitor drugs for cancer treatment

Immune checkpoint inhibitors (ICIs) target the interaction between immune checkpoints (e.g. CTLA-4) and their ligands. Other than inhibiting CTLA-4, the clinically approved ICIs can inhibit PD-1 on the surface of CTLs, and its ligand PD-L1 on the surface of tumor cells. A number of studies have shown that PD-1 and PD-L1 are upregulated in cancer, thus providing a more precisely cancer-specific target than CTLA-4 (Abiko et al., 2015; Akbay et al., 2013; Han et al., 2020). PD-L1 is expressed in 20-50% of human cancer (Herbst et al., 2013), which explains the broad and growing range of indications for which PD-1/PD-L1 inhibition has been approved. A number of other ICIs are currently being developed towards a range of targets including: TIM-3; LAG-3; TIGIT (Kon and Benhar, 2019).

As with all types of cancer therapy, response to ICIs is limited, with 44% of US patients eligible for treatment in 2018 yet only 13% benefiting from them (Figure 1.3, from (Haslam and Prasad, 2019)). This is more than 2x the response rate of genome targeted therapies, but comes with the significant disadvantage that ICIs are comparatively very expensive. One study for instance, found that a combination treatment with three non-ICI drugs cost on average 112,551 USD, whereas the same combination but with keytruda (PD-1 inhibitor) treatment added cost 113,731 USD extra but increased the quality-adjusted lifespan by 0.97 years (Criss et al., 2019). This high cost of treatment is another strong motivation to ensure accurate prescription of ICIs, so that only patients with a high chance of response are treated.

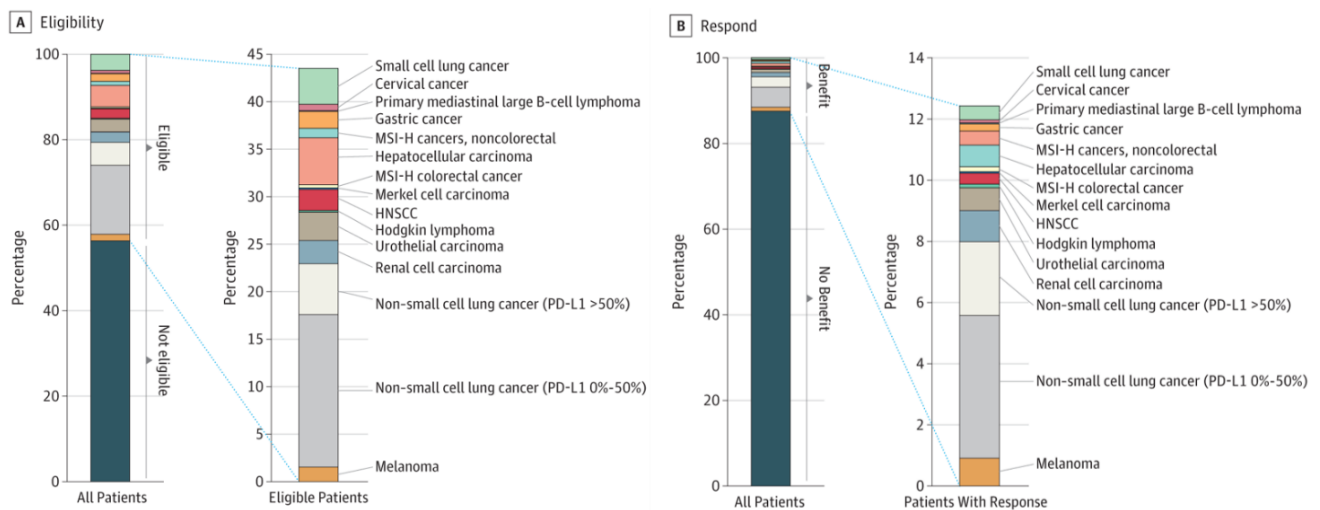


Figure 1.3 From Haslam and Prasad, 2019. A) Percentage of US patients eligible for immune checkpoint inhibition treatment. B) Percentage of US patients who benefited from immune checkpoint blockade treatment.

Drug combinations

The use of drug combinations for cancer treatment started to become popular in the 1950s after very successful trials using chemotherapeutics in combination for the treatment of childhood acute lymphoblastic leukemia (ALL) (Gilad et al., 2021; Greaves, 2016). The four-component drug combination which was developed in the 1950s and 1960s (FREI et al., 1965) still forms the foundation of current pediatric ALL treatment, which has a 90% survival rate. This is in sharp contrast to ALL's incurable status

in the mid 1900s. This shows that combinations are powerful because they can significantly increase efficacy of treatment by targeting multiple drivers within a clone. This also ensures that many more new mutations are required in the target cells in order for them to redevelop resistance. Furthermore combination treatments also prevent relapse because different clones within the cancer can be targeted. This is because targeting a single clone would simply create selection pressure which would drive the expansion of other clones. Combinations can also be used to reduce dosage while maintaining efficacy (thus reducing side effects). Finally, combining drugs creates new treatments very quickly, in contrast to the development of new monotherapies.

Drug combinations are said to be synergistic when the combined effects of the drugs is greater than the sum of each individual drug. Drug combinations can also be antagonistic, where the combined effect of the component drugs is less than the sum of the individuals. This can be useful when the effect in question is an unwanted off-target effect which is mitigated by the use of drug combinations, but antagonistic effects should be avoided when the effect in question is cancer cell death.

There are three main classes of synergy: complementary, anti-counteractive and facilitating (Jia et al., 2009; Sun et al., 2013). Complementary synergy is when different drugs affect the same biological function through targets in different pathways, or even targets in different parts of the same pathway, such that compensative signaling mechanisms cannot mediate resistance. Anti-counteractive synergy is when one drug has an effect within the cell, which elicits a cellular response to counteract the drug effect, and that cellular response is prevented by a second drug. For example, radiotherapy or chemotherapy can be used to induce DNA damage, and this can be combined with poly (ADP-ribose) polymerase (PARP) inhibitors to prevent DNA-damage repair. In one study the combination of cisplatin with PARP inhibition gave a 160% increase in lifespan compared to cisplatin monotherapy in a murine leukemia model (Lapidus et al., 2006). Facilitating synergy is when the effect of one drug is enabled by another. For instance in penicillin-resistant bacteria, vancomycin can facilitate the activity of gentamicin (Cottagnoud et al., 2003) because vancomycin increases cell-membrane permeability (Watanakunakorn, 1984), thus allowing greater penetration of gentamicin into bacterial cells.

Determining drug-sensitivity (personalized treatments)

Molecular profiling, the practice of categorizing patient cancers according to genomic, transcriptomic or proteomic data is a rapidly growing field, which already facilitates treatment personalization based on a few known biomarkers. Current approaches mostly focus on a single biomarker to determine treatment choices, for example treatment with Imatinib for patients with the BCR-ABL1 fusion gene. While molecular profiling is extremely effective for the limited number of biomarkers with directly related targeted treatments, such biomarkers are not available for every drug. For BRAF mutant melanoma for instance, it has been found that the efficacy of BRAF inhibitors depends on which additional molecular alterations are present (Chapman et al., 2011).

The potential advantages of combining knowledge about multiple molecular alterations using computational modeling approaches was shown in a very powerful study by Iorio et al. (Iorio et al., 2016). In this work, different cancer-specific molecular alterations (DNA methylation, copy number changes, somatic mutations and transcriptomic changes) were identified in 11,289 tumors. The same alterations were identified across a panel of 1,001 human cancer cell lines, and this was compared to drug sensitivity data for those cell lines, following a perturbation screen with 265 anti-cancer drugs. Logic modelling of signaling pathways was performed using an approach termed LOBICO (Knijnenburg et al., 2016), taking into account the different molecular alterations in each cell line. They found for instance, that sensitivity to Lapatinib (an ERBB2/ EGFR inhibitor) was dependent on the combined status of 3 different biomarkers: mutations in BRCA and TP53, but lack of a deletion at the FAT1/IRF2 locus. Another successful use of logic modelling used caspase-activity assay data which was produced by our lab in a microfluidics-based drug screen with 56 treatments (Eduati et al., 2018). Logic models were built based on the signaling nodes targeted by each drug (Eduati et al., 2020). The authors simulated the effects of a further 186 new treatments, and experimentally tested 3 of the conditions which showed the greatest cell-line specific effect. The *in vitro* experimental results corresponded well with the predictions.

With approaches like these, molecular profiling of patient cancer cells will allow patients to be assigned to increasingly precise treatment sub-groups, based on combinations of biomarkers which are known to correlate to sensitivity towards different treatments. This will significantly improve treatment

efficacy, but the scale of possible different genetic alterations and combinations thereof are too vast to be properly represented in current datasets based on cell line experiments. For instance Iorio et al. found that despite using 1,001 cell lines, they were unable to find cell lines which replicated every cancer-specific alteration present in their patient cell analysis, while for other alterations there was only one cell line (Iorio et al., 2016). Drug perturbation screens directly on patient cells, with both molecular profiling and phenotypic readout is therefore urgently needed to collect sufficient data for accurate modeling. Furthermore, in the study by Iorio et al. only 50% of the tumor samples had molecular alterations which could be correlated to drug response. Other studies have also found that for many cancer samples, drug sensitivities which could not be predicted by cancer genotype can be identified by high-throughput drug perturbation screens (Andersson et al., 2018; Crystal et al., 2014). These screens have the significant advantage that they allow biomarker-agnostic predictions of drug sensitivity, which means that they are not restricted by lack of knowledge about biomarkers and their interdependencies. If such screens became cost effective and widely available, patient tumors could be tested before and after treatment to monitor for clonal selection within a tumor, and identify the sensitivities of different clones. This would allow adaptive treatment decisions which would reduce the chance of relapse (Pemovska et al., 2013). In the best case, this would include an initial molecular profiling step to inform pre-selection of drugs which are likely to be effective, then perturbation of the patients cancer cells, followed by phenotypic assessment of drug efficacy.

Even if future modeling approaches are eventually able to accurately predict appropriate drug treatments based solely on biomarkers, identification of those biomarkers and training of models depends on access to large amounts of reliable, high-content data. As such, high-throughput experimental techniques are urgently needed. The scale of possible drug combinations in particular necessitates the use of computational models. Even if just the roughly 600 FDA-approved cancer drugs were screened as pairwise combinations, there would be over 175,000 possible treatments. This increases further if cancer drugs in clinical development or any of the many thousands of drugs approved by the FDA for non-cancer indications are tested. Furthermore, appropriate concentrations should be determined and combinations with more than 2 drugs are often required for maximum efficacy. Experimental screening at this scale on primary cells will likely never be feasible, but accurate, patient-specific drug screening data may provide the basis for computational predictions.

Transcriptomics as a readout to link genotype and phenotype

Of the different “omics” technologies, transcriptomics has immense potential as a future readout for drug screens, because it is a comparatively cheap form of high-coverage data, which allows complex pathway-activity modeling to be performed (Liu et al., 2019). Through counting the number of transcripts which align to each gene, the internal state of different cells or groups of cells can be quantitatively compared in terms of which genes are active. This provides detailed information about cell type, cell states and regulatory status. Unlike genomics, transcriptomics allows quantitative analysis, and unlike proteomics it allows detection of low-abundance molecules (via amplification of cDNA). Through the individual sequences themselves, genetic mutations in the analysed cells can even be identified. At the same time, phenotypic response to drug perturbations can be determined through machine learning approaches, or via direct detection of cellular toxicity signatures (Szalai et al., 2019). As a phenotypic readout, transcriptomics is less biased and more comprehensive than traditional phenotypic readouts, which rely on enzyme activity assays or reporter gene expression. This is why transcriptomics is sometimes said to link genotype to phenotype (Cieřlik and Chinnaiyan, 2018).

The Dialogue on Reverse Engineering Assessment and Methods (DREAM) project facilitates high-level data-science competitions with standardized metrics and blinded gold standards. As part of a collaboration with the National Cancer Institute (NCI), they ran a competition to produce the best drug-sensitivity prediction algorithm given a range of omics data types. Participants consistently reported that gene expression data provided the best predictive power (Costello et al., 2014), although this may have been influenced by the fact that bioinformatics tools for transcriptomic data were more developed. Participants also noted that combining multiple data types improved the predictions further. These findings were replicated by Iorio et al., who found that across a number of drug-specific models, those that performed best used gene expression data, and 86% of drug responses could be best predicted when other data types were also used for prediction (Iorio et al., 2016).

In order to facilitate wide-spread use of gene expression data for patient stratification, the cost per sample must be drastically reduced in comparison to traditional bulk RNA sequencing. Various approaches have been used to address this. One particularly successful approach is the Connectivity Map (CMap), which is a very large database of gene expression signatures following chemical and

genetic perturbation in a range of cell lines (Lamb et al., 2006; Subramanian et al., 2017). Such a database allows connections to be made based on similarities between signatures. For instance, mechanism of action (MOA) can be resolved for drugs where this was previously unknown, by comparing the signature of a drug with unknown MOA with that of known drugs. Another application of CMap is to identify potential therapeutics, by looking for a perturbation signature which is the opposite of a disease signature. Treatment of the diseased cells with that perturbagen should reverse the disease phenotype. This concept and CMap data were used to identify the ability of the plant flavonoid apigenin to reverse the disease phenotype of a particular subtype of cervical cancer (Yang et al., 2017). Signalling pathways can also be studied, if two perturbagens with known targets produce similar gene expression signatures, those targets are likely to be part of the same pathway.

There are currently well over 473,647 different perturbations signatures published, based on 25,200 perturbagens. To make this feasible, the researchers used the luminex L1000 platform (Peck et al., 2006) to survey the expression level of 1000 genes, chosen based on their independent regulation from each other (Subramanian et al., 2017). This reduced reagent cost to 2 USD per sample. The L1000 platform works by perturbing cells in microtitre plates, then performing cell lysis and reverse transcription. Ligation-mediated amplification (LMA) of 5'biotinylated DNA probes specific to each of the target genes was then performed. A gene-specific barcode sequence on the DNA probes was then used to capture the LMA products, by hybridization to barcode-complementary sequences attached to gene-specific polystyrene microspheres. Since each gene-specific microsphere exhibited a different color fluorescence and the biotin could be stained with streptavidin-phycoerythrin, these beads could be analyzed in a FACS-like manner to record the combination of gene identity and expression level for each bead.

Since the L1000 platform relies on imputation of data based on the 1000 genes which are probed, they strike a balance between cost and information gained, thus obtaining 82% of the information within the transcriptome (Subramanian et al., 2017). Although this approach is very effective, it does accept that some information will not be captured. In 2019 there was a study which used machine-learning to evaluate how many genes and which combination thereof allowed the maximum predictive capacity for drug response (Parca et al., 2019). The authors determined that a drug-unspecific set of 5000 genes

(out of 17419 measured genes) was required to capture the maximum predictive information about drug response. After this the addition of extra genes to the set did not provide an increase in predictive power. This set of genes was based on those with maximum variance between different treatments, rather than the involvement of the chosen genes in pathways which were known to be targeted or otherwise affected by drugs. One alternative to the L1000 platform which used Next-Generation Sequencing (NGS), rather than targeted expression profiling of a pre-selected set of genes is DRUG-seq (Ye et al., 2018). This used barcoded RT primers and 3' end next-generation sequencing to screen 433 compounds across 8 concentrations, at a cost of 2-4 USD per sample. It is worth noting however, that the sequencing depth used does not allow capture of some of the lowly abundant genes captured by the L1000 platform. Another approach called MIX-seq was developed in order to mix and profile up to 99 cell lines simultaneously, to enable cell-context-specific perturbation signatures to be better understood (McFarland et al., 2020). They use single-cell RNA sequencing and Single Nucleotide Polymorphism (SNP) profiling to resolve cell identities. While this approach is very powerful for direct comparison of context-dependent post-perturbation gene expression profiles, mixing cell lines could influence responses in a non-physiological way, through exchange of cytokines between cells which would not normally interact.

While all of these approaches provide impressive solutions to reduce cost and increase throughput, none of them attempt to automate the screening of drug combinations with gene expression readout. As previously mentioned, the number of even pairwise combinations possible from a panel of drugs increases quadratically with increase in the number of drugs. As such, the number of cells required and cost of drugs and other reagents can very quickly become prohibitive. Drastically reducing sample volume through the use of microfluidics is a very powerful approach to facilitate such drug screens.

Microfluidics

Overview

The term microfluidics encapsulates all techniques in which small volumes of fluid (10^{-18} to 10^{-6} litres) are spatially and temporally manipulated and analyzed. Performing experiments at this scale has many advantages. It can drastically reduce the volume of sample required for an experiment, increase experimental throughput through parallelization and even improve sensitivity of experiments by concentrating reagents. To do this, microfluidic chips with application-specific geometries are used, with features ranging from tens to hundreds of micrometers (Whitesides, 2006). The most basic features of microfluidic chips are chambers and channels, but chips can also include valves, electrodes and pumps. Most chips do not have integrated pumps however, so most microfluidic experiments are run using external pumps or pressurized sample reservoirs, which are connected to the chips via tubing. Flow rates of each fluid can be controlled by simply changing the settings on the pumps or pressure controllers.

For most experimental microfluidic applications, soft photolithography is used to produce microfluidic chips. Firstly, master molds are produced using photolithography, then inverse copies of the master mold can be cast using an elastomeric polymer. The most commonly used polymer in research laboratories is Poly-Di-Methyl-Siloxane (PDMS). The open side of the PDMS chip is sealed by bonding the chip to glass, through surface oxidization of both materials to create charged surfaces, then bringing both pieces into contact with each other (Duffy et al., 1998). A detailed description of soft lithography using PDMS can be found in the Materials and Methods section of this thesis. PDMS is particularly commonly used in biological research, because it is gas-permeable (Lamberti et al., 2014) and inert, therefore biocompatible, and it's transparency allows for imagining through the chip. This high level of biocompatibility of PDMS has allowed its use in long-term culture and imaging of both cells and whole organisms (Choudhury et al., 2012; Huberts et al., 2013). On the other hand, production of PDMS chips cannot easily be scaled up for commercial applications because mold production is time-intensive and each mold varies slightly from the next, such that parallel production of large numbers of chips is impossible.

Simple chambers

The simplest microfluidic devices are chambers of precisely designed shape and with very small dimensions. Such chambers are very powerful in biological experiments, as the different geometries can facilitate a number of different processes, from selection of specific cell types (Ozkumur et al., 2013), to physical positioning of cells (Hara and Merten, 2015). One way to increase the functionality of microfluidic chips, is to have multi-layer chips with channels on top of each other. This is the basis of the widely used “Quake valves” (Unger et al., 2000). These work by taking advantage of the flexibility of PDMS to make a thin, deformable membrane which is used to separate two layers of superimposed channels. Fluid in one channel can be controlled by pneumatic deformation of the membrane through the “control layer” into the “flow layer” (Figure 1.4B, from (Mathur et al., 2019)). If this deformation is large enough, fluid flow in the “flow layer” can be stopped.

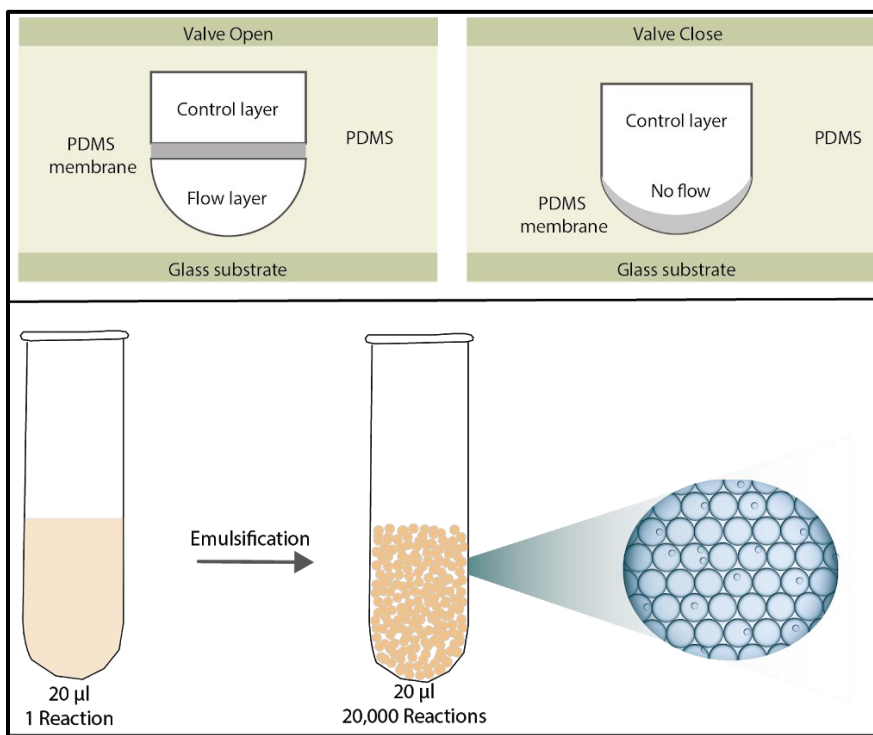


Figure 1.4 Edited from Mathur et al., 2019. Different formats for microfluidic experiments. A) Simple chambers through which fluid can be flowed to perturb cells, organoids or whole organisms. Such chambers often exhibit laminar flow, allowing precise spatial and temporal control of perturbation. B) Nanowell plates allow ultra-low volume plate-based experiments. C) Valving devices allow independent manipulation of different liquid streams. D) Emulsions of surfactant-stabilized droplets for parallelization and reduction of reagent volume.

Such valves can be used for a number of applications, most notably single-cell sequencing with the Fluidigm C1 system (Fan et al., 2011; Wang et al., 2012). Quake valves enable this by capturing single-cells and then even individual chromosomes within valved enclosures, together with relevant reagents, after which the contents of each enclosure can be separately extracted. Highly complex combinations of quake valves can be used together to create fluidic circuit boards (Gómez-Sjöberg et al., 2007; Vollertsen et al., 2020), with up to 1500 independently addressable chambers (Zhang et al., 2019). Alternative mechanisms exist to control microfluidic valves, for instance alignment of a microfluidic chip with a “Braille Display” device with individually actuatable pins, to mechanically open or close valves (Gu et al., 2004).

Another use of single-phase microfluidic devices is for “organs-on-chips”: microfluidic devices designed to simulate organs, by reconstituting the most essential aspects of that organ (Wu et al., 2020). One very powerful example is the “lung-on-a-chip”, which was used to study immune responses to lung infection in a mechanically actuated alveolar replica (Huh et al., 2010). The chip is composed of two superimposed cell culture channels separated by a thin, porous membrane with cells grown on either side. One channel is filled with fluid, while the other is filled with air, thus replicating the air-liquid interface that is present in the lung. Repeated stretching of the interface membrane allowed accurate replication of the mechanical forces experienced in active lungs. When bacteria were introduced into the alveolar channel and neutrophils into the fluid channel, the neutrophils were recruited through the membrane pores into the alveolar channel, where they phagocytosed the bacteria. Work is ongoing towards “humans-on-chips” systems, in which multiple organ chips are connected via a fluid network, thus replicating the interaction of different organs within in organism (Kimura et al., 2014; Tsamandouras et al., 2017). These systems could be used during the early stages of drug development, to allow researchers to test the pharmacology of their compounds on a system with much of the complexity of an animal model system directly with human cells. Furthermore, the ability to precisely control fluid flow rates and introduction of specific concentrations of compounds of interest, combined with the accessibility of the target cells for imaging or other measurements, makes these systems an incredibly powerful research tool.

Laminar flow

One important benefit of the small channel dimensions in microfluidic devices, is that rather than liquid flow being turbulent (as it is in macro-systems), liquids tend to exhibit laminar flow. This means that lateral mixing between layers of flow does not occur. The Reynolds number (Re) can be used to predict whether this effect is observed, by comparing the inertial and viscous forces acting within the channel. The inertial force is made up of three parameters: the fluid density (ρ), the velocity of the fluid (v) and the length scale of the system (D_h) which is on the scale of micrometers for microfluidic devices. The fluid viscosity is a single parameter (μ). The ratio between these factors can be written as follows

$$Re = \frac{\rho v D_h}{\mu}$$

With Reynolds numbers below 2000 (most microfluidic devices exhibit $Re < 5$), water-based fluid streams tend to behave like viscous fluids, forming stable laminar flow regimes within the channel. This means that mixing does not occur between two or more miscible fluids travelling parallel to each other within a channel, except for via diffusion. The rate of diffusion depends on the Péclet number (Pe), which depends on the channel length (l), the fluid velocity (v) and the diffusion coefficient of the molecule of interest (D). The relationship can be written as follows

$$Pe = \frac{lv}{D}$$

By adjusting the parameters of these two equations, in particular channel dimensions and flow rates, concentration gradients between two or more co-flowing solutions can be very precisely controlled. If cells, tissues or organisms of interest are held within the chamber, spatially and temporally targeted chemical perturbations can be achieved. This has allowed a number of successful studies, investigating topics as diverse as marine plankton environmental preferences (Ramanathan et al., 2015), to morphogen gradients in developing *Drosophila* embryos (Lucchetta et al., 2005) and chemotaxis (Frank and Tay, 2013). In an early example, Takayama et al were able to treat different sides of the same cell with various membrane-permeable molecules (Takayama et al., 2001). Using a microfluidic chamber with cells adhered to the channel, they showed the precision of this approach by first treating two sides of the same cell with different mitochondrial-targeting fluorescent dyes. The mitochondria were

stained with red or green fluorescent dye, based on the side of the cell they occupied when the dye treatment was given. In the next step, they showed that treating one side of a cell with a molecule (latrunculin A) which induces break-up of polymeric actin filaments led to dispersal of mitochondria from the treated side. This kind of precisely controlled, high resolution chemical perturbation is extremely powerful to learn about the complex interactions between organisms, cells and organelles with their local environment.

Droplets: surfactant-stabilized emulsions and 3-phase plug systems

To further increase the number of experiments which can be run in parallel, microfluidic chips can be used to produce miniature liquid droplets. Since droplets can be produced at kilohertz (kHz) frequencies, millions of droplets can be produced in a matter of minutes, each constituting an individual replicate or sample. For biological applications, the droplets are typically aqueous volumes separated by an oil carrier phase. In this setting, each droplet acts as an independent reaction vessel, allowing extremely high-throughput biological assays to be carried out. This can significantly reduce cost because the smaller volume per sample requires significantly less of each reagent. Furthermore, due to the low cell number required per replicate, fewer cells are required than for standard microtitre plate experiments. As such, when using a limited number of cells from patient samples, microfluidic experiments allow a larger number of conditions to be tested.

For the purposes of this work, it is important to distinguish between two types of droplets: surfactant-stabilized emulsions (droplets between 50 fL and 1 nL) and sequential arrays of larger plugs spaced out by oil (500 nL in this work), e.g. inside a microfluidic channel or length of tubing. Classical droplets are aqueous volumes whose form is stabilized by the addition of surfactant to the carrier oil phase. Surfactants are amphipathic molecules: they have both a hydrophilic and a hydrophobic group, making them partly soluble in both the oil and the aqueous phase. The presence of surfactants coating the aqueous droplets lowers the surface tension between the two immiscible phases. This increases the energy barrier between the system's local energy minima (in which the droplets exist) and its global energy minimum (where all droplets have coalesced such that the surface area of contact between oil

and water is at a minimum). This means that it is energetically unfavorable for surfactant-coated droplets to coalesce. In contrast, plugs are not surfactant-stabilized. This is possible because their form is largely maintained by the physical constraints of the location in which they are stored. In these settings, plugs are produced and stored sequentially in channels or tubing, where the plug diameter fills the entire cross-section of the channel. In many cases, plugs are further prevented from coalescing by interspersing each aqueous plug with plugs of a third immiscible phase (e.g. mineral oil or even a gas phase). In this way, different aqueous plugs are prevented from coming into contact with each other.

Picoinjection

Although it is not currently as easy to perform workflows in droplets with as many reagent addition or removal steps as in microtitre plate workflows, high-throughput reagent addition is possible. There are a number of different approaches to enable fusion of reinjected droplets with secondary reagents (Abate et al., 2010; Clausell-Tormos et al., 2010; Link et al., 2006). One widely-used approach is pico-injection (Abate et al., 2010), where droplets are re-injected through a narrow channel to put them into a single-file flow, then spaced out with additional spacer oil, and finally fused with an incoming stream of secondary reagents. A pair of electrodes at the junction of the reagent stream provide electrical pulses which trigger fusion of the reagents and droplets. The application of electrical charge can be precisely controlled, thus allowing secondary reagents to be added only to specific droplets of interest.

Another approach which was published around the same time, was for the fusion of non-surfactant stabilized reagent droplets with microfluidic plugs in the absence of electrical charge (Clausell-Tormos et al., 2010). In this approach, the droplets and plugs were alternately directed towards a “pillar chamber”, which consisted of a series of unrooted pillars perpendicular to the main flow chamber. The pillar chamber allowed the carrier phase to drain through the pillars, rather than exerting a forward force within the main channel, thus leaving the reagent droplets trapped in the chamber. A subsequently arriving plug was then spontaneously fused with the reagent droplets, due to the lack of surfactant. After this, the volume of the plug was so great that the carrier oil drainage was insufficient to hold the plug in place.

Encapsulation of particles into droplets

Biological experiments very often require the compartmentalization of cells into separate containers, such that they can be independently perturbed or studied. The significant advantages of performing experiments in microfluidic droplets, namely low compartment volume and high capacity for parallelization, mean that encapsulation of cells into droplets is highly desirable. This can be achieved simply by injecting a suspension of cells into a microfluidic device, together with the other aqueous reagents used for droplet production. This results in droplet occupancies which follow the Poisson distribution (Figure 1.5). Researchers can make use of this distribution, in order to perform single-cell experiments, by producing droplets with a very low probability of having 2 or more cells. This means that 90% or higher of droplets do not contain any cells, but the vast majority of the remaining droplets contain exactly 1 cell. To adjust the number of cells per droplet, the cell density of the cell suspension or the size of droplets can be changed. In order to determine the correct concentration of cells to produce single-cell droplets, the lambda parameter (λ) can be adjusted. λ values of 0.1 or smaller are typically used for single cell experiments.

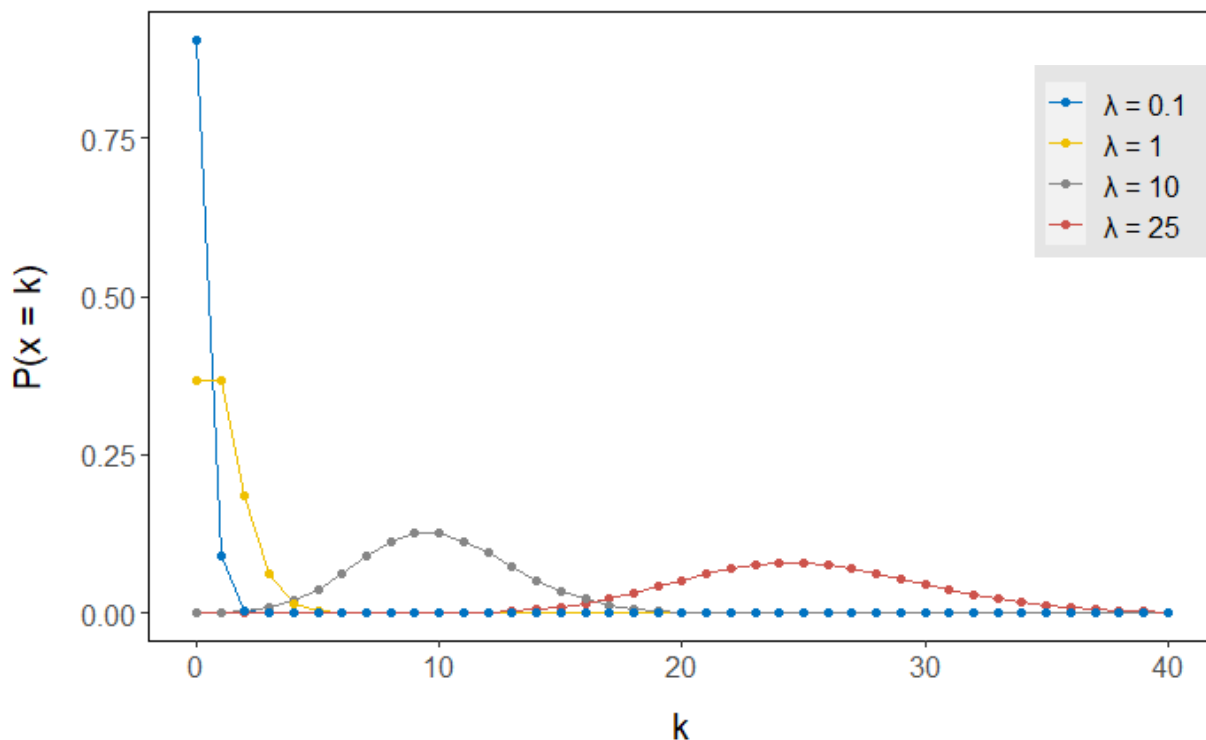


Figure 1.5 Own work. Probability of different numbers of cells (k) encapsulated into droplets based on λ values.

For some experiments, it is also necessary to encapsulate other species into droplets, for instance beads attached to unique DNA sequences which function as molecular barcodes (see below). For non-deformable particles, the probability of encapsulation also follows the Poisson distribution. For deformable barcoded hydrogel microspheres (BHM) however, a “Super-Poissonian” rate of encapsulation can be achieved. These beads can be closely packed within the infusion channel, which creates regular spacing if constant pressure is applied. This in turn creates a regular flow rate into the encapsulation channel, such that flow of BHMs into the encapsulation channel can be synchronized with droplet production. As such, the incorporation of BHM is Super-Poissonian, as this can be used to incorporate a single BHM into the vast majority of droplets (Abate et al., 2009).

Transcriptomics in microfluidics

Recently, the immense power of microfluidic droplets to facilitate parallelization has been demonstrated by the development and widespread application of in-drop and drop-seq: single-cell transcriptomic workflows in droplets (Klein et al., 2015; Macosko et al., 2015). A closely related approach has been very successfully commercialized with the development of 10x Genomics (Zheng et al., 2017). These methods all depend on the encapsulation of droplet-specific DNA barcodes into each droplet, together with a single-cell and lysis buffer. Within each droplet, the mRNA released from the lysed cell is captured by poly-dT sequences of the droplet-specific DNA barcodes. Reverse transcription is then carried out (before or after emulsion breakage, depending on the exact protocol). Single-cell sequencing is particularly desirable because it allows fine-grain information to be gained about different cell types within a tissue, even when there are no known biomarkers to distinguish the relevant cell types. By profiling cells based on their transcriptome, different groups of cells can be identified, their proportions within a tissue can be quantified and the transition states between cell types can be mapped. As proven by the very successful commercialization of the 10x workflow, these approaches are all very powerful. In-drop states that they were able to capture cells at a rate of 4,000–12,000/hour (Klein et al., 2015), which is a significant improvement on previous single-cell approaches which only reached a few thousand cells (Jaitin et al., 2014).

Cross-contamination between surfactant-stabilized droplets

The biggest limitation to the use of surfactant-stabilized droplets for high-throughput drug-screening experiments is in maintaining differing chemical content between droplets. Although essential for droplet stability, surfactants mediate significant exchange of hydrophobic molecules between droplets (those with a logP of ~ 2 or greater). This limits the types of molecules which can be retained within droplets over time.

To quantify the speed and scale of exchange between surfactant-stabilised droplets, Gruner et al created "minimal emulsions" to study surfactant-mediated exchange of droplet contents (Gruner et al., 2016). The minimal emulsions consisted of monodisperse droplets arrayed in a one-dimensional train within a microfluidic chip, such that the distance between each droplet centre and the next was controlled. This one-dimensional array allows for modelling of the exchange between droplets, as the interface between droplets is reduced to a single membrane (the fluorinated oil between each droplet). The droplets were produced with and without resorufin (a hydrophobic fluorophore) in an alternating manner, then stored such that each droplet which contained resorufin was neighbored by an "empty" droplet. The authors found that the resorufin exchanged between droplets until after a number of hours, the system had relaxed to a state of equilibrium with the same concentration of resorufin in every droplet. The time required to reach equilibrium decreased with increased surfactant concentration or decreased distance between droplets. They were able to conclude that vesicles or reverse-micelles were the vector for exchange between droplets, by measuring the rates of diffusion during fluorophore exchange and modelling the permeability of the membrane between the droplets. From this they concluded that the diffusing species were much larger than single fluorophore molecules. Calculations based on this observation, and on dynamic light scattering put the size of the diffusing species at ~ 200 nm. All other conditions being equal (distance between droplets, surfactant concentration etc.), different fluorophores were found to exchange at different rates, depending on their hydrophobicity. Fluorescein dye took several days to exchange, while Rhodamine 6G took only minutes. One way of avoiding the cross-contamination between droplets as a result of surfactant exchange, is to use microfluidic plugs as reaction vessels, rather than classical surfactant-stabilized droplets. Without the presence of surfactants, micellar transport does not occur.

Drug-screening in droplets

The aforementioned benefits of droplet microfluidics, namely the small sample volume and the capacity for high-throughput via automation, is highly beneficial for the screening of drug treatments on patient cancer cells. Microfluidic droplets and plugs can be produced with a wide range of cell densities, depending on the application. This is essential, because the number of patient cells available from a single patient sample is limited: 500,000 cells for a fine-needle aspiration biopsy (Rajer and Kmet, 2005) and up to hundreds of millions cells for resected tumor pieces. Using 96-, 384-, or 1536-well plates, drug screens usually require 500-60,000 cells/ well (Dietrich et al., 2018; Popova et al., 2020; Shum et al., 2008), although the lower end is only reached with the use of expensive pipetting robots. This means that cell number is frequently the limiting factor for throughput of a drug-screen. It is important to note that *in vitro* amplification of patient cells prior to drug screening leads to the selection of particular clones which survive well *in vitro* and therefore do not reflect the true drug sensitivity of the cancer (Montero et al., 2015). Because of this, it is highly desirable to perform drug perturbation screens directly on patient cells without *ex vivo* culturing steps. Performing screens in microfluidic droplets also provides a unique opportunity to maximize throughput at comparatively low cost.

There have been numerous approaches published to use microfluidics for testing of monotherapies against cancer cells. One early approach cultured 30 nL hydrogel droplets with encapsulated brain cancer cell lines or primary patient cells in a micropillar chip (Lee et al., 2014). Drug treatment was achieved by sandwiching the micropillar chip with a microwell chip which contained 24 different drug compounds. From this, the authors were able to obtain dose response curves for each drug, in total testing 144 conditions. Another method used ethidium homodimer 1 staining of single-cells in droplets to screen 5 conditions, using just 80,000 cells in an array of wells, which captured and stored droplets (Wong et al., 2017). Another approach used a droplet microarray platform composed of a glass slide with regularly spaced regions of hydrophilicity bordered by hydrophobic regions (Popova et al., 2020). Drugs were printed with a liquid dispenser onto the hydrophilic regions and the slide was sandwiched with another slide covered with cell droplets, containing 100 primary chronic lymphocytic leukemia (CLL) cells each. This allowed testing of 9 drugs, at 10 concentrations, with 4 replicates each using an imaging-based readout with PI and calcein-AM staining to detect cell death and viability respectively.

While these approaches were very effective, they do not test large numbers of different drugs (30<), and they do not allow for systematic screening of combinations within the drug panel. In 2018 Kulesa et al. published a method for the screening of antibiotic drug combinations against the model pathogen *Escherichia coli* (Kulesa et al., 2018). In this work, drugs were encapsulated into droplets, together with a unique barcoding dye and target bacterial cells constitutively expressing GFP. For each drug, 20,000 1 nL barcoded droplets were produced using a Bio-Rad QX200 instrument (for droplet digital PCR). Barcodes were drug-specific concentrations of one of three fluorescent dyes. For each chip, a total of 64 different drugs were screened by mixing all of the droplet pools from the chosen drugs, and applying this to a microwell array, where two droplets were randomly encapsulated together into each well. When a high voltage pulse was applied across the array, each pair of droplets fused, creating drug combinations. The arrays were imaged to determine the drug identity of each droplet and the growth rate of the encapsulated bacteria, based on the increase in GFP. This workflow allowed three-point dose-response curves to be determined for 10 antibiotics, paired with single doses of 4,160 non-antibiotic compounds, all within 10 days. While this is very impressive, this workflow did require more than 100 chips to achieve this throughput, and it is not clear whether this setup could be applied to mammalian cells, especially as the voltage pulse for droplet fusion has the potential to damage mammalian cells. More critically, the cells are pre-transfected with GFP, which would not be feasible for drug screens on patient cancer cells, as the process of transfection would significantly reduce the cell number and may influence drug response.

Recently, our group published a drug-combination screening approach which uses microfluidic plugs (Figure 1.6) (Eduati et al., 2018). In this work, an automated Braille Display (BD) valving module was used to produce 0.5 μ L plugs containing different pairwise drug combinations, stored sequentially in a length of tubing. Each plug had around 100 patient cells per droplet and reagents for a fluorescent readout. The fluorescent readout was based on the presence of caspase-3/7: an early marker for apoptosis. Per screen, 56 different drug combinations were produced, with 20 replicates per combination (2 cycles of 10 replicates). Each plug was separated by a mineral oil droplet, and each drug combination was separated by a set of blue fluorescent plugs to delimit the change in condition. The plugs were incubated overnight and the extent of apoptosis induced by the different drug combinations was determined, by measurement of the green fluorescence in each plug. This system is cheap and fast,

requiring low amounts of sample and drugs (costing less than US\$ 150 per run) and taking less than 48 hours from the point of tumor resection or biopsy to end of data analysis.

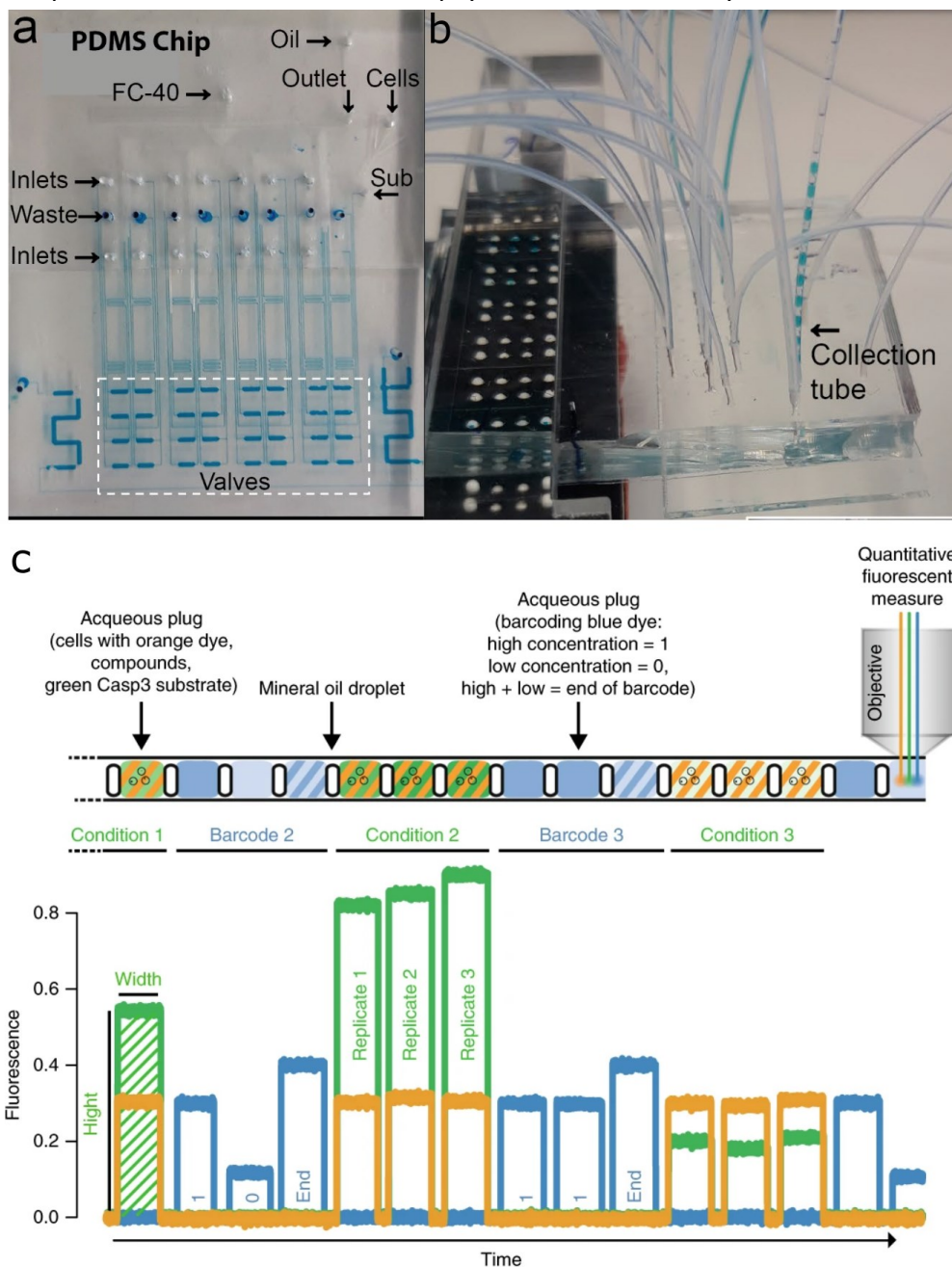


Figure 1.6 Figures combined from initial paper, plus figures from a recently submitted protocols paper on the same workflow (Eduati et al., 2018; Utharala et al., 2021). A) Microfluidic chip for producing 0.5 μ L plugs with a Braille Display (BD) valving unit. B) Drugs, cells, green-fluorescent caspase assay reagents, barcode dye and media were injected into the BD valving chip. Plugs were produced when aqueous flow was directed by the valves to plug production (rather than waste). Each sample plug, separated from the next by an immiscible mineral oil droplet, contained cells, assay reagents and a drug pair. Conditions were separated by blue barcoding plugs. C) After 16 hours of incubation, fluorescence of each plug was measured by excitation with 3 lasers and detection of emission by photomultiplier tubes (PMTs).

Another in-house approach further developed this idea by combining the same BD valving module with an autosampler (Figure 1.7, from (Mathur et al., 2021)), to produce up to 420 pairwise drug combinations in surfactant-stabilized droplets with a transcriptomic readout (Mathur et al., 2021). The key development for this work was the paired DNA barcode fragments which could be annealed together to encode the drug-pair used for treatment. Each monotherapy drug which fed into droplet production was mixed with a corresponding poly-dT barcode fragment or a biotinylated barcode fragment. This resulted in droplets which contained one of each type of DNA barcode fragment, together with a corresponding pair of drugs and a single cell. Once these components were mixed together, the barcode fragments annealed via a complementary ligation site, producing a full-length DNA barcode. After 12 hours of incubation off-chip, reagents were added via picoinjection, which facilitated ligation of barcode fragments, lysis of drug-treated cells and reverse transcription of released mRNA. The resultant single-stranded cDNA was extracted, amplified and sequenced. This approach identified a number of synergistic and antagonistic combinations for the K-562 cell line (Triciribine-Dacarbazine and Razoxane-Trametinib, respectively).

The major limitation of this approach is that it was extremely complex, and therefore would not be suitable for everyday use, particularly not in clinical settings which require fast results and simple workflows. In addition, use of surfactant-stabilized droplets limited the range of drugs which could be tested. In order to prevent exchange of drug treatments between droplets, which would nullify the compartmentalization of drugs into different droplets, only drugs with a low hydrophobicity were used (mostly logP of 0 or below). As most drug compounds need to pass through hydrophobic membranes in order to be active, most drug compounds have a logP between 2 and 3. Furthermore, since drug response of cells is significantly affected by interaction of target cells with other nearby cells, it is highly desirable to perform drug screens on groups of cells. Maintaining some cell-cell interactions ensures that the physiological environment which would be experienced by the cells *in vivo* is at least partly replicated.

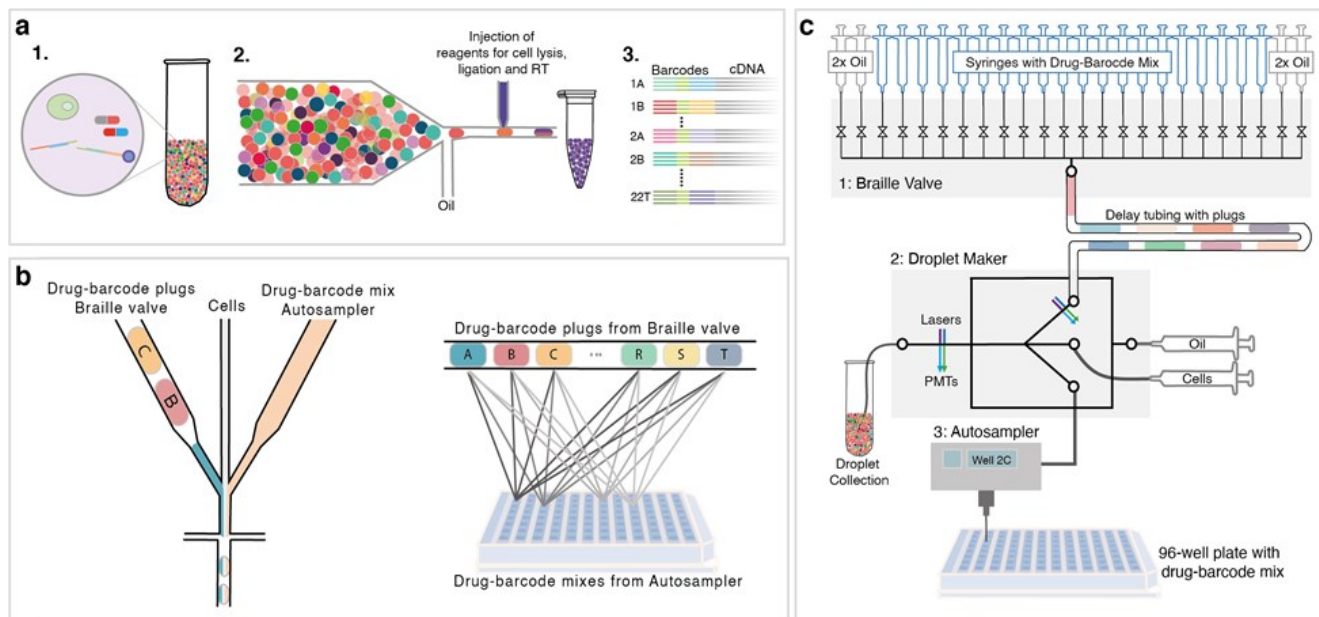


Figure 1.7 From Mathur et al., 2021. Workflow for droplet-based combination treatment with transcriptomic readout. A) Overview of complete workflow. Drugs were mixed with DNA barcode fragments then combined into surfactant-stabilized droplets containing single cells. After overnight incubation, reagents were added for ligation of barcode fragments, lysis of drug-treated cells and reverse transcription of released mRNA. The resultant single-stranded cDNA was extracted, amplified and sequenced. B) Schematic showing how different components come together to produce combinations in droplets. C) Hardware components for droplet production: a droplet-maker chip to integrate injection of cell suspension, injection of a train of plugs from a BD valving platform and injection of drugs from a microtitre plate.

Aims of this work

This work is a combination of two related projects, both aimed at improving outcomes for cancer patients by working towards microfluidic workflows for determining patient specific drug combinations.

The first project aimed to evaluate the feasibility of performing fluorescence-based screens in plugs, to determine sensitivity of cytotoxic T-lymphocytes (CTLs) to different combinations of immune checkpoint inhibitors (ICIs). To perform such a screen, a fluorescent assay is required which reports on CTL activity with a strong signal-to-noise ratio up to 24 hours after mixing of component cells with drugs. Fluorescence must be dispersed in the media surrounding the cells, rather than localized to individual cells for it to be accurately measured in plugs. The primary aim of the first project was therefore to evaluate two candidate assay formats to determine whether they could be used for a microfluidic plug-based screen to test different combinations of ICIs. To do this, I first needed to obtain a reliable source of T-cell capable of cytotoxic activity and find a means of overcoming T-cell receptor (TCR)-mediated specificity of CTL activity. Results from this work are presented in Chapter 2, part 1 **Evaluating the feasibility of fluorescence-based cytotoxic T-lymphocyte activity screens to evaluate cell-specific immune checkpoint inhibitor efficacy.**

The second project built on a workflow developed by Dr. Lukas Mathur to perform drug combination screens on single cells in surfactant-stabilized droplets, using a transcriptomic readout. While this workflow was very impressive, it was too time-consuming and complicated to be implemented in the clinic. Furthermore, for accurate screening of solid tumor biopsies it would be beneficial to perturb pools of cells rather than single cells, so that cell-cell interactions are maintained. In addition, using surfactant-stabilized droplets severely limits the drugs which can be used without cross-contamination occurring. As such, I aimed to transfer this workflow into microfluidic plugs so that it was easier to implement, target cells could be screened as a group and surfactant-mediated exchange of drugs could be avoided. To do this, I aimed to integrate aspects of different microfluidic workflows together, adapting and optimizing each as needed. I also aimed to evaluate the workflow at multiple stages of development to understand and reduce potential sources of error. Results from this work are presented in Chapter 2, part 2 **Developing a microfluidic workflow for combinatorial drug screens on cancer cells with transcriptomic readout.**

2. Results

Evaluating feasibility of fluorescence-based cytotoxic T-lymphocyte activity screens to determine cell-specific immune checkpoint inhibitor efficacy

Immune checkpoint inhibitors (ICIs) are extremely powerful when patients respond to treatment, but the rate of patient response is low (Haslam and Prasad, 2019). For instance only 20-25% of non-small cell lung cancer patients have a sustained response to immune checkpoint inhibitors (Kaderbhai et al., 2019). Predicting patient response is extremely complex, as it depends on many different factors:

- Infiltration rate of different types of immune cells into the tumor. For example, high levels of T-regulatory cell infiltration is correlated with poor prognosis (Principe et al., 2021).
- Number of immunogenic antigens (neoantigens) expressed by cancerous cells (Syn et al., 2017). This is correlated to mutational burden.
- Expression level of immune checkpoint inhibitor by the cancer cells.
- Signaling factors in the tumor microenvironment (TME).

Another complexity related to the prescription of ICIs is that combination treatments are increasingly used in an attempt to reduce side effects whilst obtaining a strong response. Furthermore, following the initial wave of success with ICIs targeting PD-L1 and CTLA-4, a number of other ICIs were developed towards novel checkpoints (TIM-3; LAG-3; TIGIT) (Kon and Benhar, 2019).

In order to aid doctors in choosing the correct ICI prescription for each patient, we set out to develop a microfluidics-based screening platform capable of predicting patient-specific ICI sensitivity. We noted that the Braille Display (BD) valving platform could be used to combine different ICIs, patient cancer cells, primary cytotoxic T lymphocytes (CTL) and different signaling factors in microfluidic droplets. After incubating these components together, the ICIs or ICI combinations that led to CTL-induced cancer cell death, should be determined based on a fluorescent signal.

Inspiration for how to perform this screen came from a plate based RNAi screen for identifying novel immune checkpoints (Khandelwal et al., 2015). In this work, a bispecific antibody targeting both EpCAM and CD3 was used to overcome T-cell receptor (TCR)-specificity, by bringing target breast cancer MCF7 cells and primary CTLs into close proximity, and activating the CD3 receptor in the process. This

arrangement mimicked high levels of CTL-infiltration into the tumor and recognition of target-cell expressed neoantigens by the TCR, since CD3 mediates TCR signalling. The epithelial cell adhesion molecule (EpCAM) is a common target of bispecific antibodies because it is present on a broad range of epithelial cells and is often upregulated or more accessible in cancer cells. In this study, a library of siRNAs targeting cell-surface and transmembrane proteins was transfected into MCF7 cells in different wells of a 384-well plate, to inhibit production of candidate immune checkpoints. All target cells were transfected with luciferase, to allow detection of target cell death by altered luciferase activity. With CTLs stimulated and in close proximity to the target cells, the extent of cytotoxic activity from the CTLs was dependent on expression of immune checkpoints by the MCF7 cells. To rule out siRNAs influencing the viability of transfected cells directly, viability of transfected cells without CTLs was always compared to that of non-transfected cells. In order to use the same CTL-targeting approach, we obtained an EpCAMxCD3 bispecific antibody from Amgen, which was in development as a potential therapeutic.

Selecting and activating primary cytotoxic T lymphocytes

To test the efficacy of immune checkpoint inhibitors (ICIs), activity of treated CTLs must be tested. As a potential source of CTLs, the TALL-104 cell line (O'Connor et al., 1991) was trialed, but had very poor viability in cell culture. This correlated with other reports that these cells were very difficult to culture (Yamawaki et al., 2021). In addition, most researchers studying CTL cytotoxicity use primary CTLs (Cerignoli et al., 2018; Khandelwal et al., 2015) because existing CTL lines do not recapitulate the full cytotoxic capabilities of a physiological CTL pool. As a result, we chose to isolate and activate primary human CTLs. Since cytotoxic activity of primary CTLs varies significantly from donor to donor, we always used a mixed pool of CTLs from several donors. This had two advantages. Firstly, we produced a stock with a more averaged cytotoxic activity level. Secondly, this gave a large stock of CTLs, so that the same stock could be used for a large number of experiments, thus reducing the variation between experiments.

CTLs were isolated from whole blood in two steps. Firstly, the whole blood was layered onto a density gradient solution of histopaque, then centrifuged to separate mononuclear cells (T cells, B cells, NK cells

and monocytes) from the less dense erythrocytes. This was followed by negative selection of CTLs using a magnetic activated cell sorting (MACS®) kit, from Miltenyi. This used a cocktail of biotinylated antibodies which targeted cell-surface proteins on all types of mononuclear cell, other than CD8+ T-cells. Streptavidin-conjugated magnetic microbeads were then added to the mixture, thus enabling magnetic capture and removal of all non-CD8+ cells. The vast majority of isolated cells were CD8 positive (Figure 2.1).

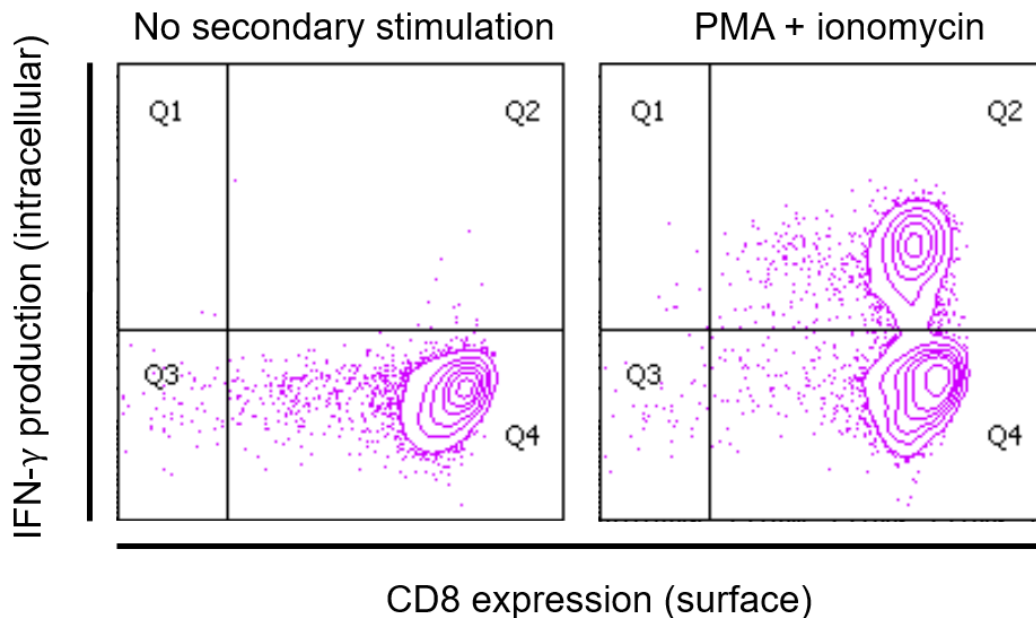


Figure 2.1 CD8+ cytotoxic T-lymphocytes (CTLs) were isolated from whole blood by centrifugation followed by negative selection. Cells were then activated with anti-CD3 and anti-CD28 antibodies for 2 days, then with IL-2 for 3 days. Activation was detected by comparing IFN-γ production in activated cells with and without secondary stimulation with PMA and ionomycin. Cells which had successfully undergone activation showed upregulation of IFN-γ production after secondary stimulation.

After CTLs were isolated, they were stimulated by CD3 and CD28 for 2 days, followed by treatment with interleukin 2 (IL-2) for 3 days. This treatment replicated the steps which would occur in-vivo following the interaction of the T-cell receptor (TCR) with its target peptide presented by an MHC class I molecule on the surface of a cancerous cell, virus-infected cell or antigen-presenting cell (APC). The first step of the process caused activation of the CTLs, by inducing signaling via CD3 and CD28. As seen in Figure 2.2 (Srivastava and Riddell, 2015), TCRs are associated with CD3 signaling modules, which transmit the signal from a triggered TCR into the cell. This is referred to as “signal 1” of the process of CTL activation.

During antigen-presentation, B7 proteins on the surface of APCs also bind CD28 on the surface of the interacting CTL. This co-stimulation is “signal 2” of CTL activation. Finally, activated CTLs and also nearby CD4+ T lymphocytes release interleukin-2 (IL-2) cytokines, which are the source of the final signal for CTL activation “signal 3”. This third signal maintains the clonal expansion of newly activated CTLs, once the initial activation signal is no longer present.

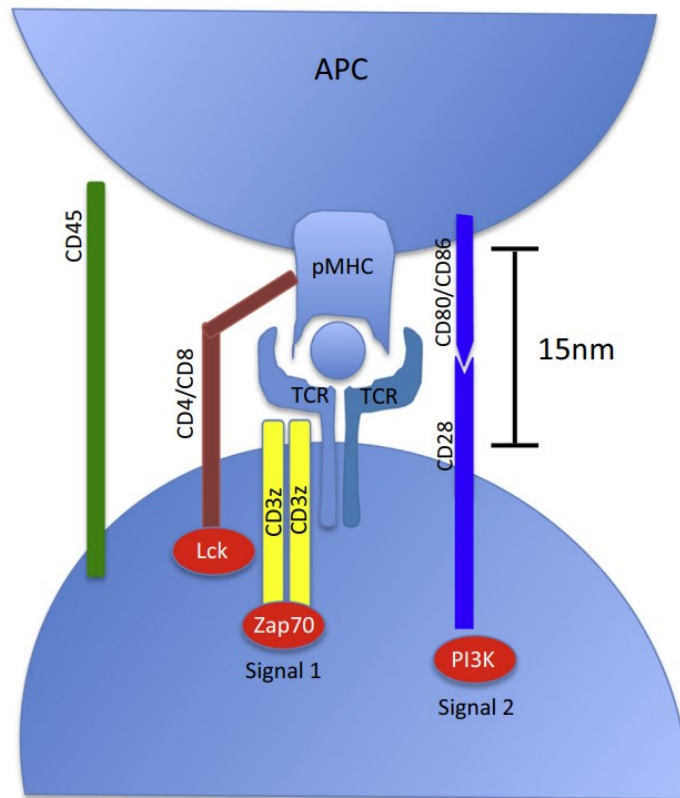


Figure 2.2 Edited from Srivastava and Riddell, 2015. Activation of cytotoxic T lymphocytes (CTLs). The first signal comes from binding of the T-cell receptor (TCR) with its target antigen in an MHC class I receptor. It is transmitted by CD3 molecules associated with the TCRs. The second activation signal comes from binding of CD28 on the CTLs to CD80 or CD86 on the target or antigen presenting cells.

To assess whether this activation process worked, activated cells were further stimulated with phorbol 12-myristate 13-acetate (PMA) and the calcium ionophore: ionomycin. PMA and ionomycin rapidly enter CTLs and activate protein kinase C (PKC), a downstream signaling molecule from TCR stimulation (Chatila et al., 1989). This also replicates downstream signaling from activation via the TCR, but happens on a faster timescale than with CD3 and CD28. As such, the combination is commonly used as a secondary stimulation, to replicate the stimulation which occurs *in vivo* when CTLs which have already

been activated come into contact with a target cell. Flow cytometry analysis was performed following secondary activation to measure interferon-gamma (IFN- γ) production by the CTLs. IFN- γ is a classical marker of CD8+ T-cell activation, because it is strongly correlated with production of cytotoxic effector molecules, such as perforin and granzymes (Nicolet et al., 2020). IFN- γ also induces expression of MHC class I molecules on surrounding cells, thereby increasing the chance that cancerous or virus-infected cells will be recognized by CTLs (Schoenborn and Wilson, 2007). As seen in Figure 2.1, the IFN- γ positive population of CD8+ T-cells was 40.1% of analyzed cells when secondary stimulation was given, vs. 0.3% for cells without secondary stimulation. This is similar to the 47% percent of CD8 positive, IFN- γ positive cells found after activation in a comparable study (Nicolet et al., 2020). Consistently with each new blood sample and aliquot of buffy coat, CD8+ T-cells could be isolated and activated. These results showed that the activation process was successfully established and the CTLs could be used for activity screens with target cells.

[Assays to detect activity of cytotoxic T lymphocytes on target cells](#)

With a reliable source of activated primary CTLs, the next step was to develop a method for detecting CTL activity. The MCF7 breast cancer cell line was chosen for the target cells because it expresses EpCAM, making it amenable to binding with the EpCAMxCD3 bispecific antibody. In the screen by Khandelwal et al., target MCF7 cells were transfected with luciferase to allow detection of cell death by reduced luciferase activity (Khandelwal et al., 2015). While this was a very effective approach for finding novel immune checkpoints, this approach would not be appropriate for screening of patient cancer cells for their ICI sensitivity. This is because transfection approaches take time and do not work with 100% efficiency, thus reducing the number of available target cells and making the workflow more complex. Furthermore, luminescence is not suited for high throughput assays in a droplet format, since the signal detection takes up to several seconds (versus microseconds for fluorescence readouts). In addition, the workflow used by Khandelwal et al. used a multi-step process for measuring luciferase activity, first removing supernatant, then lysing cells, then measuring the luciferase activity. Multistep processes of this complexity cannot be replicated with a microfluidic workflow. As such, an alternative readout method was required. This needed to satisfy the following constraints:

- The readout should be fluorescence-based, but with fluorescence dispersed in the media surrounding the cells, rather than localized to each target cell. This is because the collection tubing through which the microfluidic plugs are measured is 0.6 mm in diameter, and the cells can move freely within the cross-section of this space. The laser used for excitation of fluorophores is only focused on one z-plane, so only a fraction of cells are in focus during readout. If the fluorophore is localized in the surrounding media, then it doesn't matter which z-plane the laser is focused to, as each z-plane will give the same fluorescence level.
- The readout should be able to occur based on reagents which were added to the plugs at initial production. This is because steps of reagent addition or removal are difficult and added complexity should always be avoided if possible.
- The readout must give information specifically about cell death of target cells and not CTLs.
- The readout must be robust over an incubation period of 24 hours, as plug production takes a minimum of 5 hours and incubation times of published CTL cytotoxicity assays are between 3 and 18 hours (Ganesan et al., 2019; Khandelwal et al., 2015; Wonderlich et al., 2006).

Calcein-AM green release

The first approach trialed for detecting CTL-induced target cell death, was to stain the target MCF7 cells with calcein-AM green, and detect released fluorescence as a proxy for target cell death. Calcein-AM green enters cells and is cleaved by internal esterases, making it both fluorescent and negatively charged such that it should no longer readily leave the cell. It is also non-toxic. To test this approach, MCF7 cells were stained and mixed with CTLs (20 CTLs per 1 MCF7 cell), bispecific antibody, or both, in 384-well plates. After 4 hours of incubation, the plates were imaged and the supernatant fluorescence was removed and measured (Figure 2.3A). Within this timeframe, the positive control samples which had all three components (stained target cells, activated CTLs and bispecific antibody) had 1.4 times higher release of fluorescence, than negative control samples, where one or both of CTLs and bispecific antibody were absent (p value of 0.0039 or 0.0035 respectively). This showed that the combination of bispecific antibody and CTLs allowed specific killing of target MCF7 cells. This was reinforced by the

microscopy images taken of the cells (Figure 2.3B), which showed large cell clumps only when all three components were present.

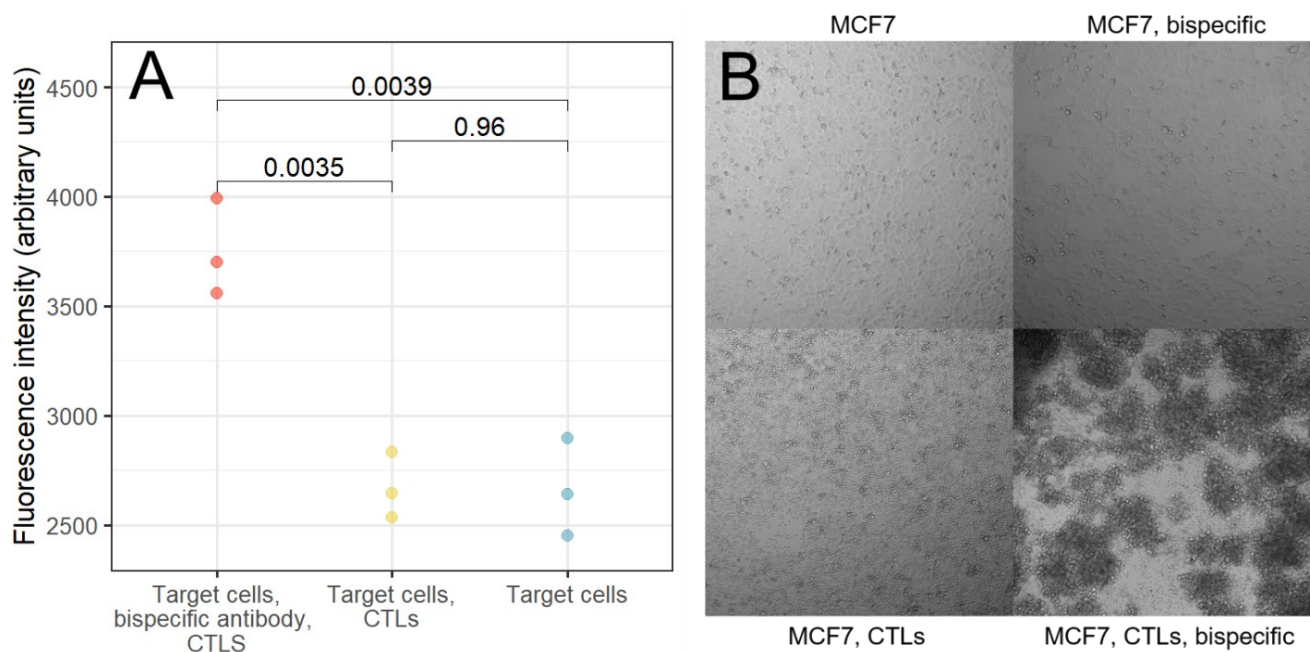


Figure 2.3 Induction of target MCF7 cell death by cytotoxic T-lymphocytes (CTLs) is enabled by bispecific antibodies targeting EpCAM on MCF7 cells and CD3 on CTLs. MCF7 cells were stained with Calcein-AM green and incubated with pre-activated CTLs (at a 20:1 ratio) and bispecific antibodies. A) Supernatant from the cell mixtures was removed and green-fluorescence measured. The combination of all three components led to a 1.4 times higher release of calcein-AM green fluorescence (indicating MCF7 cell death), than when any component was missing. p-values were computed using two-tailed t-tests. B) The cell mixtures were imaged with a 10x objective. Cell clumps were observed only when all three components were present, indicating that the bispecific antibody brought CTLs and MCF7 cells together.

To further investigate the parameters which determined the signal-to-noise ratio of this assay, different incubation times were trialed (Figure 2.4A). In addition, different ratios of CTLs to target cells were trialed (Figure 2.4B). It was found that within the first 4 hours of observation, higher ratios of CTLs to target cells increased the signal-to-noise ratio, as observed in other studies (Cerignoli et al., 2018; Khandelwal et al., 2015; Somasundaram et al., 2005). With the longer incubation time of 19 hours however, the previously observed trend of higher calcein release from the positive control was reversed, probably as a result of active efflux of calcein from the target cells which were still alive. As an incubation time of roughly 24 hours would realistically be necessary for a ICI screen, this finding showed that this assay would not be applicable.

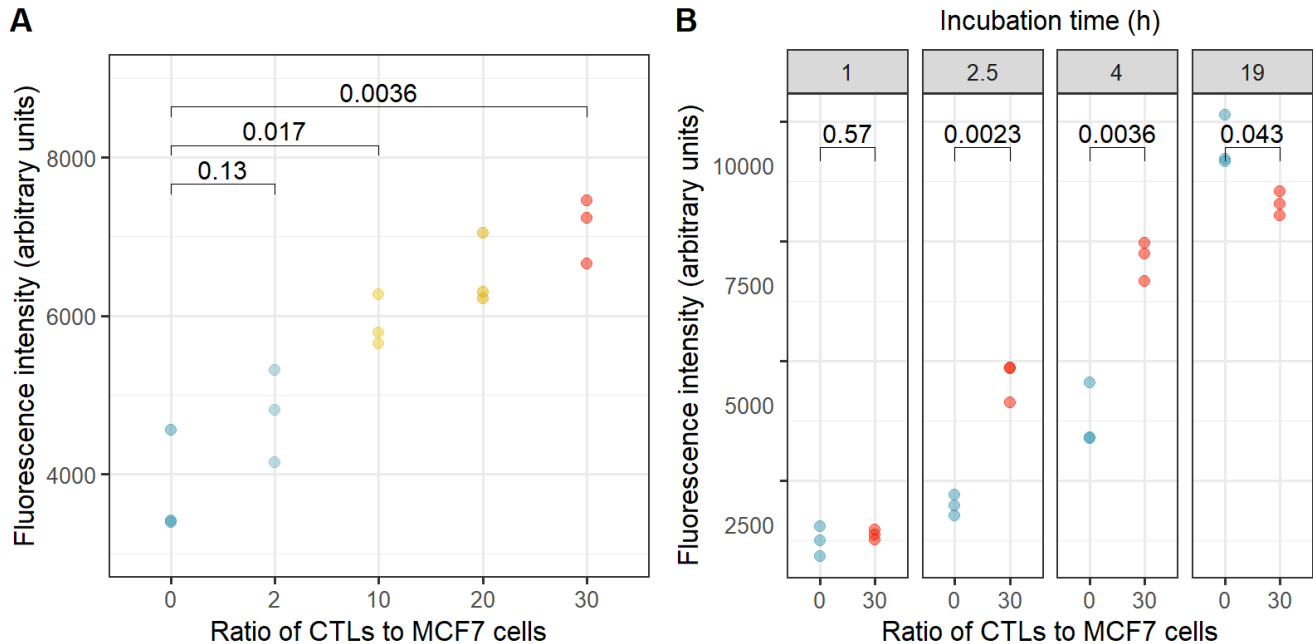


Figure 2.4 MCF7 cells were stained with Calcein-AM green and incubated with bispecific antibody and pre-activated CTLs. Supernatant from the cell mixtures was removed and green-fluorescence measured as an indicator of cell death. p-values were computed using two-tailed t-tests. A) Increasing the ratio of CTLs per target cell increases the rate of fluorescence release. B) At longer incubation times, calcein-AM green is released independent of whether CTLs are present. After 19 h, the positive control no longer exhibits higher cell death than the negative control.

Caspase-3 detection as a proxy for apoptosis

The next approach trialed for detecting CTL-induced MCF7 cell death was via a commercial apoptosis assay, which had already been used for previous drug screens in plugs (Eduati et al., 2018). This used a Rhodamine-110 conjugated substrate of caspase-3, which would be cleaved in the presence of caspase-3, thus unquenching the Rhodamine-110 and generating a fluorescent product. As CTL-induced cell death occurs via apoptosis, and most apoptotic pathways act via caspase-3, this assay allowed CTL-induced cell death to be measured. This assay was trialed based on the assumption that the CTLs would not experience any significant cell death over the course of the assay. Unfortunately, as seen in Figure 2.5 this assumption was disproven.

After 20 hours, the cell death from CTLs alone led to a mean fluorescence level of 3203 AU, while that of the other negative control, MCF7 alone, was 2682 AU. In contrast, the combination of both cell types in the absence of bispecific antibody led to a mean fluorescence level of 8035 AU, which is significantly

higher than the sum of both single cell-types. The positive control with all three components was 8800 AU. This indicates increased non-specific cell death in the cell mixture negative control vs. the single cell type negative controls, probably as a result of a positive feedback loop of dead cells releasing reactive oxygen species (ROS), which lead to death of neighboring cells and release of more ROS etc. As such, the signal-to-noise ratio between the cell mixture negative control and the positive control is not very large, although it is distinguishable with a p-value of 0.0014. More critically, the high rate of background CTL death is very concerning, because it suggests the possibility that one treatment could lead to increased CTL death, while another led to increased CTL activity, and these two situations would be indistinguishable. In addition, we anticipated that the scale of difference in cell death induced by treatment with an ICI would be much smaller than the difference between the negative and positive controls. If this is correct, any effect of ICI treatment is unlikely to be distinguishable. Given these arguments against the use of a generic caspase assay readout, we chose not to pursue the use of this readout for ICI screens.

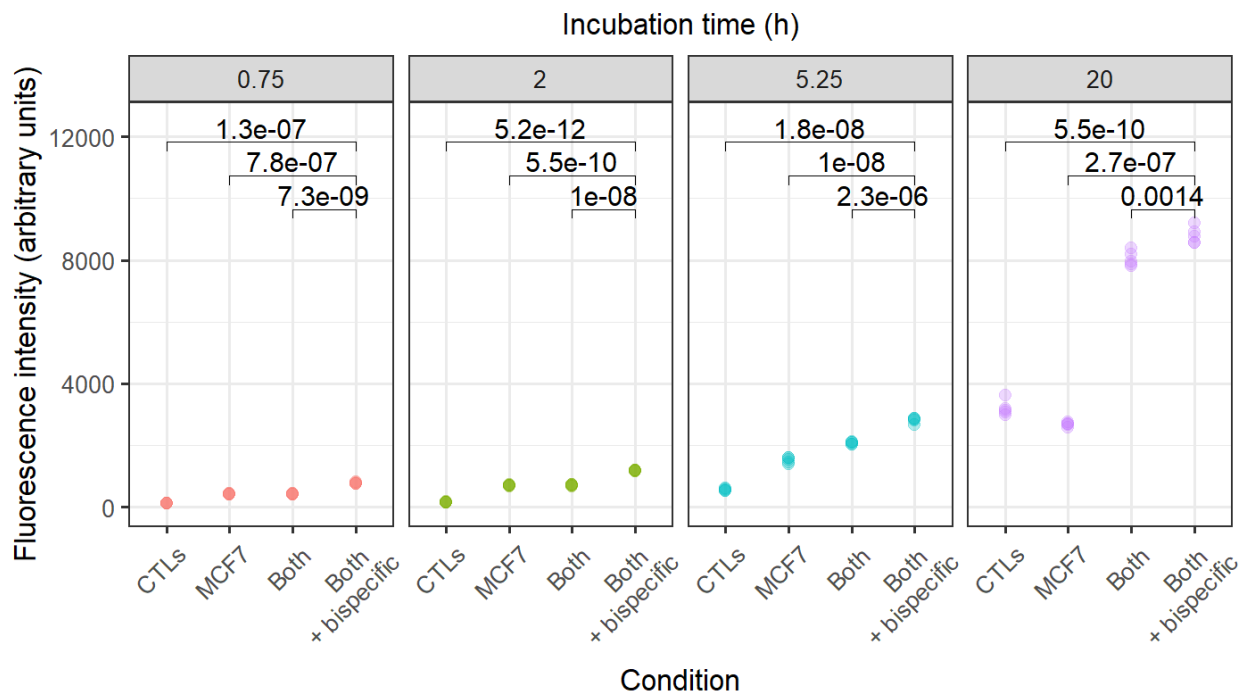


Figure 2.5 Target MCF7 cells were mixed together with caspase assay reagent, pre-activated cytotoxic T-lymphocytes (CTLs) and bispecific antibody which bound EpCAM on the MCF7 cells and CD3 on the CTLs. Between 2-5.25 h of incubation led to induction of CTL-mediated target cell death, but background rates of cell death in both cell types led to very high signal-to-noise ratios in the longest incubation time (20 h). p-values were computed using two-tailed t-tests.

Outlook

This work showed the successful selection and activation of primary human CTLs, and the use of those CTLs to induce cell death in target cells. Although this induced cell death could be measured in two different ways, we concluded that both proposed readouts for ICI screens were not appropriate for the timeframe that was required. As such, we concluded that significant further technology development was required before an ICI screen could be developed. One promising approach for future ICI screens would be via transcriptomics of treated cells, if the transcriptomes of target cells and CTLs could be distinguished. As such, we decided to focus on developing transcriptomics-based readout of microfluidic drug screens, before further developing the ICI approach.

Developing a microfluidic workflow for combinatorial drug screens on cancer cells with transcriptomic readout

Overview of proposed workflow

In order to perform high-throughput drug screens on small numbers of cancer cells, the Braille Display (BD) valving device has previously been used to produce microfluidic plugs with cells, fluorescent caspase assay reagents and different pairs of drugs (Eduati et al., 2018). The fluorescence-based data from this screen enabled direct identification of several cell-line specific treatments, and logic models built from the data even allowed a number of effective conditions to be predicted, which had not been in the original screen (Eduati et al., 2020). Generation of richer data from microfluidics-based drug perturbations would significantly improve such logic models, as information about all perturbed pathways could be obtained, rather than a single end-point (caspase activity).

Dr. Lukas Mathur developed an initial workflow based on combining plugs from a BD valving chip with input from an autosampler device (which injected drugs sequentially aspirated from a microtitre plate) to produce a droplet emulsion with different drug pairs (Figure 1.7). The significant limitation of this workflow was that it was far too complex for clinical application. Furthermore, it is well established that sensitivity of cancer cells to drug treatment is heavily influenced by cells in the surrounding area, and the cytokines that they release. In order to apply this platform where it is most valuable, on solid tumor biopsies, cells must be perturbed as pools of cells rather than single cells, to reproduce as much as possible of the physiological conditions which are experienced within solid tumors. In addition, Dr. Mathur's workflow could only be applied with drugs which were very hydrophilic ($\log P < 0$ in the best case), which severely limited the range of drugs which could be tested. As a result, an alternative workflow was proposed in which drug combinations were produced in microfluidic plugs (as in the original caspase-assay-based screens), but with drugs accompanied by deterministic DNA barcode fragments (Figure 2.6), as developed by Dr. Mathur.

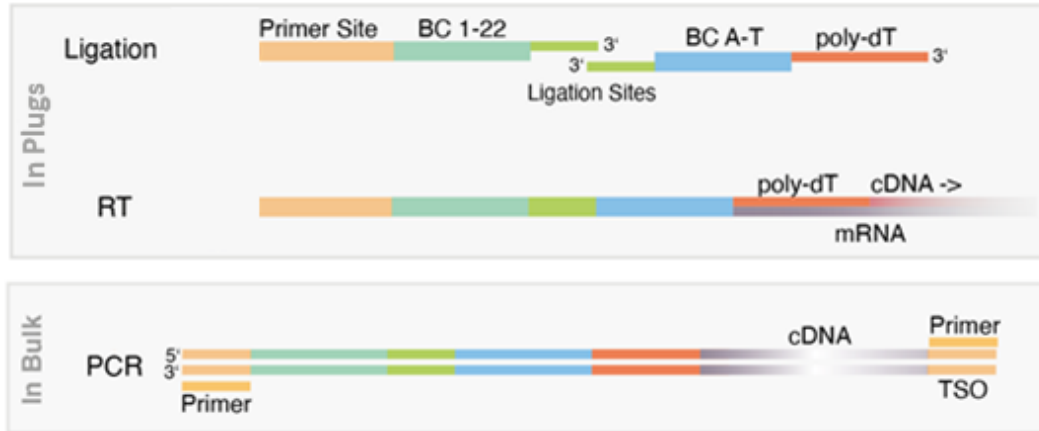


Figure 2.6 Adapted from Mathur et al., 2021. Combinatorial DNA barcoding approach in which pairs of drug-specific DNA barcode fragments are combined in a ligation reaction to create a full-length DNA barcode which is incorporated into cDNA during reverse transcription to encode a pairwise drug treatment. Each pair of fragments includes a PCR-priming fragment and a reverse transcription-priming fragment. Full length cDNA can be extracted and amplified via the two identical PCR primer sites which are present on the PCR-priming fragment and the template switching oligonucleotide (TSO).

The proposed new workflow for screening pairs of targeted drugs on cancer cells, with a transcriptomic readout is shown in Figure 2.7. Firstly plugs containing target cells together with different pairs of drugs and barcode fragments are produced. To do this, each drug is mixed with a specific DNA barcode fragment, and each mixture is then continually injected into the BD valving chip. The valves produce plugs of different chemical composition, by directing drug-barcode mixtures either to waste, or to plug production. After 16 hours incubation of the plugs, reverse transcription mixture is added to each plug using a droplet-injection device. The reagent mixture contains reagents to ligate the two DNA barcode fragments together, lyse the targeted cells and carry out first-strand synthesis from the released mRNA. The plugs are heated to 42°C for 90 minutes to allow the reactions to occur. Importantly, reverse transcription is primed by the poly-dT tail of the newly ligated DNA barcode. This ensures that the resultant cDNA is barcoded with the identities of both drugs used in that treatment condition. Incorporation of template switching oligo (TSO) into the 3' end of the nascent cDNA during reverse transcription ensures that full-length cDNA can be amplified, via a primer sequence at the ends of both the TSO and the combinatorial barcode. This amplification approach and the corresponding primer sequence was taken from the SMART-Seq2 workflow for sequencing of single cells (Picelli et al., 2014). Following amplification of cDNA purified from pooled plugs, the library is tagged and sequenced.

Development of this workflow required integration of various pieces of work previously carried out in the Merten group. To bring these pieces together, elements had to be further developed and optimized to make them compatible with each other.

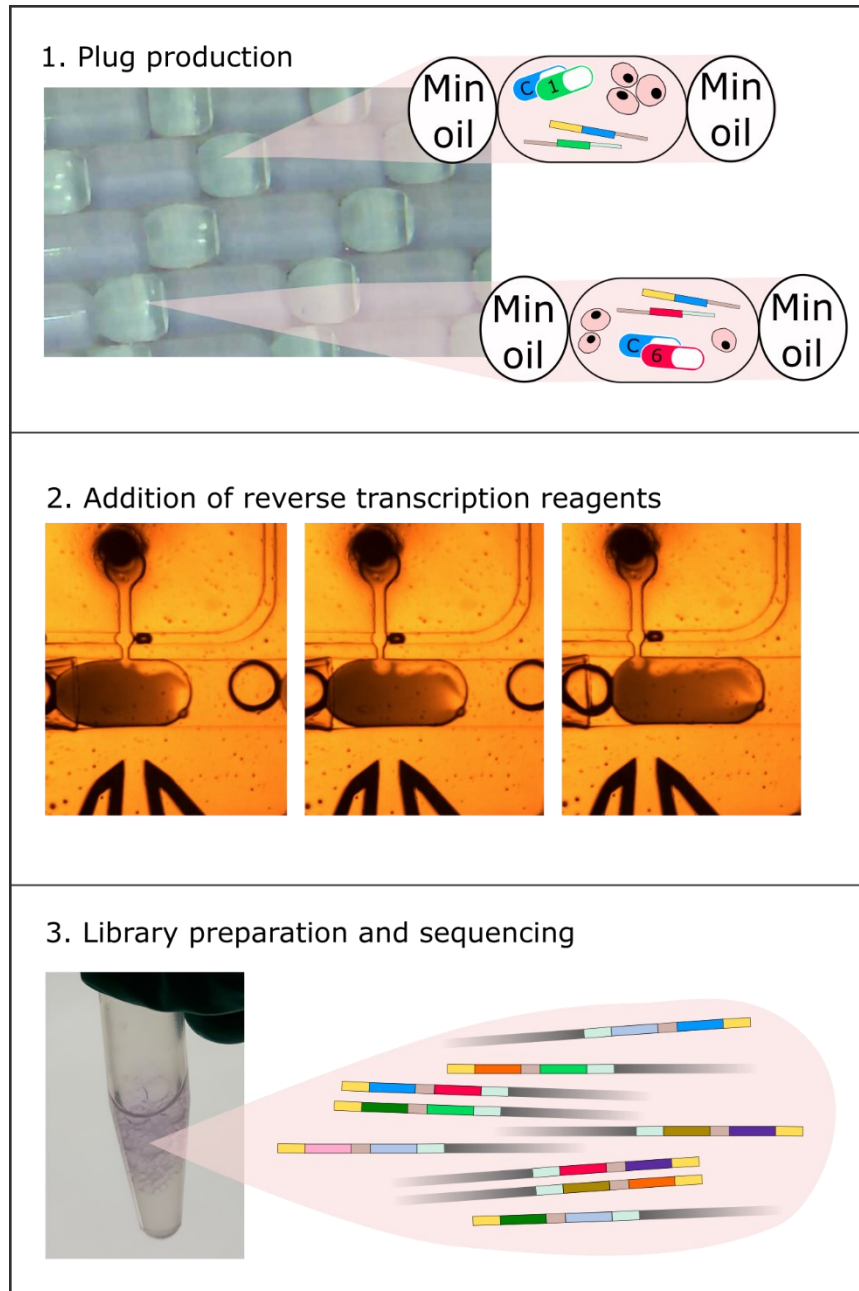


Figure 2.7 Overview of workflow for drug screening in plugs, with transcriptomic readout. Firstly, plugs are produced with the BD valving device, containing pairs of drugs, DNA barcoding fragments and cells. They are stored sequentially in a length of gas-permeable tubing. After 16 hours of incubation, reagents are added using the droplet-injection device. These allow ligation of DNA barcode fragments together, lysis of treated cells and reverse transcription of the released mRNA. After these reactions have occurred, cDNA is extracted from plugs, purified, amplified, tagmented and sequenced.

Introducing reagents into plugs

In order to add reverse transcription reagents to plugs, a new device was required, which would be suitable for addition of reagents to microfluidic plugs. It is necessary to use a different type of device rather than a pico-injector, as Dr. Mathur did, because the large size of plugs (and the correspondingly large volume of reagent which must be added) makes them incompatible with picoinjection. In 2014, Dr. Dominic Eicher from our group made an initial prototype device for the injection of reagents into plugs (design shown in Figure 2.9A). This device essentially consisted of a single main channel, through which plugs could be injected, and a droplet-maker which created surfactant-stabilized droplets of reagent. Electrodes aligned with the droplet-maker allowed fusion of plugs with the incoming reagent droplets. Incoming reagents were encapsulated into droplets so that they would not fuse with nearby plugs unless electrodes were present and activated at that location. If infused reagent was not encapsulated into surfactant-stabilized droplets, reagent flow which came between droplets would get added to the preceding plug, regardless of how long the gap was between plugs. As such, plugs with larger spacing to the next would receive more reagent than plugs which were closely followed by another plug. By encapsulating reagents directly into surfactant-stabilized droplets, reagent was either directly added to a perpendicular plug or remained within stable droplets and did not fuse with any plug. This prevented reagent addition rate from varying as a result of varying spacing between plugs. Another feature of this device was the side inlets which created an oil sheath to prevent plugs from contacting the PDMS channel walls and causing wetting.

When starting my project at the end of 2019, a number of issues needed to be solved before this device could be used.

- New droplet-injection molds needed to be produced.
- A robust protocol for production of droplet-injection chips needed to be designed.
- The surfactant used by Dr. Eicher was no longer available, and would need to be replaced by pico-surf. It was unclear how this would affect droplet production and introduction of plugs into the device.
- The efficacy and consistency of droplet injection needed to be evaluated.

To start with, I made and measured a new droplet-injection mold. As the required depth of the droplet-injection channel was significantly greater than the measurement range which could be achieved with the standard profilometer, the profilometer could not be used to determine channel depth. Instead, a PDMS chip was produced from the mold, then cut open and the cross section was imaged. Since channel width was directly set by the predetermined channel width of the photomask, FIJI could be used to measure the channel width and depth of the cross-section image, such that the channel depth (Figure 2.8, B) could be calculated proportional to the channel width (Figure 2.8, A). For the successful mold which was used for further experiments, this calculation gave a channel depth of 390 μm , which is sufficiently close to that reported by Dr. Eicher (500 μm).

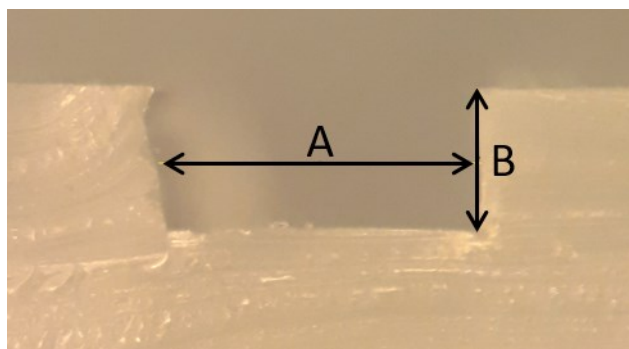


Figure 2.8 Measurement of channel depth for exceptionally deep devices was done via comparison of channel width (A), dictated by width of structures in the photomask, with channel depth (B), dictated by photoresist viscosity and spin-speed during photomask coating.

I trialed a number of different methods for the production of droplet-injection chips from the successful mold. This eventually culminated in the robust protocol described in the methods section of this thesis. Briefly, the PDMS chips were cut from the mold, inlets and outlets were punched and the chip was bonded to a PDMS membrane. A length of plug-collection tubing was inserted horizontally into the plug-injection channel, and the chip with tubing inserted was then glued to an ITO-coated glass slide. It was previously found that microfluidic plugs must be injected horizontally into chips, rather than vertically to avoid plug-breakup and resultant cross-contamination (Clausell-Tormos et al., 2010). To enable horizontal injection for this device, it was found that the PDMS should be cut through the channel as close as possible to the inlets for sheath oil. This ensured that the fragile plug-tubing had a minimum distance to be inserted into the chip, in order for plugs to enter the chip after the sheath oil junction (Figure 2.9B, white arrow). It was also found that the standard membrane thickness used for

BD chips was unsuitable for this device, as it was thin enough to be easily ripped during insertion of plug tubing. As such, a thicker membrane was produced. Various glues were also tried, in order to seal the plug tubing into the chip. It was found that epoxy glue performed best, because it was highly viscous and therefore did not flow into the tubing inlet and block the chip, as other glues had done.

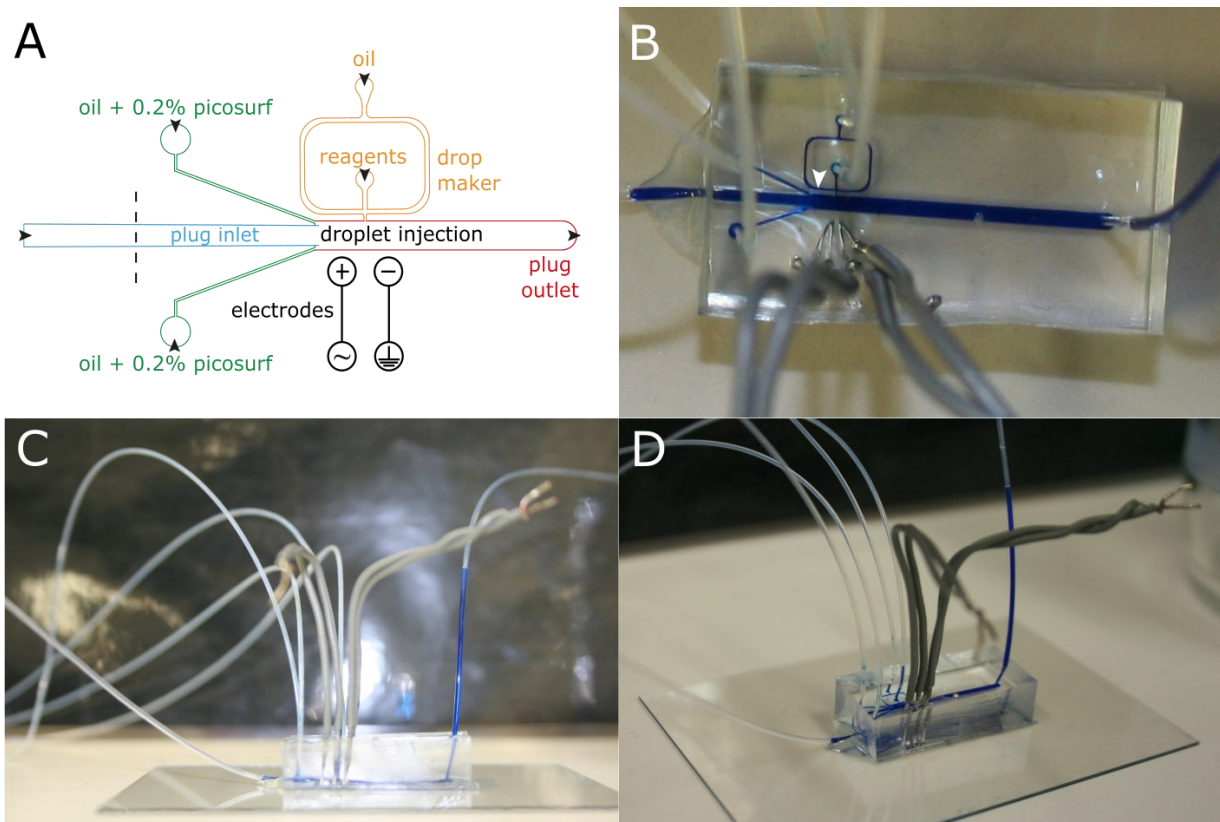


Figure 2.9 A) Droplet-injection chip design (adapted from PhD thesis of Dominic Eicher). Plugs are infused horizontally into the chip, entering just after the junction of the sheath oil inlets (green). Once in the droplet-injection device, plugs have reagents added to them only when they are in the channel space between the droplet-maker and the electrodes. Dotted line indicates where the PDMS chip should be cut to allow insertion of the plug collection tubing sufficiently far into the chip. B-D) Images of the droplet-injection chip from different angles (images and chip my own). White arrow in B indicates where the plug collection tubing should reach in order to avoid wetting as plugs enter the chip.

With a robust protocol established for production of droplet-injection chips, I started testing the droplet-injection workflow. Initially, very extreme wetting was observed, such that plugs fused continuously and large-scale cross-contamination occurred (Figure 2.10A). The extremity of this wetting can also be seen by the very low contact angle between the plug and channel walls in Figure 2.10A. By increasing the concentration of surfactant in the side inlets to 0.2% and optimizing the surface

treatment of the chip, plugs no longer fused continuously (Figure 2.10B). Unfortunately, adjacent plugs still frequently fused with each other (causing cross-contamination), as a result of intervening mineral oil spacers becoming attached to the device walls. I found that producing plugs with half the rate of FC-40 flow decreased the dead volume between plugs and mineral oil spacers, such that mineral oil spacers no longer attached to the channel walls (Figure 2.10C).

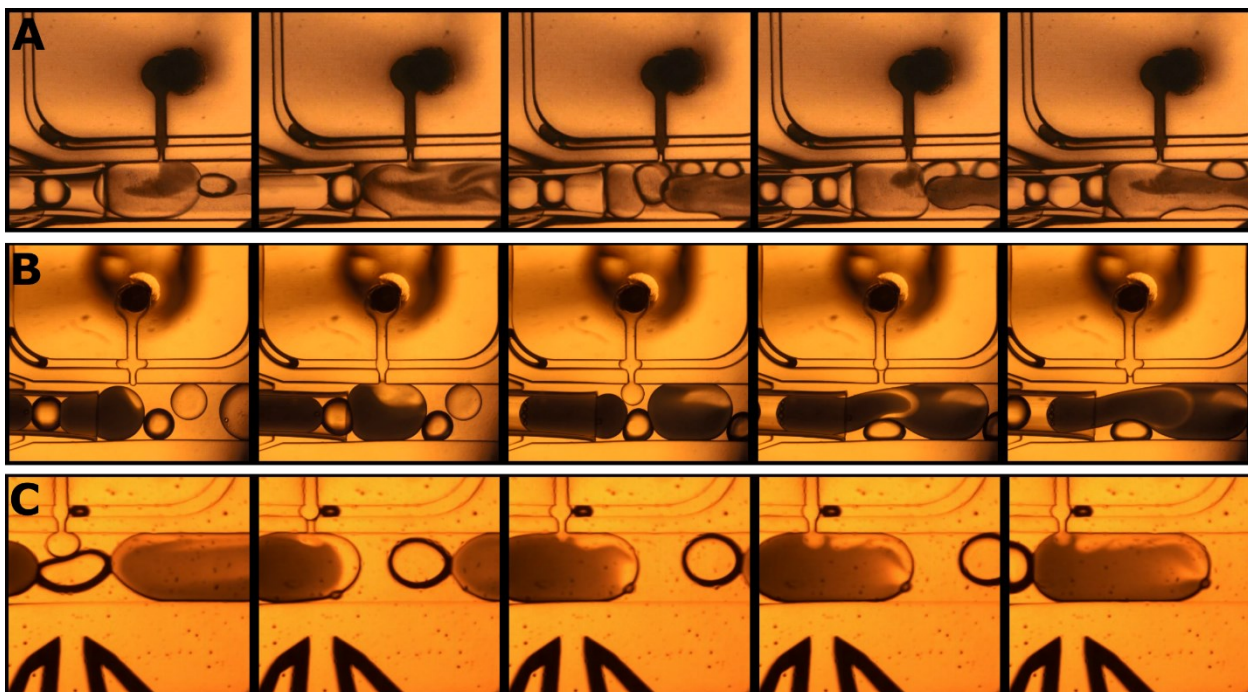


Figure 2.10 Development of the droplet-injection workflow. A) Initially, large-scale wetting and cross-contamination occurred. B) Optimization of channel surface treatment and sheath oil surfactant concentration significantly reduced wetting, but mineral oil became stuck on the channel walls, leading to frequent fusion of adjacent plugs. C) Reduction in speed of FC-40 carrier oil during initial plug production meant that there was significantly less dead volume between plugs and mineral oil spacers, such that mineral oil no longer became stuck to the channel walls.

Once the droplet-injection workflow was working robustly, with no visible cross-contamination, I wanted to quantify this. To assess the consistency of injected volume and to determine whether some degree of plug fusion or breakup was occurring, I measured addition of fluorescein into 180 plugs. To do this, I produced 18 sets of 10 orange sample plugs (containing the fluorophore AF594), each interspaced by 5 blue barcoding plugs (containing the fluorophore cascade blue) (Figure 2.11A). I then added green dye (fluorescein) into each plug via the droplet-injection device, and measured the fluorescence in each plug. The fluorescence data was then analyzed with the BraDiPlus package

(<https://github.com/saezlab/BraDiPluS/blob/master/README.md>) to identify each set of 10 sample plugs, based on the location of the blue barcode plugs. By using orange dyed sample plugs, each plug could be identified based on the orange fluorescence and the green fluorescence intensity could be quantified. This ensured that even if sample plugs did not receive green dye, they would still be identified and their green fluorescence level quantified.

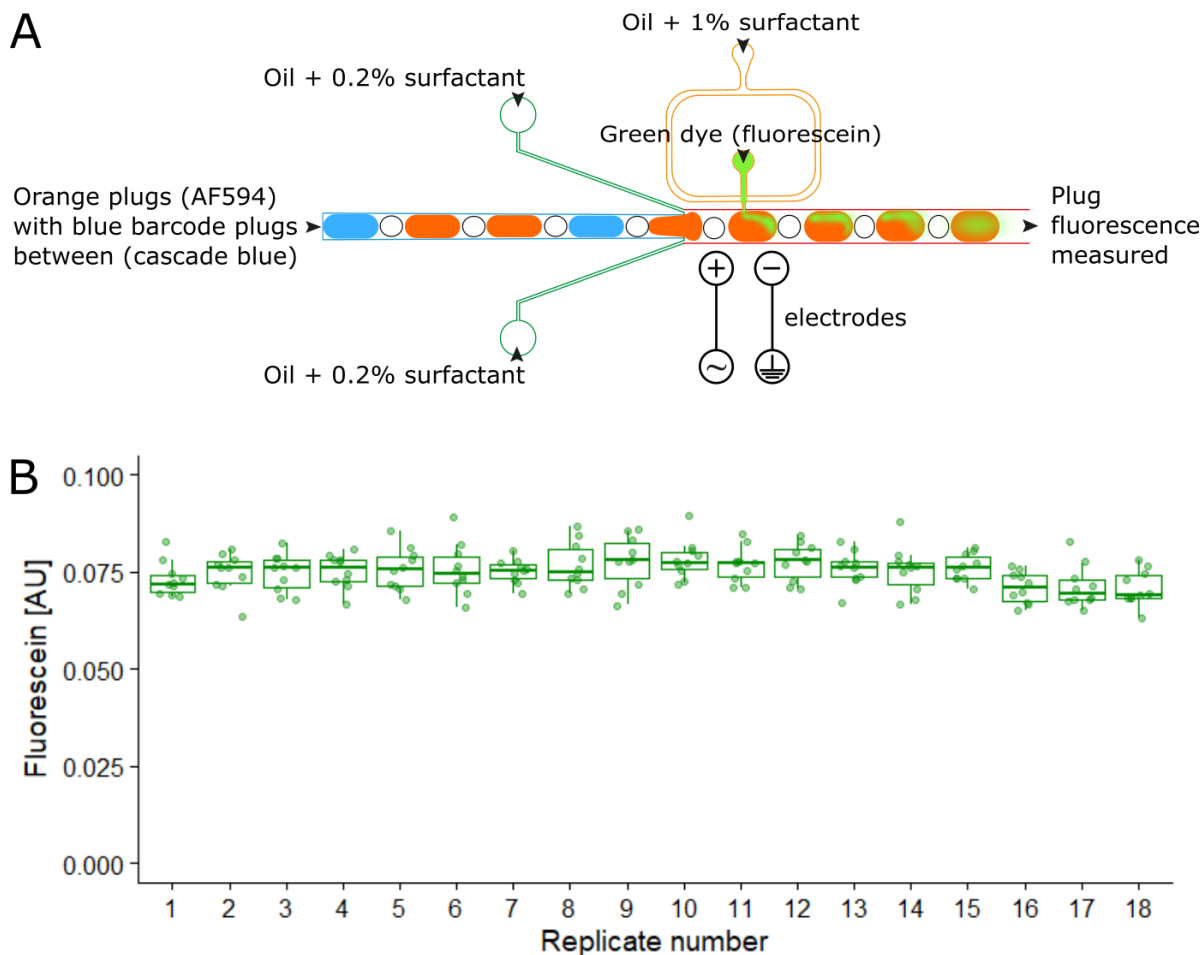


Figure 2.11 Quantification of droplet-injection consistency. A) Sets of 10 orange plugs interspersed with 5 blue barcode plugs were produced, and green dye was then added to these using the droplet-injection device. B) Measurement of plug fluorescence after droplet-injection showed that all sample plugs received green dye from the droplet-injection device, and at a consistent quantity. No plug fusion or breakup was observed, as seen by the consistent presence of exactly 10 plugs per set.

This experiment showed that the droplet-injection workflow was very consistent. All sample plugs received green dye from the droplet-injection device, and at a consistent quantity (Figure 2.11B). No plug fusion or breakup was observed, as seen by the consistent presence of exactly 10 plugs per set.

With droplet-injection working consistently over a large number of plugs, I was able to proceed with developing the rest of the transcriptomic workflow.

Chemical agents for lysis in plugs

In order to analyze differences in gene expression between treatment conditions, target cells must be lysed so that cellular mRNA can be extracted and cDNA produced. Related workflows use detergents to lyse cells (Klein et al., 2015; Macosko et al., 2015) because this lyses cells extremely quickly. This means that cells do not have enough time to alter their gene expression as a stress response when lysis begins, which would lead to confounding signatures in the transcriptomic data. Detergent-based lysis is also simple, reliable and cheap. With this in mind, detergent-based cell-lysis was highly desirable as the method of cell lysis for my workflow. Specifically, IGEPAL CA-630 at 0.3% (v/v) final concentration would have been the default choice of lysis buffer, as this was already used internally in the work by Dr. Mathur. As plugs have significantly lower stability than surfactant-stabilized droplets, it was unknown whether phase separation would be maintained if IGEPAL CA-630 was added to plugs. Maintenance of phase separation is essential, as large-scale fusion of plugs would lead to levels of cross contamination which would render the results unusable.

To test the effect of IGEPAL CA-630 on plug stability, an initial qualitative experiment was done by making a large number of PBS-filled plugs, then adding PBS or IGEPAL CA-630 to each plug by droplet-injection. IGEPAL CA-630 was added at 0.9% (v/v) to plugs, so that the final plug concentration would be 0.3% (v/v). This experiment clearly showed that phase separation was not maintained when IGEPAL CA-630 was added at this concentration (Figure 2.12). Large-scale fusion of adjacent plugs was observed, and mineral oil spacers were engulfed by the aqueous plugs when IGEPAL was added. This was in contrast to when PBS alone was added, which had no effect on the mineral oil- aqueous plug interface (Figure 2.10C). This clearly showed that another chemical lysis method was required, to extract mRNA from target cells.

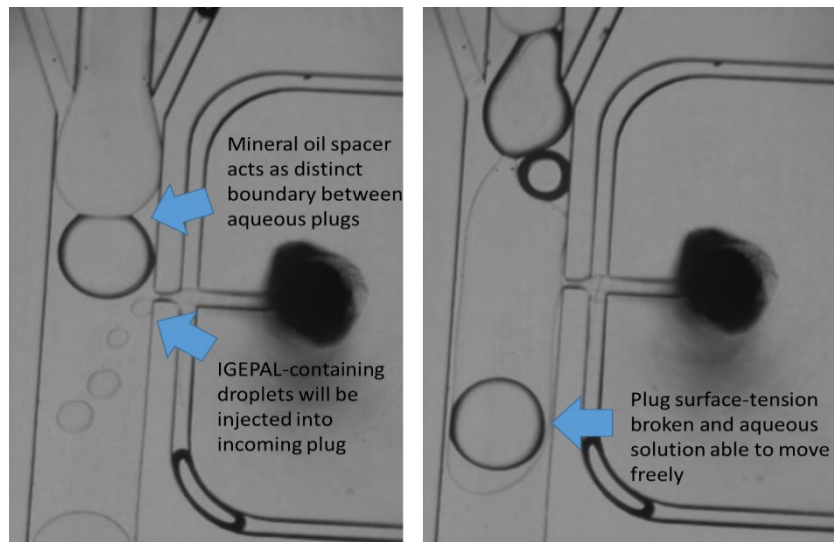


Figure 2.12 Addition of IGEPAL CA-630 to aqueous plugs caused breakdown of phase separation and cross-contamination between plugs.

To identify an alternative lysis agent, three lysis buffers were trialed based on literature concentrations of different detergents: Perm/wash buffer (manufacturer's instructions), Sarkosyl (Macosko et al., 2015) and SDS (Goldenberger et al., 1995). I also trialed lower concentrations of IGEPAL (0.03%, or 0.003% final concentration (v/v)). In order to systematically compare this range of buffers, the BD valving device was used to produce different sets of fluorescent plugs containing the different lysis buffers at final concentrations matching the concentration required for cell lysis, based on literature. The fluorescent intensity of the plugs were then measured to determine whether the number of plugs per set and plug length varied in comparison to PBS-only plugs, as this would indicate that plugs were fused together or broken apart more easily when they contained that detergent (Figure 2.13A). This showed that the lysis agent with the lowest variation was Perm/wash buffer (based on saponin), with Igepal at 0.003% (v/v) being the second least variable.

The cell lysis capabilities of these detergents was then evaluated, by comparing them to Igepal at 0.3% (v/v) as a positive control, or nuclease-free water as a negative control. To do this, a K-562 cell line expressing the green-fluorescent protein Zs-green was used. This was chosen because Zs-green is highly unlikely to be an environmental contaminant, so detection of Zs-green mRNA from lysed cells is very specific. Each lysis agent was mixed with Zs-green expressing K-562, then reverse transcription was

carried out on this mixture, and the amount of Zs-green cDNA was quantified using qPCR (Figure 2.13B). From the qPCR results, lysis with Perm/wash buffer or 0.3% (v/v) Igepal CA-630 led to significantly higher levels of Zs-green cDNA being amplified, than for 0.003% (v/v) Igepal. This is likely due to the fact that 0.003% (v/v) Igepal is too dilute to induce efficient lysis. Given the fact that Perm/wash was able to be used in plugs without disturbing phase separation, and that it was able to release comparable volumes of cDNA as Igepal CA-630 at 0.3% (v/v), I chose to proceed with Perm/wash as my cell lysis buffer.

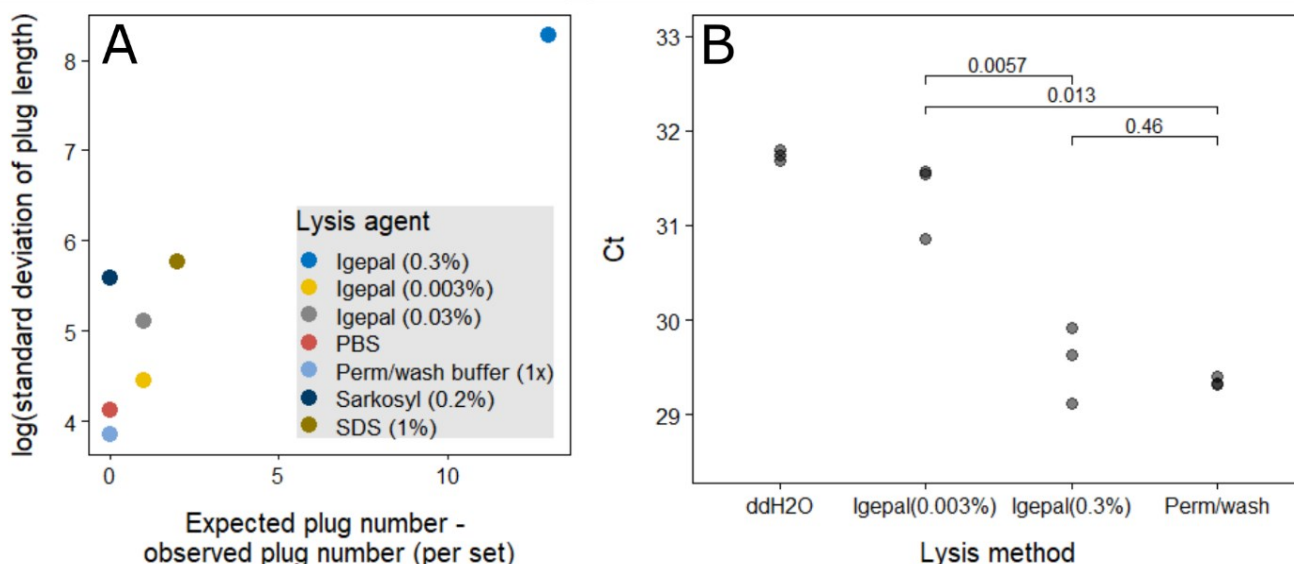


Figure 2.13 Screening of different chemical agents for cell lysis. A) Sets of 20 fluorescent plugs were produced containing each of the different lysis agents at the final concentration used in literature for cell lysis (or PBS as a negative control). Plug length and number of plugs per set were then evaluated based on fluorescence measurements, and the results were plotted against each other. B) The lysis agents with the lowest variation (and Igepal at 0.3% (v/v), as a positive control) were used to lyse K-562 cells expressing zs-green. Reverse transcription was then performed on this lysate, and zs-green cDNA was quantified by qPCR. Replicates are qPCR technical replicates using the same cDNA input. p-values were computed using two-tailed t-tests.

[qPCR to assess microfluidics workflow](#)

With a robust droplet-injection workflow, and a lysis agent which both allows sufficient mRNA release and does not affect plug stability, I wanted to now test reverse transcription in plugs. To do this, I first designed a number of simpler barcodes which only contained a DNA barcode sequence and a poly-dT sequence, without the need for ligation. As seen in Figure 2.14, the barcoded poly-dT sequence could

capture mRNA, allowing reverse transcription to be primed. The DNA barcode was 32 bp long, making it large enough for binding of a qPCR primer. The expression level of genes of interest and the treatment condition could then be determined based on choice of primers used for a qPCR reaction.

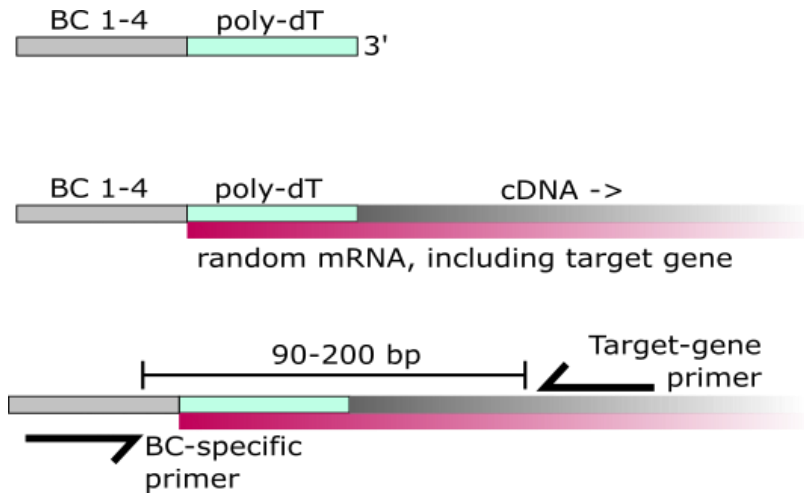


Figure 2.14 qPCR barcodes were designed which allowed mRNA to be captured, and reverse transcribed such that a treatment-specific qPCR primer site was incorporated. The expression level of a gene of interest, and the treatment condition could then be determined based on choice of primers in the qPCR reaction.

I chose to use K-562 cells for qPCR validation experiments and for combinatorial drug screens, primarily because K-562 was used in the workflow development by Dr. Mathur. He chose it because it is a suspension cell line, so has a reduced tendency to form cell clumps, which would block the channels of the BD valving chip. Such blockages would be particularly detrimental for transcriptomics-based drug screens, because large variations in cell number between conditions could lead to confounding effects in the transcriptomic data. In addition, it is a well studied suspension cell line, as it is part of the NCI-60 cell line panel (Shoemaker, 2006). In particular, its response to the targeted therapy Imatinib has been well studied, because K-562 is a classic Chronic Myelogenous Leukemia (CML) cell line. This means that it harbors the reciprocal translocation between chromosome 9 and 22 which produces the BCR-ABL oncogene: the target of Imatinib.

To investigate the specificity and amplification efficacy of the newly designed qPCR barcodes, I mixed K-562 cells in PCR tubes with each of the simple barcodes, then added reagents for reverse transcription and Perm/wash buffer for cell lysis. After incubating for 90 minutes at 42 °C, I purified the single-

stranded cDNA using AMPURE XP-beads. The purified cDNA was then added with a primer towards the 3' region of Gapdh to different wells of a qPCR plate, together with different barcode-specific primers. As expected, amplification was only observed in wells in which the barcode primer matched the barcode-dT sequence used for reverse transcription (Figure 2.15). This proved that qPCR-based amplification was barcode specific, thus allowing treatment condition to be detected based on choice of qPCR primer.

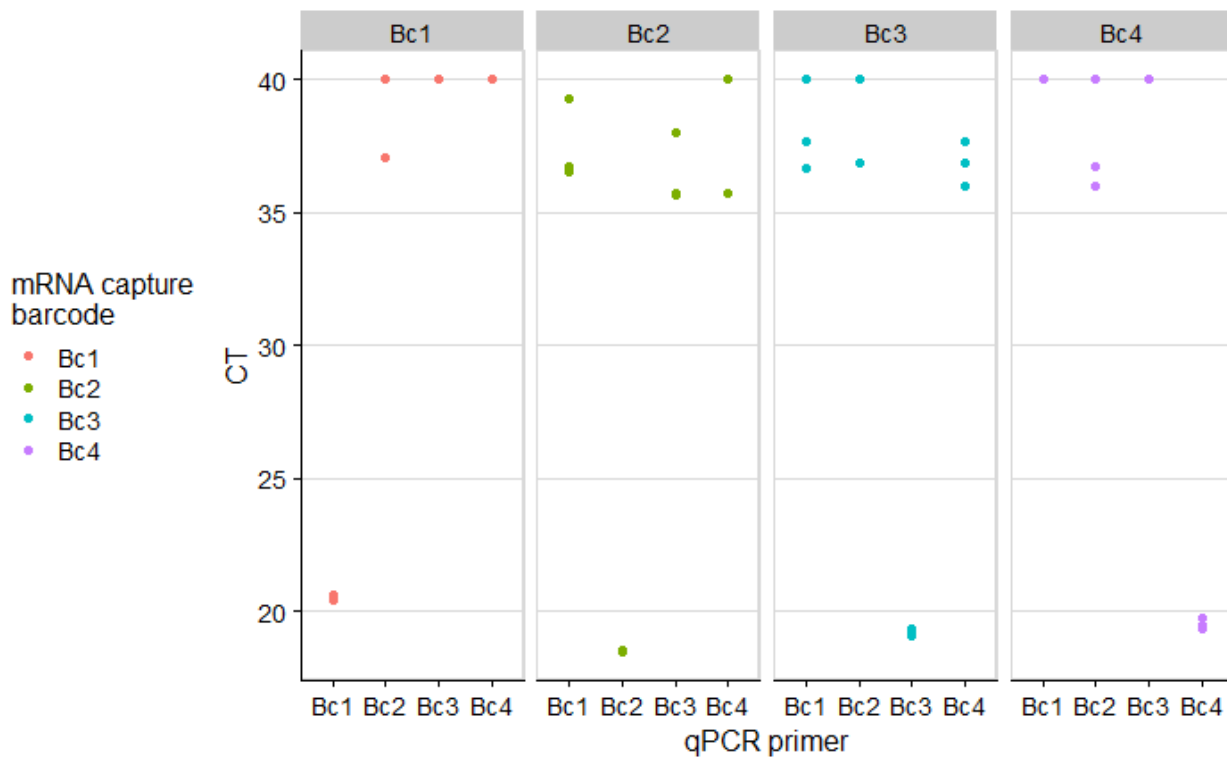


Figure 2.15 Separate reverse transcription reactions were carried out using each of the 4 poly-dT tagged qPCR barcodes. Then the cDNA was purified and quantified by qPCR using a primer towards GAPDH combined with different barcode-qPCR primers. Amplification was only observed when the barcode primer matched the poly-dT barcode.

In order to identify genes which were likely to be consistently differentially regulated in K-562 cells upon treatment with Imatinib, I used the “GEO2R” tool of the Gene Expression Omnibus(GEO) to run an automatically generated limma script (Ritchie et al., 2015) on published data. I used two microarray-based studies, where gene expression changes were determined following treatment of K-562 cells with DMSO or Imatinib for 12 or 24 hours respectively (Håkansson et al., 2008; Neumann et al., 2007). For

each dataset, this analysis determined magnitude of differential expression between DMSO and Imatinib treatment. Data was given in the form of log(fold-change) with significance in the form of p-value, adjusted p-value, moderated t-statistic and B statistic. The top 250 genes (ranked by B-statistic) were exported for each dataset, and the genes which were common to both datasets were identified (Table 1).

adj.P.Val	P.Value	t	B	logFC	Gene.symb	Gene.title	Study
4.22E-05	2.65E-08	24.254693	9.822797	2.2029035	PODXL	podocalyxin like	GSE19567
6.03E-05	5.60E-08	21.888483	9.181133	3.5709654	SPTA1	spectrin alpha, erythrocytic 1	GSE19567
6.76E-05	8.49E-08	-20.66952	8.810611	-2.54218	SOCS2	suppressor of cytokine signaling 2	GSE19567
7.25E-05	9.44E-08	-20.37235	8.715682	-3.88333	EGR1	early growth response 1	GSE19567
7.52E-05	1.02E-07	-20.15671	8.645607	-2.029568	SOCS2	suppressor of cytokine signaling 2	GSE19567
7.62E-05	1.40E-07	-19.28786	8.352707	-2.471085	EGR1	early growth response 1	GSE19567
7.93E-05	1.67E-07	18.826948	8.190121	2.7147728	SLC25A37	solute carrier family 25 member 37	GSE19567
8.93E-05	2.37E-07	-17.94275	7.863215	-1.59459	CTSH	cathepsin H	GSE19567
8.93E-05	2.42E-07	-17.88334	7.840512	-2.62954	PIM1	Pim-1 proto-oncogene, serine/threonine kinase	GSE19567
0.000116	3.85E-07	16.772342	7.397529	2.1311084	ADD2	adducin 2	GSE19567
0.000124	5.04E-07	16.155816	7.13569	1.7159143	TSC22D1	TSC22 domain family member 1	GSE19567
0.0008689	1.42E-05	10.082591	3.722023	2.2240128	SLC25A37	solute carrier family 25 member 37	GSE19567
0.0015927	3.85E-05	8.717074	2.658612	3.0927848	SLC25A37	solute carrier family 25 member 37	GSE19567
0.009851	0.000683	5.596241	-0.447447	1.0285844	ADD2	adducin 2	GSE19567
0.3808753	0.196	1.422058	-6.30118	0.7621174	ADD2	adducin 2	GSE19567
0.204	4.23E-05	-9.845856	1.75464	-2.950841	PIM1	pim-1 oncogene	GSE10283
0.204	5.39E-05	-9.45798	1.62314	-2.902125	PIM1	pim-1 oncogene	GSE10283
0.204	7.99E-05	-8.85654	1.39857	-2.54219	SOCS2	suppressor of cytokine signaling 2	GSE10283
0.212	0.0001111	-8.379559	1.20052	-2.626641	PIM1	pim-1 oncogene	GSE10283
0.252	0.0003068	-7.043427	0.53244	-2.252003	EGR1	early growth response 1	GSE10283
0.311	0.000777	-5.975728	-0.15063	-1.766094	CTSH	cathepsin H	GSE10283
0.312	0.0015942	5.2357767	-0.72094	1.505576	ADD2	adducin 2 (beta)	GSE10283
0.344	0.0034662	4.5079348	-1.37213	1.5306835	SLC25A37	solute carrier family 25, member 37	GSE10283
0.344	0.0037032	4.4490153	-1.42905	1.8659888	SPTA1	spectrin, alpha, erythrocytic 1 (elliptocytosis 2)	GSE10283
0.354	0.0040597	4.3678949	-1.50847	1.5444321	PODXL	podocalyxin-like	GSE10283
0.362	0.0045559	4.2673095	-1.60867	1.6980492	TSC22D1	TSC22 domain family, member 1	GSE10283
0.389	0.0067389	3.9352215	-1.95305	1.3259569	SLC25A37	solute carrier family 25, member 37	GSE10283

Table 1. Table of genes which were most significantly upregulated across two published studies: GSE19567 and GSE10283.

Where possible, primers were designed towards the 3' end of each of the commonly differentially regulated genes (as shown in Figure 2.14). It was not possible to design primers towards every gene however, because each primer needed to bind within 90-200 bp of the 3' end of the gene, and for many genes there was no good primer binding site within this region. The genes for which primers were made, were therefore: PIM1, EGR1, SLC25A37 and SPTA1. Literature analysis of these genes provide

mechanistic explanations for the up- or down-regulation of each of these genes, thus confirming that this is a relevant panel of genes to assess Imatinib-induced differential expression in K-562 cells.

PIM1 (proviral integration site for Moloney murine leukemia virus 1) is a serine/threonine kinase which has been linked to survival, proliferation and cell growth in cancer cells (Luszczak et al., 2020). Since the BCR-ABL fusion protein in K-562 cells activates STAT pathway signaling (Hazlehurst et al., 2009), which in turn causes expression of PIM1, inhibition of the BCR-ABL fusion protein via Imatinib treatment necessarily reduces PIM1 expression. EGR1 (Early growth response protein 1) is a transcription factor which drives the expression of a number of genes involved with proliferation (Li et al., 2019). EGR1 expression is regulated by Erk activity (Gregg and Fraizer, 2011), which is in turn activated by the BCR-ABL fusion protein (Hazlehurst et al., 2009). It is logical therefore that inhibition of BCR-ABL activity leads to downregulation of EGR1, as predicted by the literature search. SLC25A37 (Mitoferrin-1) is a protein involved with transport of iron into the mitochondria (Lytovchenko and Kunji, 2017). It's expression is regulated by GATA-1 in zebrafish (Amigo et al., 2011) and therefore probably in humans too. GATA-1 is in turn upregulated in K-562 cells following Imatinib treatment (Xu et al., 2014), which would explain the upregulation of SLC25A37 predicted by the literature analysis. SPTA1 (Spectrin alpha 1) is a scaffold protein which crosslinks actin. The mechanism for SPTA1 upregulation following Imatinib treatment is less clear, due to the lack of knowledge about SPTA1 regulation, however it has been shown to bind ABL (Ziemnicka-Kotula et al., 1998), so there is a clear link between SPTA1 and ABL.

To test for Imatinib-specific gene expression changes in K-562 cells, I produced plugs containing: barcode 1, K-562 cells and DMSO; or barcode 2, K-562 and Imatinib. I incubated these plugs overnight, then used the droplet-injection device to inject a reagent mixture containing perm/wash buffer and reagents for reverse transcription. I then incubated these plugs for 90 minutes at 42°C, pooled the plugs and purified the single-stranded cDNA using AMPURE XP-beads. The cDNA product was then quantified with a series of qPCR reactions, together with different combinations of primers. The results showed that for the genes tested, gene expression changes were significant and direction of differential regulation matched that predicted by literature (Figure 2.16).

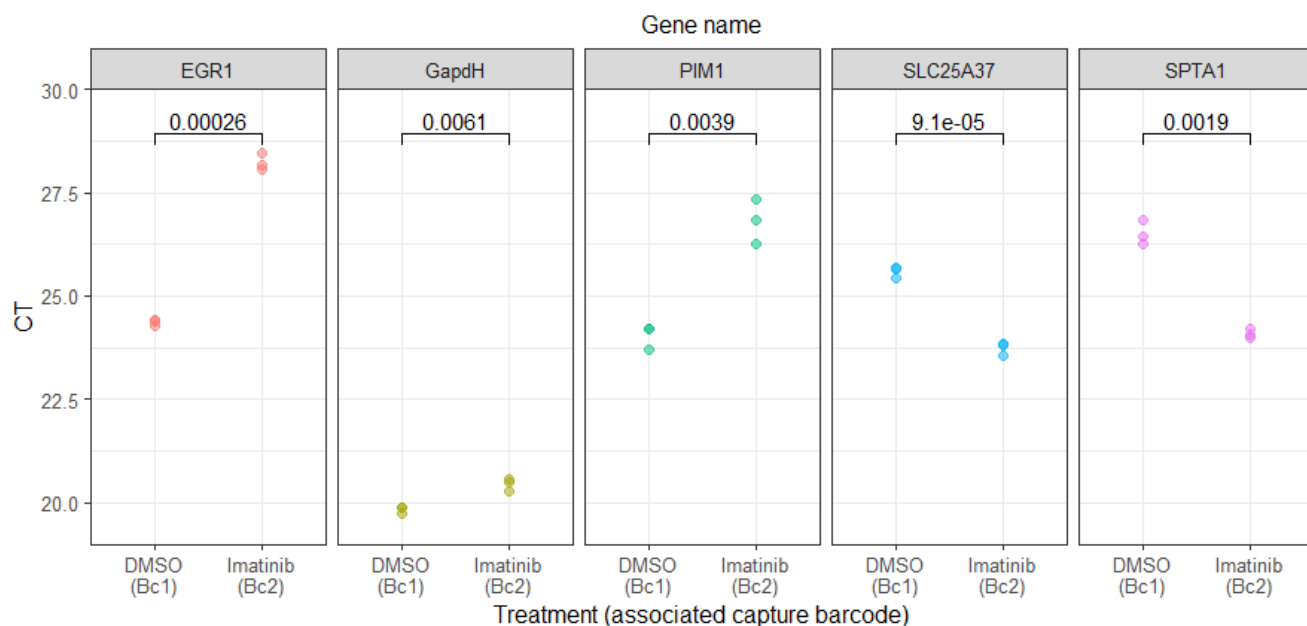


Figure 2.16 K-562 cells were treated in plugs with Imatinib or DMSO, in the presence of a treatment-specific barcode. After cell lysis and reverse transcription in plugs, the cDNA was pooled and purified, then quantified with qPCR. Direction of gene expression change was consistent with literature values. p-values were computed using two-tailed t-tests. Although all genes showed differences in expression between the two conditions, these differences were greater and more significant for all genes other than GAPDH.

Gene expression was normalized based on GAPDH, given that this was known to not be differentially expressed as a result of Imatinib treatment. The normalized results gave differential expression in the direction and magnitude predicted by the literature study (Table 2). Apart from for PIM1, the magnitude of expression change fell within that predicted by the two microarray studies. For example, EGR1 was downregulated 0.068x in GSE19567 and 0.21x in GSE10283. In the qPCR experiment, it was found to be downregulated 0.11x which is very close to both values. Overall, this shows that the basic principle of transcriptomic readouts for drug-treatment of cells in plugs is possible, and that DNA barcodes mixed with each drug can be used to barcode cDNA, thus encoding drug treatment. Furthermore, because the magnitude of detected differential expression fitted with that detected in bulk RNA-seq in previous studies (Håkansson et al., 2008; Neumann et al., 2007), it could be concluded that this lysis and reverse transcription approach has good efficiency.

Study	Gene-specific fold change in expression			
	EGR1	PIM1	SLC25A37	SPTA1
GSE19567	0.067764	0.161596	6.564899	11.88414
GSE10283	0.209932	0.129333	2.889227	3.645177
Plug-qPCR	0.105993	0.226231	5.538663	4.86132

Table 2. Fold changes for each gene of interest, after normalization of the plug results towards GAPDH expression.

Preliminary drug screening on K-562 cells

Having shown that cells could be treated, lysed and the mRNA reverse transcribed in plugs, and that this allowed meaningful treatment-specific changes in gene expression to be measured, I was able to proceed to combinatorial drug screens with whole-transcriptome RNA-seq. First, I designed an experiment to understand within-experiment variation, based on the fact that Dr. Mathur's experiments had shown synergy for the combination between Imatinib and YM155 in K-562 cells. Imatinib as previously mentioned, targets the BCR-ABL fusion protein which is a key feature of K-562 cells. YM155 is a potent inhibitor of survivin promoter activity. Based on the GR35 concentrations used by Dr. Mathur, I used YM155 at 0.0004 μ M and Imatinib at 0.039 μ M. I tested these two drugs in plugs on K-562 cells, both as monotherapies and in combination, with multiple replicates each (Table 3). Four replicate dilutions were produced for each drug and also for the DMSO-control, and unique barcode fragments were added to each replicate of a condition (12 unique barcode fragment sequences total, giving 36 possible unique barcode combinations). Plugs containing K-562 cells were then produced using the BD valving platform, containing each possible pairwise combination from the drugs and DMSO control replicates. There were 10 plugs for each combination, with 5 media-only plugs between each set to wash away any remaining drug from the previous set, thus preventing cross-contamination. The whole process was run twice to produce two replicates, henceforth referred to as cycles.

		Numbered barcode fragments with SMART-seq primer						
		Ym155 (1)	Imatinib (2)	DMSO (3)	Ym155 (4)	Imatinib (5)	DMSO (6)	Unique treatments
Lettered barcode fragments with poly-dT sequence	Ym155 (A)	1A	2A	3A	4A	5A	6A	Ym155 + YM155 (4x)
	Imatinib (B)	1B	2B	3B	4B	5B	6B	Imatinib + Imatinib (4x)
	DMSO (C)	1C	2C	3C	4C	5C	6C	DMSO + DMSO (4x)
	Ym155 (D)	1D	2D	3D	4D	5D	6D	Ym155 + Imatinib (8x)
	Imatinib (E)	1E	2E	3E	4E	5E	6E	YM155 + DMSO (8x)
	DMSO (F)	1F	2F	3F	4F	5F	6F	Imatinib + DMSO (8x)

Table 2. Replicates in the Imatinib-Ym155 drug screen. Each of the 12 syringes are shown on the column and row titles, while the resultant barcode combinations are shown in the table, colored according to the unique treatment combination produced.

After 16 hours of incubation, the plugs were removed from the incubator and reagents were added to each plug using the droplet-injection device. These reagents allowed lysis of cells, ligation of barcode fragments and reverse transcription of mRNA. The plugs were incubated for 90 minutes at 42°C, before they were eluted from the collection tubing. cDNA was then extracted from this aqueous pool using AMPURE XP beads and amplified by PCR. The amplified cDNA was then purified again and fragment size was analyzed by high sensitivity gel electrophoresis using a 2100 Bioanalyzer instrument (Figure 2.17). This showed that the main fragment size peak in the cDNA library was between 1.5-2 kbp, as would be expected, given the overlap in fundamental principles between my microfluidics-based workflow and the SMART-Seq2 workflow (Picelli et al., 2014). Libraries produced from the microfluidic workflow had fewer short DNA fragments, but have a less smooth distribution of sequence lengths.

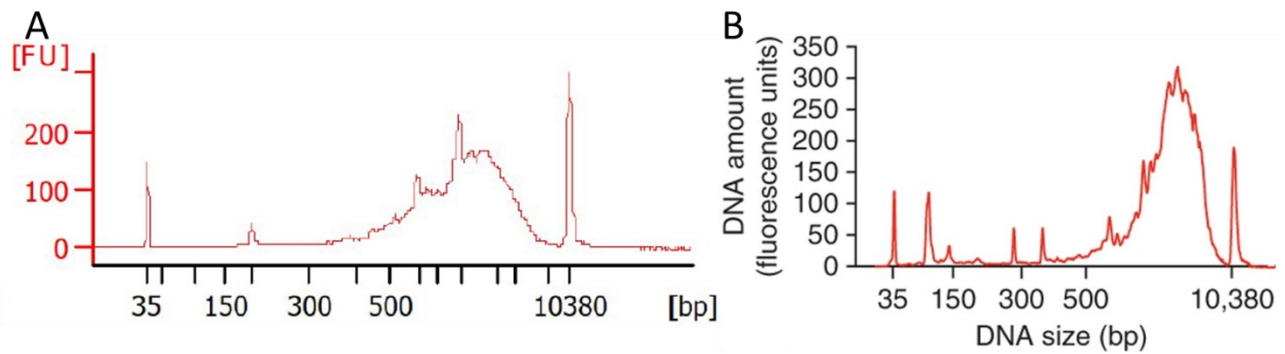


Figure 2.17 Bioanalyser traces of cDNA libraries prior to tagmentation. A) Library produced by plug-based lysis of cells, ligation of barcode fragments and reverse transcription, then purification of single stranded cDNA, amplification with the SMART-seq primer and a further round of purification. B) From Picelli et al., 2014. Library produced by lysis of single cells and reverse transcription in plates, according to the SMART-seq2 workflow. In both libraries the main peak of cDNA was between 1.5-2 kbp, with minimal sequences shorter than 500 bp.

After confirmation that reverse transcription and amplification had been successful, tagmentation and indexing were performed according to cycle by Jelena Pistolc from the Genomics Core Facility at EMBL, Heidelberg, using an in-house 3' tagmentation protocol (Hennig et al., 2018). Paired-end sequencing was then carried out with a MiSeq sequencer and demultiplexing of the DNA-barcodes and alignment of the reads was performed by Dr. Jonathan Landry (see details in methods for more information). This resulted in a median of 195,957 reads/ replicate of a condition (prior to filtering steps), from a theoretical 222,222 reads per replicate of a condition. For comparison to the yield from Dr. Mathur's workflow, similar filtering steps to those used by Dr. Mathur were performed, and the number of retained reads dropped to 72,729 (32.7% of the theoretical maximum). This compares favorably with that obtained by Dr. Mathur, where 16.4% of the maximum possible reads were retained after filtering. Moving forwards, data was analysed by Olga Ivanova with an alternative data processing pipeline. Genes with 150 or fewer total counts per gene were removed, as were two samples with particularly low counts. Then a variance stabilizing transformation (vst) (Anders and Huber, 2010) was performed to remove heteroscedasticity and normalize the counts to library size (Supplementary Supplementary Figure 5.1A). This prefiltering pipeline resulted in a median of 63,820 reads per sample.

A principal component analysis (PCA) was performed to understand whether the main variation between samples correlated to treatment and cycle number (Figure 2.18). This showed that samples with Imatinib treatment clustered separately to those with DMSO control (FS) or YM155. The clearest

separation was between each of the 2x concentration treatments of YM155 and Imatinib (pink and turquoise). The samples which were partially split between the Imatinib and YM155 clusters were samples from the combination treatment (blue), and some Imatinib monotherapy treatments (gold). While it makes sense that the combination treatment samples would cluster somewhere between the two monotherapies, it is not clear why some Imatinib monotherapy samples would cluster towards the YM155 samples. It is also not clear why the negative control samples containing only DMSO in Freestyle medium (red) cluster together with YM155 samples. This may indicate that the YM155 effect was overall very weak, and therefore not that different to DMSO-only treatment. This could be the case if Ym155 was partially degraded prior to plug production. In future, a plate-based viability screen should be carried out for each new drug stock prior to plug-based screens. Cycle number (replicate) does not appear to drive variation in either of the first two principal components. It is worth noting that only 7.4% of the variance in the data was explained by the first principal component (Supplementary Figure 5.1B). Further variation is fairly evenly distributed across the remaining principal components, with the next 10 principal components showing 3.5-2% of further variance and the vast majority after that showing roughly 1% each. Together, this indicates that the signal was very weak, which could be partially explained by insufficient sequencing depth, which resulted in large numbers of genes with 0 counts for a large number of samples.

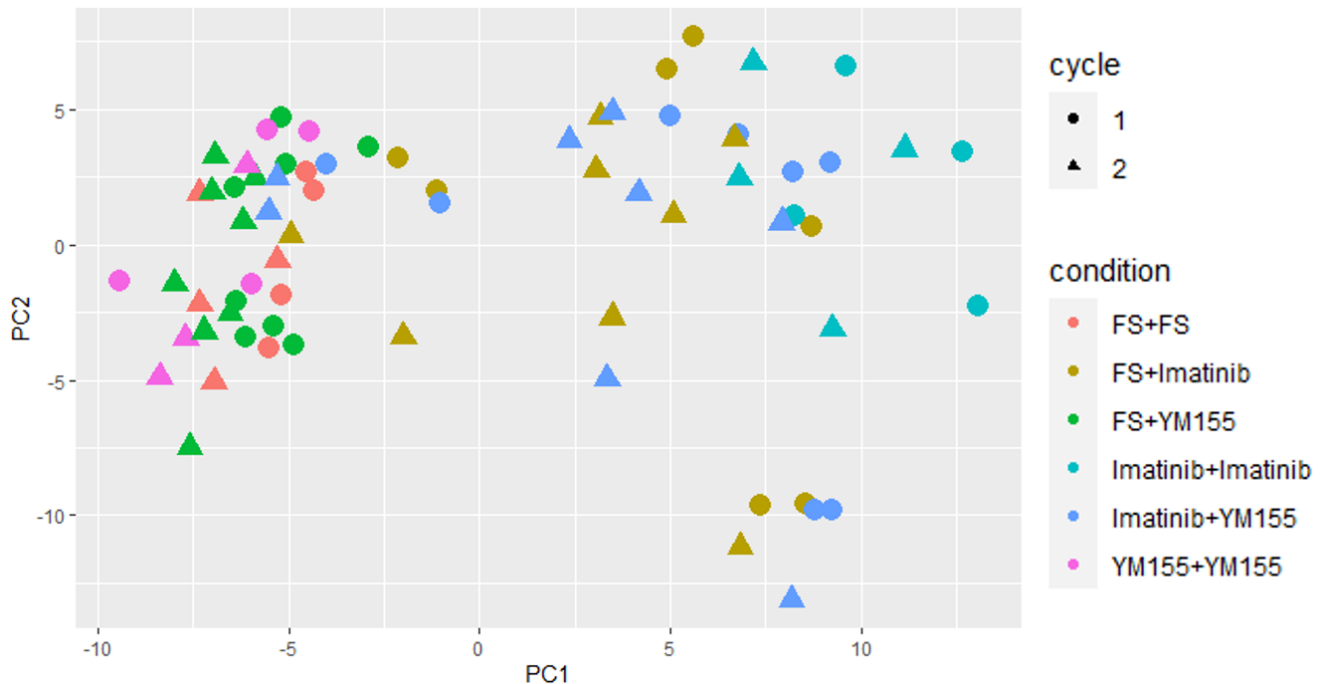


Figure 2.18 Plot by Olga Ivanova, data my own. Principle component analysis (PCA) of gene expression data, colored by drug treatment and with shape set by cycle number (replicate). In order to understand the within-cycle variation for drug-perturbations with transcriptomic readout using my workflow, K-562 cells were treated in plugs with different combinations of Imatininb, YM155 or a DMSO control. 4 replicates of each treatment were used to produce plugs, each accompanied by a unique DNA barcode fragment. After incubation with drugs, cells were lysed, barcode fragments were ligated together and mRNA was reverse transcribed in plugs. cDNA was then extracted from plugs, amplified, tagmented and sequenced. Prior to plotting, counts had been filtered to remove genes with 150 or fewer counts per gene, 2 low quality samples were removed and a variance stabilizing transformation had been applied. Samples formed two main clusters in the PCA, generally correlated to Imatinib treatment vs. YM155 or DMSO control (FS) treatment. There was no strong separation as a result of cycle number.

To further investigate the gene expression data obtained from this workflow, differential expression analysis was performed with DESeq2 (Love et al., 2014). The 2x concentration samples for Imatinib and DMSO control were compared, and genes which passed the false-discovery rate (FDR) cutoff of 0.05 were retained. The distribution of p-values from this analysis was atypical, which may indicate that further filtering was required (Supplementary Figure 5.1C), however it was deemed more important at this stage to retain the maximum possible number of reads. Differential expression analysis gave 0.66% of genes showing upregulation, 0.59% showing downregulation and 77% of genes having counts too low to be considered for differential expression analysis (Supplementary Figure 5.1D). On comparison to the same panel of genes identified for the qPCR validation experiments (Table 3), the majority of

genes did show differential expression in the direction predicted by the literature values. A number of genes either could not be assigned an adjusted p-value, or even could not be assigned a log2FC value. The first situation occurs because automatic independent filtering identified the gene as having a baseMean count which was too low. PODXL was a sample which was filtered from the dataset prior to differential expression analysis due to low counts. Overall, these results are very encouraging but only constitute a first step in evaluation of this drug screening workflow. Further experiments will require deeper sequencing and screening of a full drug panel, to understand whether this workflow is able to produce RNA-seq data which accurately predicts drug response and could even be used for patient-specific mathematical modeling.

padj	baseMean	Ensembl Id	Gene name	Plug barcoding log2FC	GSE19567 log2FC	GSE10283 log2FC
0.0386	3.3313	ENSG00000075340	ADD2	2.6514	2.1311	1.5056
NA	1.9212	ENSG00000102804	TSC22D1	2.5126	1.7159	1.6980
0.4541	3.7919	ENSG00000103811	CTSH	-0.9244	-1.5946	-1.7661
0.0010	2.2972	ENSG00000120738	EGR1	-3.8785	-3.8833	-2.2520
NA	1.6823	ENSG00000120833	SOCS2	-1.1093	-2.5422	-2.5422
NA	NA	ENSG00000128567	PODXL	NA	2.2029	1.5444
0.0001	4.0388	ENSG00000137193	PIM1	-3.9031	-2.6295	-2.9508
0.0000	51.2846	ENSG00000147454	SLC25A37	2.7920	2.7148	1.5307
0.0019	4.9832	ENSG00000163554	SPTA1	2.1970	3.5710	1.8660

Table 3 Values determined by Olga Ivanova. Table of differential expression analysis results. Analysis was performed with DESeq2, to determine which genes were differentially expressed in RNA-seq data from K-562 cells treated in plugs and barcoded according to drug combination treatment. Imatinib and DMSO treatment conditions were compared, and genes previously identified based on literature were selected. FDR was set to 0.05.

Outlook

These results show that a workflow has been successfully established for pairwise drug treatment in plugs, with a transcriptomic readout. Each newly developed component of this workflow was first assessed independently, then as part of a simplified workflow which was evaluated with a qPCR readout. After this, an initial plug-based experiment with drug treatment and combinatorial barcoding was performed to evaluate within-experiment variation. Sequencing data from this experiment is promising, indicating that differential gene expression can be identified from RNA-seq data based on

libraries barcoded in plugs according to drug treatment condition. Due to insufficient sequencing depth, the significance of the results is limited, so future work will need to sequence at greater depth, particularly if this data would be used to build mathematical models of drug response.

3. Discussion

Unifying themes

This work is a combination of two related projects, both aimed at improving outcomes for cancer patients by working towards microfluidic workflows for determining patient specific drug combinations. The three common ideas which drive this work are as follows. Patient-specific drug combinations hold immense potential to improve patient outcomes by increasing efficacy of treatment and reducing relapse. To determine new drug combinations and help doctors decide how to treat each patient, it can be very effective to directly perturb cells from patient cancer biopsies and determine their sensitivity to each treatment, as this does not rely on biomarker information which may be missing. The Braille Display (BD) valving device offers unique opportunities to automatically combine different reagents into microfluidic plugs to screen large numbers of drug combinations, using only a small number of patient cells. This is particularly relevant to solid tumors, where only small numbers of cells are available from tumor resections or biopsies.

CTL activity screens

In the first part of this thesis, primary human CTLs were successfully purified and activated as shown by flow cytometry. This process could be consistently repeated with new blood samples and with each aliquot of immune cells. In CTL activity screens, the ratio of CTLs to target cells correlated well with extent of cell death observed, as was expected based on literature (Khandelwal et al., 2015). The bispecific antibody was found to facilitate CTL-induced target cell death, confirming that this is a powerful tool to overcome CTL specificity for in *ex vivo* experiments in which CTL activity is measured. Furthermore, two different assays were trialed and found to allow detection of CTL-induced target cell death. Unfortunately, both assays were deemed unsuitable for microfluidics based drug screens, as the signal to noise ratios over the necessary incubation times would not allow small differences between treatment conditions to be detected. Further work is therefore needed, before microfluidics-based CTL activity screens can be performed.

It was also concluded that a microfluidics-based CTL activity screen to compare the effects of combining perturbagens would be most useful for basic research applications. This is because the high complexity

of interactions between immune cells and cancer cells cannot be properly replicated *ex vivo*, such that all types of ICIs could be tested and accurate patient-specific predictions made. For instance, many immune checkpoints are only present on APCs, rather than directly on the target cells. Even PD-L1 is expressed on APCs (Wölfle et al., 2011) in addition to target cells. This means that the immune-checkpoint expression status of patient tumor APCs is also very important. As such, any approach which attempted to screen combinations of all existing ICIs must include APCs. On the other hand, there is growing evidence that cytokines play a very important role in many aspects of cancer drug treatment response (Bruch et al., 2021; Tarafdar et al., 2017; Waldmann, 2018), so testing the effects of different combinations of cytokines, target cells and immune cells would be very useful. If the choice of cytokines could be matched to different tumor environments detected with metabolomics, this could provide valuable insight into the effect of various TME conditions and TME-specific treatments could be identified.

One intriguing possibility to detect CTL response to ICI treatment is to use differences in gene expression. It could be possible that through using CTLs and target cancer cells or APCs from different donors, a SNP-based approach (Kang et al., 2018; McFarland et al., 2020) could be used to deconvolute transcriptomic response of APCs from that of co-encapsulated CTLs. By identifying SNPs present in each read, the cell type identity of the read could be determined based on the SNP profile of each cell type. This would be extremely powerful, as this would provide insight into the molecular mechanisms active in treated immune cells, however it is unclear whether such approaches would really be applicable for this purpose. Related to this however, it may be possible to identify a limited number of genes related to CTL activity which are highly variable (in terms of SNPs) between individual. Such genes could be quantified by qPCR experiments.

Transcriptomic drug response workflow

In the next section, a robust workflow was developed for injection of reagents into an incoming train of plugs. No significant variation in quantity of injected reagent was observed throughout the process of reagent addition to 180 plugs, and phase separation of plugs was retained throughout this process. A detergent was also found which allowed lysis of cells within plugs, without causing break-up or fusion

of plugs. This was in sharp contrast to the effects of the standard lysis agent, Igepal, which caused extension fusion of adjacent plugs and consequent cross-contamination when added to plugs. The amount of cDNA produced by reverse transcription of mRNA from cells lysed with Igepal was equivalent to that produced by cell lysis with the chosen detergent: Perm/wash buffer. Importantly, both of these developments could be very useful for other microfluidic workflows in plugs, opening the way for multi-step experimental workflows in plugs. This would allow workflows to be performed which closer resemble the complex reaction steps which can be performed in microtitre plates, while retaining all the benefits of screening in microfluidic plugs. It is important to note however, that length of tubing required to hold plugs doubled during droplet-injection, so multiple sequential reagent addition steps are unlikely to be feasible with the current format of the droplet-injection workflow.

Having successfully established a means of lysing cells in plugs and adding reagents to pre-incubated plugs, I wanted to test these steps together in a simplified workflow which was not dependent on ligation of barcode fragments and incorporation of a template switching oligo (TSO). This ensured that sequencing costs were not wasted if there was some fundamental flaw in the workflow. As such, I designed simplified barcode fragments which included a barcode-specific primer binding site, and a poly-dT sequence for capture of mRNA and reverse transcription. I produced plugs either with Imatinib and Barcode 1 or with a DMSO negative control and Barcode 2. After overnight incubation to allow treatment to induce differences in gene expression, reagents for reverse transcription and cell lysis were added to each plug using the droplet-injection device. The plugs were further incubated, then cDNA was extracted and expression level of a panel of genes was quantified by qPCR. The results correlated very well with literature values, both in terms of direction and magnitude of change in expression. This confirmed that drug-treatment was specific to the desired plugs, use of Perm/wash buffer was compatible with this workflow and that addition of reverse transcription reagents was consistent enough for accurate quantitative analysis of differential expression of target genes.

This qPCR approach could be further expanded. So far only two barcodes were used, but in theory many more poly-dT barcodes could be designed, such that more treatment conditions could be tested. A much larger panel of genes could also be used, but it is important to note that this approach is significantly limited because it relies on finding a suitable primer binding site which is within ~150 bp of

the 3' tail of the target mRNA. There were a number of genes which would have been interesting to test for this study, but which did not have appropriate binding sites within the required region. Given a small panel of target genes, this problem could be overcome by designing normal qPCR primer pairs for each gene, then producing barcode sequences with the first primer in place of a poly-dT sequence. For each treatment condition, a pool of barcodes would be used, each with the same barcode sequence but followed by different gene-specific first primer sequences. After reverse transcription, the barcode primer and the second of the gene-specific primers would be used for amplification. This may allow even more accurate quantification of target genes, as mRNA would only be reverse transcribed if they were bound by the first primer sequence, and they would only be amplified if the cDNA was bound by the second primer too.

A preliminary sequencing experiment was carried out on K-562 cells to understand the within-cycle variance from the plug-based transcriptomic drug screening workflow. This showed weak clustering of samples into two groups, one based on Imatinib treatment, the other a mixture of DMSO control and YM155 treatment. It was hypothesized that lack of separation between Ym155 and DMSO treated samples was a result of degradation of the YM155 prior to plug production. The weak signal was likely due to insufficient sequencing depth (63819.5 median counts/ sample). Despite these issues, differential gene expression analysis using DESeq2 (Love et al., 2014) identified a number of genes as differentially expressed, which had previously been predicted for Imatinib treatment in K-562 cells based on a literature search. This confirmed that use of the combinatorial DNA barcoding approach in microfluidic plugs allowed detection of meaningful gene expression changes in target cells.

Performing perturbations in microfluidic plugs not only allows a small number of cells to be screened on a large number of combinations. It would also significantly reduce cost in comparison to an equivalent screen in microtitre plates, where a minimum of twice as much of the reverse transcription, ligation and cell lysis mixture would be required in comparison to plugs. This would be for a workflow in which cells were pipetted into 384-well plates together with pairwise combinations of drugs, each accompanied by a DNA barcode fragment. If each well contained only 20 μ L, which is the absolute minimum volume for most 384-well plates, 10 μ L of a 3x reaction mixture could be added to each well after incubation. If a larger number of drug combinations was used, as could be relatively easily

achieved in plugs by integration of an autosampler into the plug production workflow (Eduati et al., 2018), the difference between plugs and plates would be even greater. For example with 144 conditions per cycle rather than 42 (as could be achieved by combining drugs from 12 valves of the BD valving device, with drugs from autosampler-based aspiration from 12 wells of a microtitre plate), almost 6x as much volume would be needed to for the microtitre plates in comparison to plugs.

In comparison to Dr. Mathur's workflow in surfactant stabilized droplets, this plug-based approach is much quicker and simpler, requiring 2 full days to perform drug treatment and reverse transcription, vs. 3 full days for the surfactant-stabilized droplet approach. The droplet-based approach enabled a very impressive 420 combinations to be screened, which was exactly 10x as many as this plug-based approach would allow in its current form. However, this large number of combinations required a very complex integration of multiple different reagent input streams, which resulted in a high failure rate for experiments. In addition, by performing experiments in plugs, cells were treated in groups of around 100 cells per plug. By doing this, some of the cell-cell signaling which would normally be experienced in vivo is maintained, which should improve accuracy of drug response. Finally, using plugs rather than surfactant-stabilized droplets meant that micelle-mediated exchange of hydrophobic drugs between compartments did not occur. This meant that all targeted therapies could be screened using this setup, rather than only those with low hydrophobicity ($\log P < 0$). This is very important because most FDA-approved drugs have a $\log P$ between 1-5 (Shultz, 2019).

For future development of this work, it would be highly beneficial to incorporate the fluorescence-based caspase-readout into the workflow. This would add three new types of data: a parallel readout of drug sensitivity (caspase activity), the length of each plug and the relative cell number in each plug. Theoretically, adding the caspase readout into this workflow should not be very complex as it is already adapted for application in plugs. The necessary reagents would just need to be added during plug production and the time required per experiment would be increased, as the plug fluorescence would need to be measured prior to droplet-injection. This would probably require plugs to be passed from one collection tubing to another, as they are flowed through the tubing mounted on the microfluidic workstation. Parallel information about caspase activity of treated cells would provide a mechanism for assessing the confidence of drug sensitivity predictions, by confirming or contradicting the results from

the RNA-seq data. Knowledge about plug length would also improve analysis by providing a quality control measurement to aid in detection and removal of replicates with extreme values. The relative cell number counting approach is a recent development to the caspase-assay plug-based drug screening workflow (Utharala et al., 2021). This was introduced to allow normalization of caspase signal to cell number, to prevent variability in cell number from biasing results in the caspase-assay screen. It relies on staining of target cells with a horseradish peroxidase (HRP)-conjugated antibody prior to plug production. By encapsulating stained cells together with Amplex Red and hydrogen peroxide (H_2O_2) into plugs, the non-fluorescent Amplex Red can be converted to orange fluorescent Resorufin within the plugs. Because the number of HRP enzymes correlates with cell number, the orange fluorescence signal is proportional to cell number. This approach relies on the staining antibody having a target antigen which is present on all of the target cells, and assumes that neither the binding of the antibody, nor the exposure to H_2O_2 affects drug sensitivity. Both of these assumptions should be thoroughly investigated with RNA-seq before this approach is applied. Knowledge about cell number per plug would be highly beneficial for later analysis of transcriptomic data, as this would allow the exclusion of replicates which had extremely high or low cell numbers.

Normalization to relative cell number is necessary because of the high variability in cell number per plug observed within each caspase assay screen. In all plug-based fluorescence assays, the cell number per plug increased overall during the course of the experiment, as did the variability between plugs. In Figure 3.1, it can be seen that some plugs at the start of the experiment have less than 3x the number of cells as plugs in the last quarter of the experiment. Particularly in the second half of this experiment, the variation is very extreme, with some plugs receiving up to 7x as many cells as other nearby plugs. Given that this variation increases, it is reasonable to assume that increasing numbers of cell clusters are forming within the cell syringe over the course of the experiment, driving the variability in cell number per plug. These clusters are always observed within plugs, but it is unknown whether they are held together via cell-cell proteins in a physiological way, or whether they are the result of cells dying and releasing DNA, which is charged and therefore sticks to cells, causing clumping. In order to investigate this further, a simple experiment could be performed in which plugs containing cells were produced over a few hours, and the plugs were collected at intervals over this time. Plugs from each time point could be pooled and the cells stained with a viability dye and analyzed with microscopy to

understand what percentage of cells in clusters are viable and whether the number of clusters increases over time.

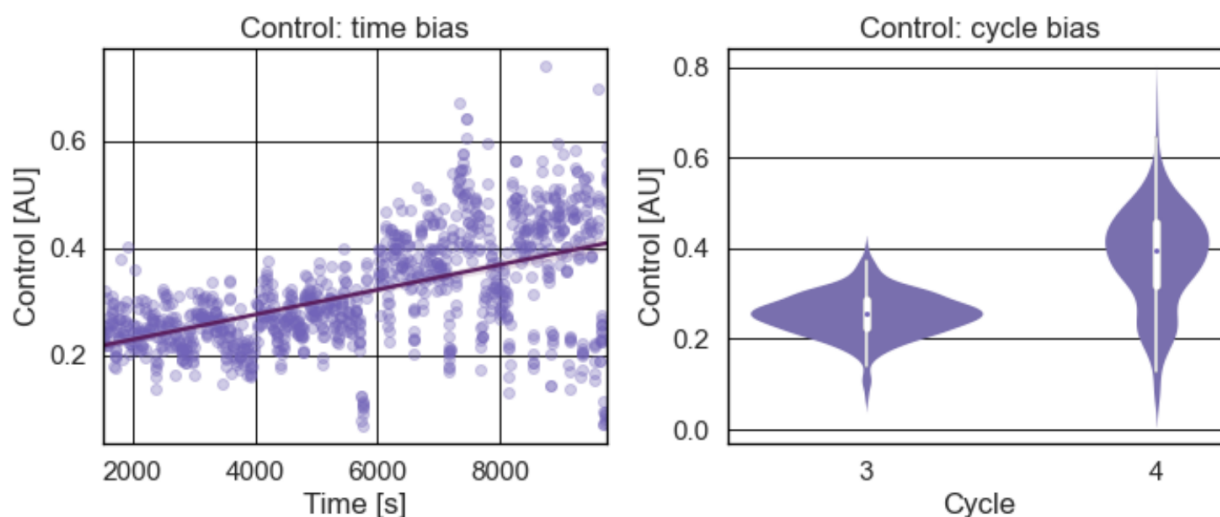


Figure 3.1 Figure produced by Vida Vafaizadeh and Denes Turei, using the Plugy analysis package (Utharala et al., 2021). Data produced by Vida Vafaizadeh. Representative plots showing how relative cell number per plug varies within fluorescence-based screens. “Control” is the orange readout which is determined by cell number. A) Variation of relative cell number per plug over the entire course of the experiment (2 cycles). B) Cycle-dependent variation in terms of relative cell number per plug.

If cell clusters were found to be composed of viable cells, these could be further investigated and perhaps better exploited as a means of ensuring more physiological conditions for cells treated in plugs. It is clear that adherent cells may respond differently to drug treatments when they are in droplets, compared to when they are tested in standard microwell plate experiments. The difference in drug response for adherent cells in droplets results from the lack of interaction between target cells and other cells, or between target cells and extracellular matrix (ECM) (Henke et al., 2020). There have been numerous studies which have shown that drug response for non-suspension cells to a number of drugs depends on the physical interactions experienced by target cells. For instance in one study, sensitivities of two breast cancer cell lines (MCF-7 and MDA-MB-231) to doxorubicin were tested in monolayers and in 3D culture (Lovitt et al., 2018). Sensitivities were found to be significantly increased in monolayers due to lack of integrin signaling through the ECM. In another study, transgenic mice with *Her2+/*PIK3CA^{H1047R}* tumors were treated with Her2 and PI3K inhibitors until resistance developed. The tumors were analyzed by RNA-seq and resistance was traced back to upregulation of ECM and cell adhesion genes (e.g. Collagen II and integrin β 1/Src). When treated in monolayers in the absence of collagen,*

these cells no longer exhibited resistance, proving that simple *in vitro* conditions failed to replicate the true physiological response of these cells. One very early study even attempted to compare directly the effects of drug treatment in suspension vs. adherent conditions for solid tumor samples (Dorfman et al., 1980). They found that cells in suspension were less susceptible to cytotoxic compounds, independent of how long the cells were incubated following dissociation, so they concluded that the difference did not lie in the regeneration of cell-surface molecules which had been cleaved during dissociation.

These issues clearly apply to both droplet-based screens and screens in which monolayers of cells are treated in microtitre plates, but it is reasonable to believe that the issues will be more pronounced in microfluidic droplets or plugs. This is because in droplets, the target cells remain in suspension throughout the entire experiment, thus there is no opportunity for any adhesion of the cells to a solid surface. In most microtitre-based drug perturbation screens, the cells are plated 24 hours before treatment begins (Subramanian et al., 2017), thus allowing some amount of ECM deposition and formation of cell-cell contacts. Of course, the benefits of this pre-incubation needs to be weighed against the issue of clonal selection via *in vitro* cultivation of patient cells. Having said this, it is reasonable to assume that cells which do not survive an initial 24-hour adjustment period are unlikely to survive the 16-hour drug treatment period in droplets, regardless of drug treatment, so they would likely just contribute to background noise anyway. Thus for applying this platform to the study of adherent cells, it will be essential to better understand how treating adherent cells while they are in suspension affects their drug response. Approaches such as inclusion of matrigel into plugs could be help to create a more physiological environment for treated cells.

The purification procedure for the cDNA could also be further improved, by making use of biotin-based purification. I used purely AMPURE XP-bead based purification, due to concerns about the cost and stability of biotinylated barcode fragments. Having tested this workflow, it is now clear that the cost of Ampure XP beads which were used in my workflow is also high, and there may be some loss of yield due to the inefficiency of single-stranded cDNA binding to AMPURE XP-beads. It would therefore be more cost effective, to use biotin-tagged barcode fragments and replace the stocks of these at least every year. I also observed an unknown contaminant in my post-PCR samples for some experiments,

which persisted despite multiple AMPURE XP-bead based purification steps. Although this did not clearly affect sequencing, it manifested in delayed migration of PCR products through the bioanalyser gel. This led to difficulties with quality assessments of the pre-tagmentation libraries. Given that this contaminant seemed to move within the gel, it is likely to be negatively charged. As such, it would be highly desirable to perform purification which did not rely on charge.

Further development of this workflow could result in a system which could provide valuable high-content data from drug screens on patient cancer cells, such that patient-specific logic models could be built. This has the potential to vastly improve patient response, by allowing non-tested treatments to be accurately predicted, thus massively increasing the number of treatment conditions which could be considered.

4. Methods

Experiments with primary human cytotoxic T-lymphocytes (CTLs)

Source of primary human CTLs

Blood samples were provided with donor consent by Dr. med. Patrick Wuchter from the DRK-Blutspendedienst Baden-Württemberg – Hessen gGmbH. Experiments with primary human CTLs were approved by the Bioethics Internal Advisory Committee (BIAC) at EMBL.

Isolation of buffy coats from whole blood

Whole blood was gently layered onto Histopaque-1077 (Sigma-Aldrich, USA) in 15mL falcon tubes (6mL of each). The tubes were centrifuged for 30 minutes at room temperature, at 400 x g with acceleration and deceleration at the minimum speed. Blood plasma (a clear yellow liquid) was carefully removed from the top of each falcon tube, exposing the layer of mononuclear cells (T cells, B cells, NK cells and monocytes) resting on the Histopaque surface (the buffy coat). 2 buffy coats were pooled into 15 mL falcon tubes, then washed twice with 12mL PBS, by centrifuging for 10 minutes at 250 x g, then removing the supernatant each time. The washed cells were all pooled and resuspended in 5mL of pre-warmed, heat-inactivated FBS. Cells were counted with a haemocytometer, then diluted to 250,000,000 cells/mL, in an FBS/DMSO mixture such that DMSO was 20% (v/v) in the final mixture. Cells were pipetted into cryovials and put into the -80 freezer in an isopropanol freezer box. After overnight freezing, the cells were transferred to liquid nitrogen.

Isolation and activation of CD8+ T-lymphocytes

Non-treated, 24-well plates were coated with 250 µL anti-mouse IgG2a (clone RM162a-1 MW1483, AntibodyChain, Netherlands) diluted 1:500 in PBS. Plates were sealed and left overnight at 4°C. The next morning, the anti-mouse IgG2a was removed and wells were washed with PBS. 250 µL per well of anti-CD3 (clone Hit3a, Cat. No. 300331, BioLegend, USA) diluted 1:1000 in PBS was then added and the plate was incubated for 5 hours at 37°C. Between 2-3 hours after the start of incubation, buffy coat cells were defrosted by repeated pipetting and removal of 10 mL warm IMDM media into the cryovial. The cells now suspended in IMDM were centrifuged at 300 x g for 8 minutes, and the supernatant

removed. CD8+ cells were then isolated with a CD8+ human T Cell isolation kit (Cat. No. 130 096 495, Miltenyi Biotech, Germany) by following the standard procedure. Briefly, cells were filtered then mixed with a cocktail of biotinylated antibodies which bound antigens of all non-CD8+ peripheral blood mononuclear cells (PBMCs): CD4+ lymphocytes, B cells, monocytes, etc. Then magnetic micro-beads bound to an anti-biotin antibody were added. The pool of cells were then passed through a column held within a magnetic stand, such that all magnetically labelled (non-CD8+) cells were captured on the column and removed. The CD8+ cells passed through the column and could be collected for activation. Cells were counted, centrifuged and diluted to $0.5-1 \times 10^6$ cells/ mL in IMDM media with 10% heat-inactivated FBS, 1% pen/strep. Anti-CD28 (clone CD28.2, Cat. No. 302914, BioLegend, USA) was added to the cell mix ($1 \mu\text{L}/\text{mL}$). Plates treated with anti-mouse IgG2a and anti-CD3 were washed with PBS. Isolated CD8+ cells were seeded into wells of the 24-well plate, then incubated for two days at 37°C , 5% CO_2 . Cells were gently aspirated and centrifuged at $300 \times g$ for 8 minutes. Cells were resuspended in prewarmed IMDM media with 10% FBS and 1% pen/strep. Cells were brought to $0.5-1 \times 10^6$ cells per mL, and IL-2 was added at $100 \text{ IU}/\text{mL}$ (Cat. No. 200-02, PEPROTECH, USA). Cells were seeded into 24-well tissue culture treated plates or a T25 flask, depending on the number of cells. If a T25 flask was used, this was kept upright in the incubator. After a minimum of 3 days, the cells were ready for use. Alternatively, media could be exchanged (including adding fresh IL-2) and cells could be used for up to 7 days, with a media change every 3 days. The typically expanded 2-5x depending on the cell stock.

Flow cytometry analysis of activated CTLs

A minimum of 5×10^5 activated cells/ condition were treated with phorbol 12-myristate 13-acetate (PMA) (Sigma-Aldrich, USA) and the calcium ionophore ionomycin (Sigma-Aldrich, USA) or kept untreated as a control. The following 5 conditions were produced for each flow cytometry experiment: treated not stained; treated and live/dead stained; treated, live/dead and CD8 stained; treated, live/dead, CD8 and IFN- γ stained; not-treated, live/dead, CD8 and IFN- γ stained. All cells were centrifuged at $300 \times g$ for 5 minutes then resuspended in IMDM media containing $1 \mu\text{L}/\text{mL}$ of brefeldin A (Cat. No. 562988, Thermo Fisher Scientific Inc., USA) and plated into 96-well plates. PMA and ionomycin were added to all wells (at $50 \text{ ng}/\text{mL}$ and $1 \mu\text{g}/\text{mL}$ respectively), except in the untreated

control. Cells were incubated at 37°C, 5% CO₂ for 4 hours, then centrifuged for 3 minutes at 394 x g, then supernatant removed by turning the 24-well plate over and tapping it onto a paper towel. Cells were resuspended in 100 µL MACS buffer and 5 µL of anti-CD8 antibody (clone HIT8a, Cat. No. 300913, BioLegend, USA) was added to the relevant wells. Cells were incubated for 5 minutes at room temperature in the dark. 2 mL PBS was added to each well, then cells were centrifuged at 394 x g for 5 minutes at 4°C and supernatant gently removed. 100 µL PBS was added to each well, with live/dead stain (Cat. No. L10120, Thermo Fisher Scientific Inc., USA) at 1:1000 for the relevant wells. Cells were incubated for 20 minutes at room temperature in the dark. Cells were centrifuged at 394 x g for 5 minutes at 4°C and supernatant gently removed. Cells were resuspended in 1 mL MACS buffer/ well, centrifuged at 394 x g for 5 minutes at 4°C and supernatant gently removed. Cells were resuspended in 100 µL cytofix/ well and incubated overnight at 4°C. Perm/wash buffer was diluted to 1x in distilled water, then filtered through a 22 µm PVDF filter (Cat. No. SLGV033RS, Millex[®] Merck KGaA., Germany). Cells were suspended in 1 mL of diluted Perm/wash buffer, centrifuged at 394 x g for 5 minutes at 4°C and supernatant gently removed. This step was repeated, then cells were resuspended in 100 µL of diluted Perm/wash buffer. 5 µL of anti-IFN-γ antibody (clone B27, Cat. No. 562988, Becton Dickinson and company, USA) was added to the relevant wells and incubated for 20 minutes at 4°C. 1 mL of diluted Perm/wash buffer was added to each well, then cells were centrifuged at 394 x g for 5 minutes at 4°C and supernatant gently removed. Cells were then resuspended in 200 µL of MACS buffer and filtered through a narrow mesh to remove cell clumps. Stained cells were analysed on the BD LSRFortessa[™].

CTL activity assays

Calcein-AM green

MCF7 cells were stained with CellTrace[™] Calcein-AM green (Cat. No. C34852, Thermo Fisher Scientific Inc., USA) according to the manufacturer's protocol, washed, then resuspended in FreeStyle 293 medium (Cat. No. 12338-018, Gibco, USA) at 200,000 cells/mL. 100 µL of stained MCF7 cells were aliquotted into each well, then mixed with different combinations of pre-activated CTLs (at ratios between 2-40 CTLs per MCF7 cell, specified for each experiment) and 1 µg/ mL bispecific antibody (AMG110, in development by Amgen, USA). Mixtures were incubated together, then plates were

centrifuged at 300 x g for 5 minutes, and the supernatant was removed and measured at 495 nm for excitation and 515 nm for emission using a TECAN Infinite M1000 Pro plate reader (Tecan, Switzerland).

Caspase activity assay

MCF7 cells, CTLs and bispecific were used at the same concentration as for the Calcein-AM green assay, but MCF7 cells were not stained in advance. In addition to cells and bispecific antibody, 15 μ M caspase-3 substrate ((Z-DEVD)²-R110, Cat. No. 13430, AAT Bioquest, USA), 4 mM DTT and 1x buffer (from 5x mix: 50mM PIPES, 10mM EDTA, 0.5% CHAPS, pH7.4). Fluorescence was directly measured in the plates at 500 nm for excitation and 522 nm for emission using a TECAN Infinite M1000 Pro plate reader.

Fabrication of microfluidic chips

Photo-masks for production of molds

Photo-masks were required for patterning the channel structures onto the photoresist during mold production. Masks had been designed by previous group members using AutoCAD (Autodesk Inc., USA), then printed externally (by Selba S.A. Versoix Switzerland) on plastic transparency slides at 25400 dpi. Based on whether channels were patterned by absence vs. presence of print on the transparency sheet, the photo-mask could be used for negative or positive photolithography respectively.

Soft-lithography for mold fabrication

A silicon wafer (Siltronix, Silicon Materials, Germany) was heated to 150 °C on a hotplate to remove solvent contamination, then left to cool for 5 minutes. SU8 2150 or AZ 40XT photoresist for droplet-injection or valving molds respectively (both MicroChem Corp., Newton MA), was poured onto the wafer and then evenly spread on the wafer using a spin coater (WS-400BZ-6NPP/LITE, Laurell Technologies Corporation, USA). For droplet-injection molds spinning was at 1000 rpm for 8 seconds, while for valving molds was at 1400 rpm for 40 seconds. The wafer was pre-baked on a hotplate by

increasing the temperature from 35 °C to 95 °C (for droplet-injection molds) or 105 °C (for valving molds), with 30 s hold time for every 10 °C temperature increase. This was then held for 5 minutes at 95 °C (droplet-injection mold) or 2 minutes at 105 °C (valving mold). A 25,400 dpi photomask with the desired design (printed by Selba S.A. Versiox Switzerland) was applied to the photoresist (taking care that any structures did not overlap with bubbles) and exposed for 100 s at 350 W (Karl Suss MA45). The wafer was then post-baked on a hotplate by increasing the temperature from 65 °C to 95 °C, with a 1 minutes hold every 10 °C temperature increase. 95 °C was then held for 5 minutes.

Molds were then developed by placing the wafer into a glass petri dish and gently pouring developer into the dish. For droplet-injection molds, development was with mr-Dev-600 (micro resist technology GmbH, Germany) for 20 minutes, after which the developer was spun off to stop the reaction. For valving molds, development was with AZ 826 MIF developer (micro resist technology GmbH, Germany) for 1 minute (with additional 10 second development periods if required), after which the reaction was stopped by spraying the mold with deionized water. For the valving mold, channel heights were checked with a profilometer (Faulhaber). Since the valving mold channel height was the desired height of roughly 40 µm, it was then further baked to create rounded channels, by heating it on a hotplate for 1 minute at 125 °C. For the droplet-injection device, freshly mixed PDMS was poured over the patterned silicon wafer, then baked overnight. The next day, the PDMS was removed and cut, such that the cross-section of the main channel was exposed. This was photographed under the microscope and measured using FIJI, to determine the ratio between channel width (precisely determined by the channel width of the photomask design) and the channel height (determined by a number of interacting factors, including choice and age of photoresist and spin speed). From this, the channel height could be determined. It was found to be 390µm, which was sufficiently close to the desired height of 500µm to be used.

[Epoxy mold copies to ensure reproducibility of chip production](#)

Epoxy mold replicas (Xia et al., 1997) were made for each valving-chip mold, as the molds are very fragile, and reproducibility could be better ensured if copies of a single, well-characterised mold were consistently used. To do this, PDMS (Sylgard 184 silicone elastomer kit, Dow Corning Corp, USA) was

cured for 24 hours, then cut out of the mold of interest, then cleaned using scotch tape and by blowing with nitrogen gas. This PDMS was then put into a clean, empty petri dish and into the desiccator for 30 minutes. 10 minutes before the PDMS had finished desiccating, epoxy was mixed at a 1:2 ratio of hardener to epoxy resin. For a single chip, 30g total of epoxy was mixed and poured into a standard circular petri dish. Care was taken to ensure that epoxy was thoroughly mixed, without introducing excessive bubbles (in particular, scraping the mixing fork on the side of the cup was avoided during mixing). Epoxy went cloudy at the start of mixing, then clear again when finished, this took around 2 minutes. Clean gloves were then applied and the PDMS chip was removed from the desiccator and carefully placed into the epoxy mixture, laying one edge down first and gradually lowering the rest of the chip down, to prevent bubbles from being created. The PDMS chip floated in the epoxy. Some bubbles were observed at the interface between epoxy and PDMS at this stage, but this air was later taken up by the degassed PDMS, so was not present in the hardened epoxy mold. The epoxy dish was placed on a flat, heat-resistant surface, with good airflow (as epoxy can produce significant heat during curing). Molds were allowed to harden for 2 weeks before being used.

Preparation of PDMS membranes

PDMS (Sylgard 184 silicone elastomer kit, Dow Corning Corp, USA) was mixed at a ratio of 10:1 (polymer to cross-linker), then degassed for 20 minutes. A 10 cm² sheet of overhead projector plastic was centered on the spin-coater (WS-400BZ-6NPP/LITE, Laurell Technologies Corporation, USA) and the vacuum was applied. PDMS was poured onto the center of this sheet, forming a pool around 4 cm in diameter. The sheet was then spun according to the type of membrane being produced: 19 seconds at 700 rpm for thin membranes, 10 seconds at 300 rpm for thick membranes (acceleration 408 rpm/s for both). Thin membranes were used for valving chips and thick membranes for droplet injection chips.

Fabrication of PDMS chips

PDMS (Sylgard 184 silicone elastomer kit, Dow Corning Corp, USA) was mixed at a ratio of 10:1 (polymer to cross-linker), degassed for 20 minutes and poured over the mold (epoxy or SU-8 mold in a

petri dish), then polymerized for 24 hours at 65 °C. After polymerization, the PDMS was cut out from the mold and inlets were punched using a 0.75 mm diameter biopsy punch. For droplet-injection chips, the electrode inlets were punched with a 0.5 mm biopsy punch, and the chips were cut ~2 mm away from the sheath fluid inlets, such that the main channel was horizontally open (Figure 1.1). The chips were then cleaned using pressurized air. The chip surfaces and corresponding PDMS membranes were activated by exposure to oxygen plasma (Femto, Diener electronic GmbH + Co. KG, Germany). Then the two activated surfaces were pressed together to enclose the channels with the membrane and the chip was put at 65 °C for 5 minutes. The valving chips were further plasma bonded to a glass slide behind the tubing inlets, such that tubing would not rupture the membrane when inserted. The droplet-injection chips had flat-cut collection tubing inserted into the open horizontal inlet, by dipping the tubing into NOVEC™ 7500 oil (3M Company, St. Paul MN), then inserting it into the channel. It was critical that the tubing went far enough into the channel, that plugs only left the collection tubing after the sheath oil inlets met the channel. The chip with inserted tubing was then heated to 85 °C on a hotplate, and indium low-melting point solder wire (GPS Technologies) was inserted into the electrode inlet until it melted and filled the electrode channel. Cables were inserted into each of the electrode inlets and the conductance of the electrode pair was tested. While the chip was still on the hotplate (so that the indium solder remained melted), the pairs of electrode wires were carefully bent and twisted together. The chip was then removed from the heat, and placed on an ITO-coated glass slide (CG 41IN-S207, Delta Technologies Limited, USA), with the ITO-coated surface facing downwards. Epoxy glue was mixed, then applied to the junction between the chip and the glass, at the site of entry of the collection tubing, to seal the collection tubing inlet. The glue was allowed to dry for 12 hours before use.

Reagents for drug screens

Culturing cell lines

MCF-7 cells (ATCC®HTB-22, USA) were cultured in DMEM medium supplemented with 10% FBS (both Gibco, Thermo Fisher Scientific Inc., USA). K-562 cells (ATCC®CCL-243TM, USA) were cultured in IMDM medium supplemented with 10% FBS (both Gibco, Thermo Fisher Scientific Inc., USA).

DNA barcodes

Barcodes for reverse transcription and qPCR

qPCR primer-binding barcodes were designed by sequentially combining 2 x 16 bp barcode sequences generated by bgen (bgen: barcode generator | GEAR (gear-genomics.com), which produces pools of barcode sequences with “balanced, per-position base distribution” with high dissimilarity from each other. Then primer binding sites were sought in the resultant 32 bp sequences, using Primer3Plus (Untergasser et al., 2007), and the 32 bp sequence was manually edited until a sufficiently acceptable primer was found ($T_m = 58.5-60.5^\circ\text{C}$, GC% = 40-60%, ANY and SELF binding < 4). A poly-deoxythymidine (poly-dT) sequence for capture of the poly-adenosine (poly-A) tail of mRNA transcripts was then added at the 3' end. These were used at 0.5 μM final concentration.

Combinatorial barcode fragments for encoding pairwise drug combinations

DNA barcodes for combinatorial transcriptomics were designed and tested by Dr. Mathur (Mathur et al., 2021; Utharala, 2016), except that I did not use biotinylated barcode fragments. They were ordered from Sigma at HPLC purity, dissolved in nuclease-free water (Thermo Fisher Scientific Inc., USA) and stored at -80°C . The two single-stranded complementary oligonucleotides which made up each double-stranded barcode fragment were annealed to produce barcode fragments with single strand overhang sequences. To do this, equimolar concentrations of the Fwd and Rev sequences for each barcode fragment were mixed, and diluted to 20 μM in nuclease-free water. Each mixture was heated at 95°C for 10 minutes, then removed from the heat block and allowed to return to room temperature over 1 hour. The annealed barcode fragments were stored at -20°C . These were used at 1 and 0.5 μM final concentration for numbered and lettered barcode fragments respectively.

Preparation of cells for plug-production

Cells used for the transcriptomic workflow were either K-562 or a suspension of cells from a digested HCT-116 mouse tumor. A minimum of 2×10^6 cells were required per experiment. The suspension was

first washed with PBS, then resuspended in 1 mL of FreeStyle 293 medium. Xanthan gum solution in FreeStyle 293 medium, filtered through a 22 µm PVDF filter (Cat. No. SLGV033RS, Millex® Merck KGaA., Germany) was added to a final concentration of 1 mg/mL. Cells were passed through a 40 µm cell strainer to remove cell clumps, then counted (TC20 Automated cell counter, Bio-RAD Laboratories Inc., USA). Cells were diluted to a final concentration of 1×10^6 cells/ mL, and pluronic (Sigma-Aldrich, USA) was added to a final concentration of 0.2 mg/mL. The cell suspension was pipetted into a pre-prepared 3 mL Luer-Lok syringe (Beckon-Dickinson, USA), with 30 cm tubing (AWG 24T, Adtech Polymer Engineering Ltd., UK) connected via a PDMS plug. A magnetic disc was added to the syringe to allow stirring of the cell suspension.

Preparation of drugs

Drugs were purchased from Selleckchem, suspended in sterile DMSO and stored at -80 °C. For transcriptomic screens, drugs were diluted in FreeStyle 293 medium (to 3x the GR35 concentration and 1% DMSO) and mixed with a unique qPCR barcode or annealed barcode fragment. Drugs were then aspirated into 3 mL Luer-Lok syringes (Beckon-Dickinson, USA) connected via a 27G ¾ needle (Beckon-Dickinson, USA) to ~30 cm length, size TW30 PTFE tubings (Adtech Polymer Engineering Ltd, UK). This media was chosen because it allows culturing of cells in the absence of FBS, which is essential because FBS contains large amounts of protein which would lead to adhesion of plugs to the channel walls (“wetting”) during plug production (Clausell-Tormos et al., 2010). GR35 concentrations were based on those determined by Dr. Mathur for his droplet-based drug screen: the concentration which results in 35% of the maximum growth reduction of treated cells (Hafner et al., 2016). This concentration was determined by plate-based screens followed by fitting of growth reduction curves to deduce the GR50 concentration, from which the GR35 concentration could be deduced based on the hill-slope of the curve using the following equation:

$$GR_F = \left(\frac{F}{100 - F} \right)^{\frac{1}{H}} * GR_{50}$$

Microfluidic operations

Operation of pumps and Braille Display for plug-production

All syringes were mounted onto PHD 22/2000 syringe pumps (Harvard Apparatus, USA) and primed to removed air bubbles. A magnetic stirrer (VP Scientific, USA) was aligned above the cell syringe, so that the magnet could be continuously agitated to keep the cell suspension evenly distributed. An ice pack was laid on top of the cell syringe to keep the cells cool. Drug and cell syringes were run at 500 μL /hour. Two oil syringes were used, running at 80 μL /hour and 200 μL /hour respectively. One oil syringe contained 3M™ Fluorinert™ FC-40 (IOLITEC Ionic liquids technology GmbH, Germany) with 0.5% 1H,1H12H,2H-Perfluoro-1-octanol (PFO) (Cat. No. AB125017, Abcr GmbH, Germany) at. The other oil syringe contained mineral oil (Cat. No. M8410-1L, Sigma-Aldrich, USA).

An Sc-9 Braille Display (BD) (KGS Corporation, Japan) plugged into its custom-made metal mount and custom-made controller block (Utharala et al., 2021), was connected to a computer hosting LabVIEW (National Instruments, USA). The pins of the BD were controlled by the LabView program “Samples on Demand” (Eduati et al., 2018). The default pin constellation directed all flows to waste. In order to “open” valves, such that flow was instead directed to plug-production, two pins were simultaneously actuated in opposite directions (the inner pin moved up, while the outer pin moved down). In order to run a reproducible sequence of pin actuations which determined which drug treatments were produced, this information was written into csv files and run via the “Samples on Demand” program.

For each experiment, a new valving chip was treated with aquapel (Autoserv, Germany), by gently injecting aquapel into the plug-collection outlet, until the aquapel met the T-junction. An empty syringe, connected via needle and tubing was used to remove the aquapel. Blue dye was then filled into the chip via the FC-40 inlet, so that the valves were clearly visible and the chip could be aligned over the BD pins and clamped into place (as shown in Figure 1.6). A plexiglass bar was then screwed into place over the BD and aligned chip, to hold these two together. Once all liquids were flowing, tubings were inserted into their respective inlets on the valving chip, and a 3.6 metre collection tubing (UT6, Adtech Polymer Engineering Ltd., UK), filled with nuclease-free water was inserted into the plug outlet. 10 cm lengths of TW30 PTFE tubing were inserted into each waste outlet. Pumps were run for 5-10 minutes, then each valve was tested to ensure that flow was coming. This was done by opening each valve individually and

checking that blue dye was released into the plug production channel. After all valves had been opened and reclosed, mineral oil plugs were produced for a further 30 seconds minimum, so that the collection tubing could be observed and it could be confirmed that no aqueous flow was coming once all the valves were shut, as this would indicate that one of the valves was leaking.

Plugs were produced by opening 3 valves at a time, using a csv sequence loaded into the LabView program "Samples on Demand". The csv ensured that cells, a letter-barcoded drug and a number-barcoded drug were each open for each sample plug. This resulted in a 0.66% DMSO concentration for each plug, since each drug syringe had 1% DMSO and the cell syringe had none. Each cycle contained every possible pairwise drug combination, with 8 sample plugs per combination, separated by a set of 4 wash plugs (2x media with cells). The DMSO-control combination was repeated at the beginning and the end of each cycle. The csv contained 3 cycles, each separated by 90 seconds of mineral oil plugs (produced via 30 pin actuations of a set of pins which did not control any valves, e.g. Pins 1-3). Plug length was monitored throughout, to ensure that plugs were roughly consistent sizes, which indicated that each valve was working properly. After plug production, the collection tubing was removed, sealed and kept in at 37 °C, 5% CO₂ atmosphere for 16 hours.

Fluorescence measurements from plugs

Fluorescent intensities of plugs were measured using a custom-built optical system. Plug tubing was positioned over the 40x objective lens of an inverted light microscope (Eclipse Ti-S, Nikon GmbH, Germany). Laser beams with wavelengths of 561 nm, 488 nm and 375 nm were directed at the plugs, via a series of dichroic mirrors within the optical system. Emitted light was directed through a series of bandpass filters, then measured by three photomultiplier tubes (PMTs), each with a specific detection wavelength. Data was recorded using the LabVIEW program "Multi-channel acquisition".

Operation of droplet-injection chip for introduction of reagents into plugs

Droplet-injection chips were treated with 1% 1H,1H,2H,2H-perfluorooctyltrichlorosilane (abcr GmbH & Co. KG, Germany) in NOVEC oil, by injecting this through the chip via a 23G needle inserted into the pre-glued length of collection tubing which was attached to the chip. The chip was then flushed with pure NOVEC oil, and then air. The chip was then further treated with aquapel, which was then flushed out with air, followed by pure NOVEC oil. The chip was then mounted onto a conductive microscope stage.

Three NOVEC syringes were mounted onto syringe pumps, one containing 1% Pico-Surf (Sphere Fluidics Limited, United Kingdom), the other two contained 0.1% picosurf. After priming, these were all set to 100 $\mu\text{L}/\text{hr}$.

Reagents for cell lysis, ligation of DNA barcode fragments and reverse transcription were mixed, filled into a syringe and mounted onto a syringe pump for priming (see “reagent mixtures” section). Care was taken to prevent contamination with RNases, by doing this in an RNase-free area, cleaned with RNaseZAP (Thermo Fisher Scientific Inc., USA), regularly changing gloves and using only RNase-free filter-tips. Once this syringe had finished priming, it was set to 250 $\mu\text{L}/\text{h}$.

16 hours after the drug-screening plugs had been produced, the plug tubing were removed from the incubator and brought to the microfluidic workstation. A syringe filled with nuclease-free water was mounted onto a syringe pump, primed and then connected to the plug tubing via a 23G needle. The flow rate of the pump was set to 500 $\mu\text{L}/\text{h}$.

The tubing containing the overnight-incubated plugs was connected to the length of connection tubing glued to the droplet-injection device via a PDMS adaptor cube, through which a 0.75 mm hole had been punched. All other primed syringes were then connected via tubing to their appropriate inlet ports on the droplet-injection device, and the syringe pumps were started. A new 2 metre length of collection tubing (prefilled with nuclease-free water) was inserted into the plug outlet of the droplet-injection device. This tubing was wound around a glass bottle to keep it organized, and the glass bottle was filled with ice to prevent the enzymatic reactions from occurring until all plugs had been through the device. A continuous electric field of 0.3kV was applied, via the electrodes embedded in the chip. The voltage

was set by the LabVIEW program “Analysis and Sorting” and amplified by a high voltage amplifier. Depending on the number of plugs per cycle, droplet-injection took between 25 and 40 minutes per cycle. New collection tubing was used for each cycle of plugs, such that each cycle was physically separated. After all three cycles had reagents added, the ice was poured out of the collection tubing bottles and the plugs were left at room temperature for 30 minutes. After this, the bottles were put into an incubator at 42°C for 90 minutes. Finally, each cycle of plugs was collected into a separate microcentrifuge tube by manually flushing the collection tube with nuclease-free water using a syringe connected to the collection tubing by a 23G needle. This plug mixture was incubated for 10 minutes at 85°C, then stored at -20°C until further processing steps.

Extracting cDNA from plugs

60 µL of PFO was added to each microcentrifuge tube containing pooled plugs, and the mixture was firmly shaken a few times. The aqueous layer was then carefully removed with a pipette, taking care not to extract any of the oil layers. Single stranded cDNA was then purified from the aqueous layer, by mixing it with 0.65x the volume of Ampure XP beads (Beckman Coulter, USA). Since these beads are not designed for single stranded DNA, the mixture was incubated together for 10 minutes to ensure maximum yield of cDNA. From this point, the standard protocol for Ampure XP size selection was followed. Size selection was then repeated on the eluate, this time with 1x the volume of Ampure XP beads. The 10 minute initial incubation was used for this purification as well.

qPCR

Detergent testing

To quantify release of mRNA after lysis with different detergents, 4x 20 µL reverse transcription mixtures were made up, each with different detergents: 0.3% Igepal (v/v), 0.003% Igepal (v/v), perm/wash (1x), nuclease-free water. The reaction mixtures were incubated for 30 minutes at room temperature, then 90 minutes at 42°C, then 5 minutes at 85°C. cDNA was not purified after reverse

transcription, as small differences in carry-through could change the final concentration from each lysis agent. Instead, reverse transcription products were diluted 1:800 in nuclease-free water. 1 μ L of diluted cDNA was then added to each 20 μ L qPCR mixture containing 10 μ L SYBR Green PCR Master mix (Thermo Fisher Scientific Inc., USA), 0.25 μ L of each primer at 10 μ M and 8.5 μ L of nuclease-free water.

Detecting transcriptomic changes by qPCR

To produce cDNA barcoded for qPCR application, the standard transcriptomic workflow was followed, except that qPCR barcodes were used rather than the standard DNA barcode fragments. In this case, for each plug three valves were opened: cells, media and a qPCR barcode plus drug mixture. After overnight incubation, addition of cell lysis and reverse transcription reagents, and further incubation, plugs were pooled and cDNA was purified using AMPURE XP beads. To quantify differential expression of the target genes, purified cDNA was diluted 10x in nuclease-free water, then 1 μ L was added to each 20 μ L reaction mixture containing nuclease-free water, 10 μ L SYBR Green, 0.25 μ L of each primer (barcode primer + gene-specific primer). 40 cycles of amplification were then performed in a StepOne™ Real-Time PCR system (Thermo Fisher Scientific Inc., USA).

Library PCR

Purified cDNA was amplified by mixing with KAPA Hifi ready mix (Kapa Biosystems, USA), and SMART primer at a final concentration of 0.8 μ M. Reaction mixture was cycled as follows:

Step	Temperature	Time
Initial denaturation	95°C	3 min
4 cycles	98°C	20 sec
	65°C	45 sec
	72°C	3 min
9 cycles	98°C	20 sec
	67°C	20 sec
	72°C	3 min
Final extension	72°C	5 min
Hold	4°C	∞

Amplified cDNA was then purified with 0.6x the volume of Ampure XT beads. cDNA concentration was quantified with the Qubit™ dsDNA HS assay kit (Thermo Fisher Scientific Inc., USA). cDNA was diluted to <5 ng/μL and the fragment size analyzed by running on a high sensitivity DNA chip, using a 2100 Bioanalyzer instrument (Agilent Technologies Inc., USA).

Tagmentation and sequencing

Purified, amplified cDNA was fragmented and sequencing linkers were introduced, using an in-house 3' tagmentation protocol (Hennig et al., 2018). This was performed by Jelena Pistolovic from the Genomics Core Facility at EMBL, Heidelberg. The only alterations from the protocol was the use of a higher starting concentration of cDNA (0.4 ng/μL), and exchange of the PE1.3'RNA-Seq i5 adapter index primer given in the protocol, with the P5-SMART adaptor primer (sequence is in the primers section of this thesis). Both cycles (replicate) of drug treated plugs was indexed separately. Libraries were pooled at equimolar ratios and paired end sequencing was performed with a MiSeq sequencer (Illumina Inc., USA) and the custom primer (given in the “primers” section). The first read was 26 bp and the second was 59 bp.

Analysis

Analysis of fluorescence data from plug-based experiments

The R package BraDiPluS (<https://github.com/saezlab/BraDiPluS/blob/master/README.md>) (Eduati et al., 2018) was used to analyze fluorescence data recorded by the “Multi-channel acquisition” program. Thresholds for intensity and plug length were chosen manually after plotting the data. Peaks in the blue channel were used to identify the change of one condition to the next. Orange fluorescence above the chosen threshold was used to identify plugs.

Analysis of RNA-seq data from K-562 drug screen

Demultiplexing and aligning of reads was carried out by Dr. Jonathan Landry from the EMBL Genomics Core Facility. Reads generated by paired-end sequencing were first assigned to replicates based on the in-line i7 illumina indices which were replicate-specific. Combinatorial barcode sequences encoding drug combinations (found on read 1) were then assigned using the Je demultiplexing software for NGS data (Girardot et al., 2016). A maximum of 6 mismatches from the reference sequence for each barcode fragment combination were allowed. The corresponding mRNA sequence found on Read 2 of the same sequenced fragment was then aligned to a reference genome. This was done using the RNA-Seq alignment tool: STAR (Dobin et al., 2013).

Analysis of mouse data was performed by Olga Ivanova from the Saez-Rodriguez group. Filtering was applied to count data by removing all genes with fewer than 150 total reads. This threshold was chosen to maximize the number of features retained, while removing the genes with low counts which show variance-mean dependence. Two samples were then removed which had been identified as having particularly low read counts. Finally the variance stabilizing transformation (vst) from DESeq2 (Love et al., 2014) was applied to produce a count matrix which is approximately homoskedastic (meaning that its variance was constant throughout the range of mean values) and which is normalized to library size. PCA analysis was then performed to determine whether conditions (drug combinations) clustered together across different cycles, and what portion of the variation between conditions could be explained by each principle component. Differential expression analysis was then performed using DESeq2 (Love et al., 2014) to compare the DMSO control vs. Imatinib treatments (at 2x concentration). The false discovery rate (FDR) threshold was set to 0.05 (adjusted p-value).

Reaction mixtures, barcode sequences, primers and PCR programs

Cell lysis, barcode ligation and reverse transcription mixtures

<u>Component:</u>	<u>Stock concentration:</u>	<u>Units:</u>	<u>Source:</u>	<u>In PCR tubes (20 uL volume):</u>	<u>Droplet-injection (700 uL at 3x):</u>
Ligase buffer	10	x	NEB	2.00	210
Perm/wash buffer*	10	%	BD	2.00	210
RNAse block	40	U/uL	Lucigen	1.00	105
Betaine	5	M	Sigma	0.25	26.25
dNTPs	25	mM	Carl Roth	0.40	42
Ligase ^x	2x10 ⁶	U/mL	NEB	0.20	21
TSO ^x	100	uM	IDT	0.50	52.5
RTase H-	200	U/uL	Thermo	0.25	26.25
Numbered barcode fragment ^o	20	uM	Sigma	1.00	105
qPCR barcode/ lettered barcode fragment ^o	20	uM	Sigma	0.50	52.5
Cells ^o	1x10 ⁶	Cells/mL		4.00	420

* Was swapped for different detergents in the detergent screen

X Was not included when barcoded cDNA was produced for qPCR

o Came from plugs in combinatorial drug screens, so not included in mix

Barcode sequences

qPCR capture barcodes

BC-1	GACAGTACAGGTCCTACACACCAGTTGATGTTTTTTTTTTTTTTTTTTTTVN
BC-2	CTGACTAGCTGTCGTCTCACTCTCGACTCATCTTTTTTTTTTTTTTTTTTTTTVN
BC-3	CATGCATCAGTCGAGACCTGACGAGTGAACAGTTTTTTTTTTTTTTTTTTTTVN
BC-4	TCGACATCTCAGATCGTGGTCGTACAGCTCACTTTTTTTTTTTTTTTTTTTTTVN

Combinatorial barcode sequences (designed by Dr. Lukas Mathur)

Numbered barcodes

BC-1	TTTTTTAAGCAGTGGTATCAACGCAGAGTACGCTCACCTGCgccgc [Pho]GCAGGTGAGCGTACTCTGCGTTGATACCACTGCTTAAAAAAA
BC-2	TTTTTTAAGCAGTGGTATCAACGCAGAGTACTACCGTCTCGgccgc [Pho]CGAGACGGTAGTACTCTGCGTTGATACCACTGCTTAAAAAAA
BC-3	TTTTTTAAGCAGTGGTATCAACGCAGAGTACAAGCTGGCTCgccgc [Pho]GAGCCAGCTTGTACTCTGCGTTGATACCACTGCTTAAAAAAA
BC-4	TTTTTTAAGCAGTGGTATCAACGCAGAGTACAAGTATCCTCgccgc [Pho]GAGGATACTTGTACTCTGCGTTGATACCACTGCTTAAAAAAA
BC-5	TTTTTTAAGCAGTGGTATCAACGCAGAGTACATCAATCCTCgccgc [Pho]GAGGATTGATGTACTCTGCGTTGATACCACTGCTTAAAAAAA
BC-6	TTTTTTAAGCAGTGGTATCAACGCAGAGTACACTACCCTCgccgc [Pho]GAGGGTGAGTGTACTCTGCGTTGATACCACTGCTTAAAAAAA

Lettered barcodes

BC-A	[Pho]GCTGTGACTGTTTTTTTTTTTTTTTTTTTTVN CAGTCACAGCgcccgc
BC-B	[Pho]GGACGCATAGTTTTTTTTTTTTTTTTTTTTVN CTATGCGTCCgcccgc
BC-C	[Pho]GGAGGATTCCTTTTTTTTTTTTTTTTTTTTTVN GGAATCCTCCgcccgc
BC-D	[Pho]ACATATATCCTTTTTTTTTTTTTTTTTTTTTVN GGATATATGTgcccgc
BC-E	[Pho]GGATGGAACATTTTTTTTTTTTTTTTTTTTTVN TGTTCCATCCgcccgc
BC-F	[Pho]ACTCTTCGTGTTTTTTTTTTTTTTTTTTTTVN CACGAAGAGTgcccgc

Primers

qPCR of Zs-green to compare detergents

Name	Sequence	Melt temp. (°C)	GC content [%]	Product length (bp)
ZsG_fw1	ACCGTGTACAAGGCCAAGTC	60	55	109
ZsG_rev1	GGTGCCACTTCTGGTTCTTG	59	55	

qPCR from plug-based reverse transcription

Barcode primer	Barcode	Melt temperature	Length	GC%
CAGGTCCTACACACCAGTTGA	1	58.7	22	50
AGCTGTCGTCTCACTCTCGAC	2	59.8	21	57.1
CGAGACCTGACGAGTGAACA	2	60	20	55
TCAGATCGTGGTCGTACAGC	3	59.9	20	55

Gene	Primer sequence	Melt temp.	Product (bp)	GC%	Reference sequence: (https://www.ncbi.nlm.nih.gov/nucore/..)
SPTA1	tccaaggcaattttcaaaca	59.1		35	NM_003126.4
PIM1	gttttgagcagcaggtagcc	60		55	NM_002648.4
EGR1	cattgaatgcgctttattgc	59.3		40	NM_001964.3
SLC25A37	ttgtgtgggatgtttctga	59.9		45	NM_001317812.2

Primers for tagmentation and sequencing

Name	Sequence (5' --> 3')
TSO	AAGCAGTGGTATCAACGCAGAGTGAATrGrGrG
SMART-Primer	AAGCAGTGGTATCAACGCAGAGT
Tn5ME-A	TCGTCGGCAGCGTCAGATGTGTATAAGAGACAG
Tn5MErev	[phos]CTGTCTCTTATACACATCT
i7 index adapter primer	CAAGCAGAAGACGGCATACGAGATnnnnnnnnGTCTCGTGGGCTCGG
P5-SMART adaptor primer	AATGATACGGCGACCACCGAGATCTACACGCCT GTCCGCGGAAGCAGTGGTATCAACGCAGAGTAC
Custom sequencing primer	GCCTGTCCGCGGAAGCAGTGGTATCAACGCAGAGTAC

5. Appendix

Abbreviations

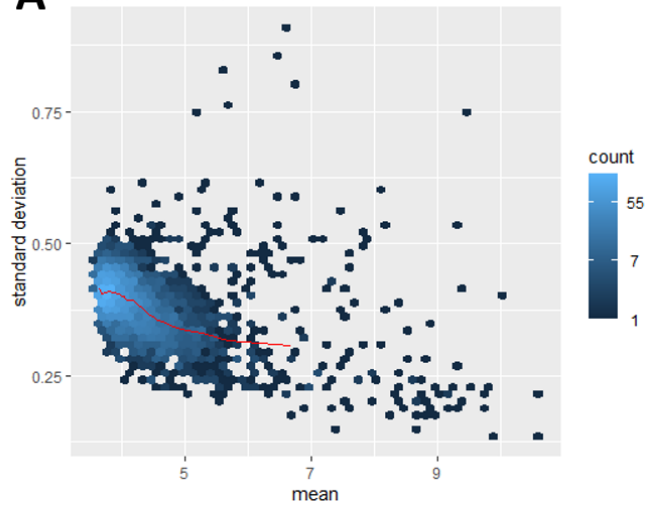
APC antigen-presenting cell	PDMS Poly-Di-Methyl-Siloxane
BC Barcode	PFO 1H,1H,2H,2H-Perfluorooctanol
BRCA1 Breast cancer 1	PMT Photomultiplier Tube
C Celsius	PTFE Polytetrafluorethylene
CRISPR-Cas9 clustered regularly interspaced short palindromic repeats associated protein 9	qPCR quantitative Polymerase Chain Reaction
CTL Cytotoxic T-lymphocyte	Rev Reverse
DMSO Dimethyl Sulfoxide	RNA Ribonucleic Acid
DNA Deoxyribonucleic acid	RNA-Seq RNA sequencing
dpi Dots per inch	rpm Revolutions per minute
dT Deoxythymidine	RT Reverse Transcription
EGFR Epidermal Growth Factor Receptor	SDS Sodium dodecyl sulfate
FBS Fetal bovine serum	TCR T-cell receptor
Fwd Forward	TME Tumor microenvironment
GR35 35% of maximum growth reduction	TSO template switching oligo
ICI Immune checkpoint inhibitor	UV Ultraviolet
ITO Indium tin oxide	
mm Millimetre	
mRNA messenger Ribonucleic Acid	
ms Milliseconds	
NGS Next Generation Sequencing	
PARP1 Poly [ADP-ribose] polymerase 1	
PBS Phosphate buffered saline	
PCA Principal Component Analysis	
PCR Polymerase Chain Reaction	

Supplementary figures

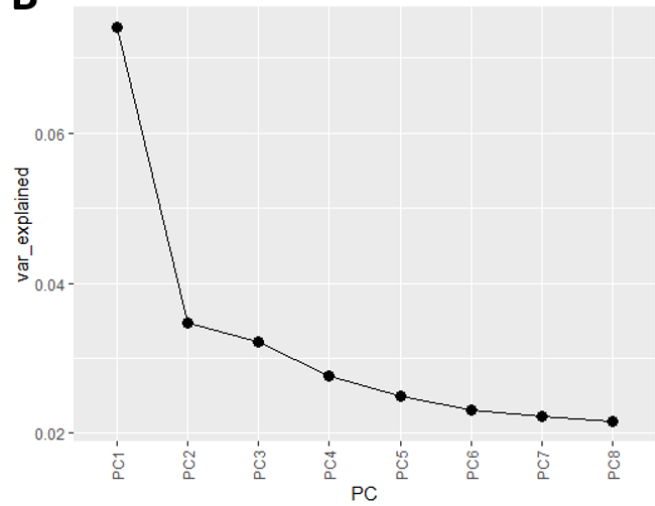
<u>Valve</u>	<u>Reagent</u>	<u>Barcode</u>
9	cells	None
10	FS	None
11	FS	None
12	FS	None
13	YM155	1
14	Imatinib	2
15	FS	3
16	YM155	4
17	Imatinib	5
18	FS	6
19	YM155	A
20	Imatinib	B
21	FS	C
22	YM155	D
23	Imatinib	E
24	FS	F

Table 5. Table of syringes and corresponding valves used for the Imatinib-Ym155 control screen.

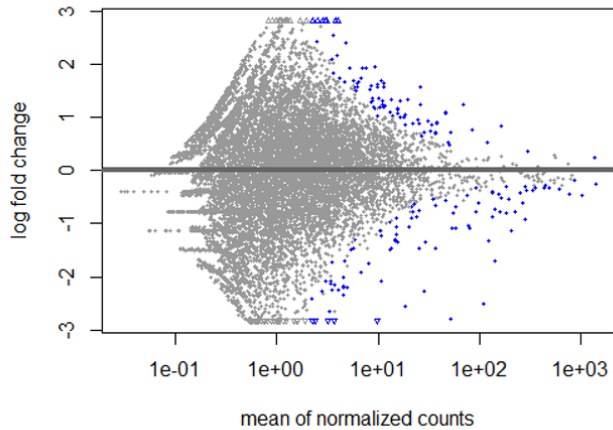
A sequencing depth normalized vst(read counts)



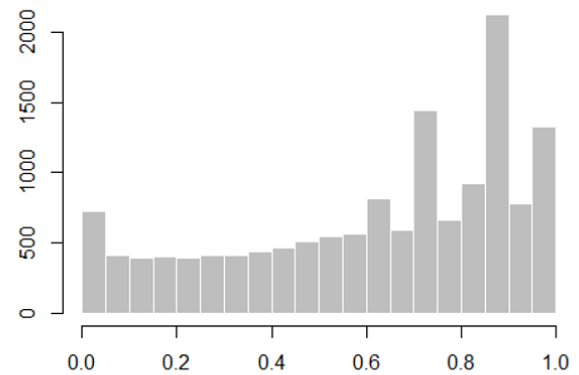
B Scree plot: PCA on scaled data



C WT vs treated



D frequencies of p-values



Supplementary Figure 5.1 QC plots by Olga Ivanova. A) Mean-sd plot showing that vst transformation combined with removal of all genes with total counts below 150, produced approximately homoscedastic data. B) Scree plot showing how variation was distributed between different principal components. An unusually small amount of variance is explained by the first principal component. C) MA plot. This shows the distribution of log₂FC values in relation to the mean normalized counts for that gene. D) Histogram of p-values following differential gene expression analysis.

6. References

- Abate, A.R., Chen, C.-H., Agresti, J.J., and Weitz, D.A. (2009). Beating Poisson encapsulation statistics using close-packed ordering. *Lab Chip* *9*, 2628-2631.
- Abate, A.R., Hung, T., Mary, P., Agresti, J.J., and Weitz, D.A. (2010). High-throughput injection with microfluidics using picoinjectors. *Proceedings of the National Academy of Sciences* *107*, 19163-19166.
- Abiko, K., Matsumura, N., Hamanishi, J., Horikawa, N., Murakami, R., Yamaguchi, K., Yoshioka, Y., Baba, T., Konishi, I., and Mandai, M. (2015). IFN- γ from lymphocytes induces PD-L1 expression and promotes progression of ovarian cancer. *Br J Cancer* *112*, 1501-1509.
- Adams, J.M., and Cory, S. (2007). The Bcl-2 apoptotic switch in cancer development and therapy. *Oncogene* *26*, 1324-1337.
- Akbay, E.A., Koyama, S., Carretero, J., Altabef, A., Tchaicha, J.H., Christensen, C.L., Mikse, O.R., Cherniack, A.D., Beauchamp, E.M., and Pugh, T.J. (2013). Activation of the PD-1 pathway contributes to immune escape in EGFR-driven lung tumors. *Cancer discovery* *3*, 1355-1363.
- Alard, E., Butnariu, A.-B., Grillo, M., Kirkham, C., Zinovkin, D., Newnham, L., Macciochi, J., and Pranjol, Z. (2020). Advances in Anti-Cancer Immunotherapy: Car-T Cell, Checkpoint Inhibitors, Dendritic Cell Vaccines, and Oncolytic Viruses, and Emerging Cellular and Molecular Targets. *Cancers* *12*.
- Alberts, B. (2014). *Molecular biology of the cell*, Sixth edn (New York, NY: Garland Science).
- Amigo, J.D., Yu, M., Troadec, M.-B., Gwynn, B., Cooney, J.D., Lambert, A.J., Chi, N.C., Weiss, M.J., Peters, L.L., Kaplan, J., *et al.* (2011). Identification of distal cis-regulatory elements at mouse mitoferrin loci using zebrafish transgenesis. *Mol Cell Biol* *31*, 1344-1356.
- Anders, S., and Huber, W. (2010). Differential expression analysis for sequence count data. *Genome Biol* *11*, R106.
- Andersson, E.I., Pützer, S., Yadav, B., Dufva, O., Khan, S., He, L., Sellner, L., Schrader, A., Crispatzu, G., Oleś, M., *et al.* (2018). Discovery of novel drug sensitivities in T-PLL by high-throughput ex vivo drug testing and mutation profiling. *Leukemia* *32*, 774-787.

- Berdasco, M., and Esteller, M. (2010). Aberrant Epigenetic Landscape in Cancer: How Cellular Identity Goes Awry. *Developmental Cell* 19, 698-711.
- Birchmeier, W., and Behrens, J. (1994). Cadherin expression in carcinomas: role in the formation of cell junctions and the prevention of invasiveness. *Biochimica et Biophysica Acta (BBA)-Reviews on Cancer* 1198, 11-26.
- Bruch, P.-M., Giles, H.A.R., Kolb, C., Herbst, S.A., Becirovic, T., Roeder, T., Lu, J., Scheinost, S., Wagner, L., Huellein, J., *et al.* (2021). Mapping drug-microenvironment-genetic interplay in CLL reveals trisomy 12 as a modulator of microenvironmental signals. *bioRxiv*, 2021.2007.2023.453514.
- Cameron, F., Whiteside, G., and Perry, C. (2011). Ipilimumab. *Drugs* 71, 1093-1104.
- Carmeliet, P. (2005). VEGF as a Key Mediator of Angiogenesis in Cancer. *Oncology* 69(suppl 3), 4-10.
- Castells-Roca, L., Tejero, E., Rodríguez-Santiago, B., and Surrallés, J. (2021). CRISPR Screens in Synthetic Lethality and Combinatorial Therapies for Cancer. *Cancers* 13, 1591.
- Cavallaro, U., and Christofori, G. (2004). Cell adhesion and signalling by cadherins and Ig-CAMs in cancer. *Nature Reviews Cancer* 4, 118-132.
- Cerignoli, F., Abassi, Y.A., Lamarche, B.J., Guenther, G., Santa Ana, D., Guimet, D., Zhang, W., Zhang, J., and Xi, B. (2018). In vitro immunotherapy potency assays using real-time cell analysis. *PLOS ONE* 13, e0193498.
- Chapman, P.B., Hauschild, A., Robert, C., Haanen, J.B., Ascierto, P., Larkin, J., Dummer, R., Garbe, C., Testori, A., and Maio, M. (2011). Improved survival with vemurafenib in melanoma with BRAF V600E mutation. *New England Journal of Medicine* 364, 2507-2516.
- Chatila, T., Silverman, L., Miller, R., and Geha, R. (1989). Mechanisms of T cell activation by the calcium ionophore ionomycin. *The Journal of Immunology* 143, 1283.
- Chen, Daniel S., and Mellman, I. (2013). Oncology Meets Immunology: The Cancer-Immunity Cycle. *Immunity* 39, 1-10.
- Choudhury, D., van Noort, D., Iliescu, C., Zheng, B., Poon, K.-L., Korzh, S., Korzh, V., and Yu, H. (2012).

Fish and Chips: a microfluidic perfusion platform for monitoring zebrafish development. *Lab Chip* *12*, 892-900.

Cieřlik, M., and Chinnaiyan, A.M. (2018). Cancer transcriptome profiling at the juncture of clinical translation. *Nature Reviews Genetics* *19*, 93-109.

Clausell-Tormos, J., Griffiths, A.D., and Merten, C.A. (2010). An automated two-phase microfluidic system for kinetic analyses and the screening of compound libraries. *Lab Chip* *10*, 1302-1307.

Collins, A.V., Brodie, D.W., Gilbert, R.J.C., Iaboni, A., Manso-Sancho, R., Walse, B., Stuart, D.I., van der Merwe, P.A., and Davis, S.J. (2002). The Interaction Properties of Costimulatory Molecules Revisited. *Immunity* *17*, 201-210.

Costello, J.C., Heiser, L.M., Georgii, E., Gonen, M., Menden, M.P., Wang, N.J., Bansal, M., Ammad-uddin, M., Hintsanen, P., Khan, S.A., *et al.* (2014). A community effort to assess and improve drug sensitivity prediction algorithms. *Nat Biotechnol* *32*, 1202-1212.

Cottagnoud, P., Cottagnoud, M., and Tauber, M. (2003). Vancomycin acts synergistically with gentamicin against penicillin-resistant pneumococci by increasing the intracellular penetration of gentamicin. *Antimicrobial agents and chemotherapy* *47*, 144-147.

Crick, F. (1958). On protein synthesis. *Symposia of the Society for Experimental Biology* *12*, 138-163.

Criss, S.D., Mooradian, M.J., Watson, T.R., Gainor, J.F., Reynolds, K.L., and Kong, C.Y. (2019). Cost-effectiveness of Atezolizumab Combination Therapy for First-Line Treatment of Metastatic Nonsquamous Non-Small Cell Lung Cancer in the United States. *JAMA network open* *2*, e1911952-e1911952.

Crystal, A.S., Shaw, A.T., Sequist, L.V., Friboulet, L., Niederst, M.J., Lockerman, E.L., Frias, R.L., Gainor, J.F., Amzallag, A., Greninger, P., *et al.* (2014). Patient-derived models of acquired resistance can identify effective drug combinations for cancer. *Science* *346*, 1480-1486.

Davoli, T., Xu, Andrew W., Mengwasser, Kristen E., Sack, Laura M., Yoon, John C., Park, Peter J., and Elledge, Stephen J. (2013). Cumulative Haploinsufficiency and Triplosensitivity Drive Aneuploidy Patterns and Shape the Cancer Genome. *Cell* *155*, 948-962.

DeBerardinis, R.J., Lum, J.J., Hatzivassiliou, G., and Thompson, C.B. (2008). The biology of cancer: metabolic reprogramming fuels cell growth and proliferation. *Cell metabolism* 7, 11-20.

Dietrich, S., Oles, M., Lu, J., Sellner, L., Anders, S., Velten, B., Wu, B., Hullein, J., da Silva Liberio, M., Walther, T., *et al.* (2018). Drug-perturbation-based stratification of blood cancer. *J Clin Invest* 128, 427-445.

Dobin, A., Davis, C.A., Schlesinger, F., Drenkow, J., Zaleski, C., Jha, S., Batut, P., Chaisson, M., and Gingeras, T.R. (2013). STAR: ultrafast universal RNA-seq aligner. *Bioinformatics* 29, 15-21.

Dorfman, N.A., Civin, C.I., and Wunderlich, J.R. (1980). Susceptibility of adherent versus suspension target cells derived from adherent tissue culture lines to cell-mediated cytotoxicity in rapid ⁵¹Cr-release assays. *Journal of Immunological Methods* 32, 127-139.

Druker, B.J., Talpaz, M., Resta, D.J., Peng, B., Buchdunger, E., Ford, J.M., Lydon, N.B., Kantarjian, H., Capdeville, R., Ohno-Jones, S., *et al.* (2001). Efficacy and safety of a specific inhibitor of the BCR-ABL tyrosine kinase in chronic myeloid leukemia. *N Engl J Med* 344, 1031-1037.

Duffy, D.C., McDonald, J.C., Schueller, O.J.A., and Whitesides, G.M. (1998). Rapid Prototyping of Microfluidic Systems in Poly(dimethylsiloxane). *Anal Chem* 70, 4974-4984.

Eduati, F., Jaaks, P., Wappler, J., Cramer, T., Merten, C.A., Garnett, M.J., and Saez-Rodriguez, J. (2020). Patient-specific logic models of signaling pathways from screenings on cancer biopsies to prioritize personalized combination therapies. *Molecular Systems Biology* 16, e8664.

Eduati, F., Utharala, R., Madhavan, D., Neumann, U.P., Longerich, T., Cramer, T., Saez-Rodriguez, J., and Merten, C.A. (2018). A microfluidics platform for combinatorial drug screening on cancer biopsies. *Nat Commun* 9, 2434.

Evan, G., and Littlewood, T. (1998). A matter of life and cell death. *Science* 281, 1317-1322.

Fan, H.C., Wang, J., Potanina, A., and Quake, S.R. (2011). Whole-genome molecular haplotyping of single cells. *Nat Biotechnol* 29, 51-57.

Farber, S., and Diamond, L. (1948). Temporary remissions in acute leukemia in children produced by

folic acid antagonist, 4-aminopteroyl-glutamic acid. *The New England journal of medicine* 238 23, 787-793.

Ferlay, J., Shin, H.-R., Bray, F., Forman, D., Mathers, C., and Parkin, D.M. (2010). Estimates of worldwide burden of cancer in 2008: GLOBOCAN 2008. *International Journal of Cancer* 127, 2893-2917.

Feuk, L., Carson, A.R., and Scherer, S.W. (2006). Structural variation in the human genome. *Nature Reviews Genetics* 7, 85-97.

Fidler, I.J. (2003). The pathogenesis of cancer metastasis: the 'seed and soil' hypothesis revisited. *Nature Reviews Cancer* 3, 453-458.

Frank, T., and Tay, S. (2013). Flow-switching allows independently programmable, extremely stable, high-throughput diffusion-based gradients. *Lab Chip* 13, 1273-1281.

FREI, E., III, KARON, M., LEVIN, R.H., FREIREICH, E.J., TAYLOR, R.J., HANANIAN, J., SELAWRY, O., HOLLAND, J.F., HOOGSTATEN, B., WOLMAN, I.J., *et al.* (1965). The Effectiveness of Combinations of Antileukemic Agents in Inducing and Maintaining Remission in Children with Acute Leukemia. *Blood* 26, 642-656.

Ganesan, A., Ahmed, M., Okoye, I., Arutyunova, E., Babu, D., Turnbull, W.L., Kundu, J.K., Shields, J., Agopsowicz, K.C., Xu, L., *et al.* (2019). Comprehensive in vitro characterization of PD-L1 small molecule inhibitors. *Scientific Reports* 9, 12392.

Garrido, F., Ruiz-Cabello, F., Cabrera, T., Perez-Villar, J.J., López-Botet, M., Duggan-Keen, M., and Stern, P.L. (1997). Implications for immunosurveillance of altered HLA class I phenotypes in human tumours. *Immunology today* 18, 89-95.

Genomes Project, C., Abecasis, G.R., Auton, A., Brooks, L.D., DePristo, M.A., Durbin, R.M., Handsaker, R.E., Kang, H.M., Marth, G.T., and McVean, G.A. (2012). An integrated map of genetic variation from 1,092 human genomes. *Nature* 491, 56-65.

Gilad, Y., Gellerman, G., Lonard, D.M., and O'Malley, B.W. (2021). Drug Combination in Cancer Treatment-From Cocktails to Conjugated Combinations. *Cancers* 13, 669.

Girardot, C., Scholtalbers, J., Sauer, S., Su, S.-Y., and Furlong, E.E.M. (2016). Je, a versatile suite to handle multiplexed NGS libraries with unique molecular identifiers. *BMC Bioinformatics* 17, 419-419.

Goldenberger, D., Perschil, I., Ritzler, M., and Altwegg, M. (1995). A simple "universal" DNA extraction procedure using SDS and proteinase K is compatible with direct PCR amplification. *PCR methods and applications* 4 6, 368-370.

Gómez-Sjöberg, R., Leyrat, A.A., Pirone, D.M., Chen, C.S., and Quake, S.R. (2007). Versatile, Fully Automated, Microfluidic Cell Culture System. *Anal Chem* 79, 8557-8563.

Goodman, L.S., WINTROBE, M.M., DAMESHEK, W., GOODMAN, M.J., GILMAN, A., and McLENNAN, M.T. (1946). NITROGEN MUSTARD THERAPY: Use of Methyl-Bis(Beta-Chloroethyl)amine Hydrochloride and Tris(Beta-Chloroethyl)amine Hydrochloride for Hodgkin's Disease, Lymphosarcoma, Leukemia and Certain Allied and Miscellaneous Disorders. *Journal of the American Medical Association* 132, 126-132.

Greaves, M. (2016). Leukaemia 'firsts' in cancer research and treatment. *Nature Reviews Cancer* 16, 163-172.

Gregg, J., and Fraizer, G. (2011). Transcriptional Regulation of EGR1 by EGF and the ERK Signaling Pathway in Prostate Cancer Cells. *Genes & Cancer* 2, 900-909.

Grivennikov, S.I., Greten, F.R., and Karin, M. (2010). Immunity, inflammation, and cancer. *Cell* 140, 883-899.

Gruner, P., Riechers, B., Semin, B., Lim, J., Johnston, A., Short, K., and Baret, J.-C. (2016). Controlling molecular transport in minimal emulsions. *Nature Communications* 7, 10392.

Gu, W., Zhu, X., Futai, N., Cho, B.S., and Takayama, S. (2004). Computerized microfluidic cell culture using elastomeric channels and Braille displays. *P Natl Acad Sci USA* 101, 15861-15866.

Hafner, M., Niepel, M., Chung, M., and Sorger, P.K. (2016). Growth rate inhibition metrics correct for confounders in measuring sensitivity to cancer drugs. *Nature methods* 13, 521-527.

Håkansson, P., Nilsson, B., Andersson, A., Lassen, C., Gullberg, U., and Fioretos, T. (2008). Gene expression analysis of BCR/ABL1-dependent transcriptional response reveals enrichment for genes

involved in negative feedback regulation. *Genes, Chromosomes and Cancer* 47, 267-275.

Han, Y., Liu, D., and Li, L. (2020). PD-1/PD-L1 pathway: current researches in cancer. *Am J Cancer Res* 10, 727-742.

Hanahan, D., and Weinberg, R.A. (2000). The hallmarks of cancer. *Cell* 100, 57-70.

Hanahan, D., and Weinberg, Robert A. (2011). Hallmarks of Cancer: The Next Generation. *Cell* 144, 646-674.

Hara, Y., and Merten, Christoph A. (2015). Dynein-Based Accumulation of Membranes Regulates Nuclear Expansion in *Xenopus laevis* Egg Extracts. *Developmental Cell* 33, 562-575.

Haslam, A., and Prasad, V. (2019). Estimation of the Percentage of US Patients With Cancer Who Are Eligible for and Respond to Checkpoint Inhibitor Immunotherapy Drugs. *JAMA Network Open* 2, e192535-e192535.

Hazlehurst, L.A., Bewry, N.N., Nair, R.R., and Pinilla-Ibarz, J. (2009). Signaling Networks Associated with BCR–ABL–Dependent Transformation. *Cancer Control* 16, 100-107.

Henke, E., Nandigama, R., and Ergün, S. (2020). Extracellular Matrix in the Tumor Microenvironment and Its Impact on Cancer Therapy. *Frontiers in Molecular Biosciences* 6.

Hennig, B.P., Velten, L., Racke, I., Tu, C.S., Thoms, M., Rybin, V., Besir, H., Remans, K., and Steinmetz, L.M. (2018). Large-Scale Low-Cost NGS Library Preparation Using a Robust Tn5 Purification and Tagmentation Protocol. *G3 (Bethesda)* 8, 79-89.

Herbst, R.S., Gordon, M.S., Fine, G.D., Sosman, J.A., Soria, J.-C., Hamid, O., Powderly, J.D., Burris, H.A., Mokatzin, A., and Kowanetz, M. (2013). A study of MPDL3280A, an engineered PD-L1 antibody in patients with locally advanced or metastatic tumors (American Society of Clinical Oncology).

Hicklin, D.J., Marincola, F.M., and Ferrone, S. (1999). HLA class I antigen downregulation in human cancers: T-cell immunotherapy revives an old story. *Molecular medicine today* 5, 178-186.

Hirohashi, S. (1998). Inactivation of the E-cadherin-mediated cell adhesion system in human cancers. *The American journal of pathology* 153, 333-339.

Hodi, F.S., O'Day, S.J., McDermott, D.F., Weber, R.W., Sosman, J.A., Haanen, J.B., Gonzalez, R., Robert, C., Schadendorf, D., and Hassel, J.C. (2010). Improved survival with ipilimumab in patients with metastatic melanoma. *New England Journal of Medicine* 363, 711-723.

Hsu, P.P., and Sabatini, D.M. (2008). Cancer cell metabolism: Warburg and beyond. *Cell* 134, 703-707.

Huberts, D.H.E.W., Sik Lee, S., González, J., Janssens, G.E., Vizcarra, I.A., and Heinemann, M. (2013). Construction and use of a microfluidic dissection platform for long-term imaging of cellular processes in budding yeast. *Nat Protoc* 8, 1019-1027.

Huh, D., Matthews, B.D., Mammoto, A., Montoya-Zavala, M., Hsin, H.Y., and Ingber, D.E. (2010). Reconstituting Organ-Level Lung Functions on a Chip. *Science* 328, 1662.

Hungerford, D., and Nowell, P. (1960). A minute chromosome in human chronic granulocytic leukemia. *Science* 132, 1497-1499.

Iorio, F., Knijnenburg, T.A., Vis, D.J., Bignell, G.R., Menden, M.P., Schubert, M., Aben, N., Goncalves, E., Barthorpe, S., Lightfoot, H., *et al.* (2016). A Landscape of Pharmacogenomic Interactions in Cancer. *Cell* 166, 740-754.

Iwatsuki, M., Mimori, K., Yokobori, T., Ishi, H., Beppu, T., Nakamori, S., Baba, H., and Mori, M. (2010). Epithelial–mesenchymal transition in cancer development and its clinical significance. *Cancer Science* 101, 293-299.

Jaitin, D.A., Kenigsberg, E., Keren-Shaul, H., Elefant, N., Paul, F., Zaretsky, I., Mildner, A., Cohen, N., Jung, S., Tanay, A., *et al.* (2014). Massively parallel single-cell RNA-seq for marker-free decomposition of tissues into cell types. *Science (New York, NY)* 343, 776-779.

Jia, J., Zhu, F., Ma, X., Cao, Z.W., Li, Y.X., and Chen, Y.Z. (2009). Mechanisms of drug combinations: interaction and network perspectives. *Nature reviews Drug discovery* 8, 111-128.

Johnsen, A., Templeton, D., Sy, M.-S., and Harding, C. (1999). Deficiency of transporter for antigen presentation (TAP) in tumor cells allows evasion of immune surveillance and increases tumorigenesis. *The Journal of Immunology* 163, 4224-4231.

Kaderbhai, C., Tharin, Z., and Ghiringhelli, F. (2019). The Role of Molecular Profiling to Predict the Response to Immune Checkpoint Inhibitors in Lung Cancer. *Cancers* 11, 201.

Kang, H.M., Subramaniam, M., Targ, S., Nguyen, M., Maliskova, L., McCarthy, E., Wan, E., Wong, S., Byrnes, L., Lanata, C.M., *et al.* (2018). Multiplexed droplet single-cell RNA-sequencing using natural genetic variation. *Nat Biotechnol* 36, 89-94.

Khandelwal, N., Breinig, M., Speck, T., Michels, T., Kreutzer, C., Sorrentino, A., Sharma, A.K., Umansky, L., Conrad, H., Poschke, I., *et al.* (2015). A high-throughput RNAi screen for detection of immune-checkpoint molecules that mediate tumor resistance to cytotoxic T lymphocytes. *EMBO Molecular Medicine* 7, 450-463.

Khurana, E., Fu, Y., Chakravarty, D., Demichelis, F., Rubin, M.A., and Gerstein, M. (2016). Role of non-coding sequence variants in cancer. *Nature Reviews Genetics* 17, 93-108.

Kim, R. (2007). Cancer immunoediting: from immune surveillance to immune escape. *Cancer Immunotherapy*, 9-27.

Kimura, H., Ikeda, T., Nakayama, H., Sakai, Y., and Fujii, T. (2014). An On-Chip Small Intestine–Liver Model for Pharmacokinetic Studies. *Journal of Laboratory Automation* 20, 265-273.

Klein, Allon M., Mazutis, L., Akartuna, I., Tallapragada, N., Veres, A., Li, V., Peshkin, L., Weitz, David A., and Kirschner, Marc W. (2015). Droplet Barcoding for Single-Cell Transcriptomics Applied to Embryonic Stem Cells. *Cell* 161, 1187-1201.

Knijnenburg, T.A., Klau, G.W., Iorio, F., Garnett, M.J., McDermott, U., Shmulevich, I., and Wessels, L.F.A. (2016). Logic models to predict continuous outputs based on binary inputs with an application to personalized cancer therapy. *Scientific reports* 6, 36812-36812.

Kon, E., and Benhar, I. (2019). Immune checkpoint inhibitor combinations: Current efforts and important aspects for success. *Drug Resistance Updates* 45, 13-29.

Kulesa, A., Kehe, J., Hurtado, J.E., Tawde, P., and Blainey, P.C. (2018). Combinatorial drug discovery in nanoliter droplets. *Proceedings of the National Academy of Sciences* 115, 6685-6690.

Lamb, J., Crawford, E.D., Peck, D., Modell, J.W., Blat, I.C., Wrobel, M.J., Lerner, J., Brunet, J.-P., Subramanian, A., Ross, K.N., *et al.* (2006). The Connectivity Map: Using Gene-Expression Signatures to Connect Small Molecules, Genes, and Disease. *Science* *313*, 1929.

Lamberti, A., Marasso, S.L., and Cocuzza, M. (2014). PDMS membranes with tunable gas permeability for microfluidic applications. *RSC Advances* *4*, 61415-61419.

Lapidus, R.G., Xu, W., Spicer, E., Hoover, R., and Zhang, J. (2006). PARP inhibitors enhance the effect of cisplatin against tumors and ameliorate cisplatin-induced neuropathy. *Cancer Res* *66*, 506.

Leach, D.R., Krummel, M.F., and Allison, J.P. (1996). Enhancement of Antitumor Immunity by CTLA-4 Blockade. *Science* *271*, 1734.

Lee, D.W., Choi, Y.S., Seo, Y.J., Lee, M.Y., Jeon, S.Y., Ku, B., Kim, S., Yi, S.H., and Nam, D.H. (2014). High-Throughput Screening (HTS) of Anticancer Drug Efficacy on a Micropillar/Microwell Chip Platform. *Anal Chem* *86*, 535-542.

Li, T.-t., Liu, M.-r., and Pei, D.-s. (2019). Friend or foe, the role of EGR-1 in cancer. *Medical Oncology* *37*, 7.

Lin, M., Whitmire, S., Chen, J., Farrel, A., Shi, X., and Guo, J.-t. (2017). Effects of short indels on protein structure and function in human genomes. *Scientific Reports* *7*, 9313.

Link, D.R., Grasland-Mongrain, E., Duri, A., Sarrazin, F., Cheng, Z., Cristobal, G., Marquez, M., and Weitz, D.A. (2006). Electric Control of Droplets in Microfluidic Devices. *Angewandte Chemie International Edition* *45*, 2556-2560.

Liu, A., Trairatphisan, P., Gjerga, E., Didangelos, A., Barratt, J., and Saez-Rodriguez, J. (2019). From expression footprints to causal pathways: contextualizing large signaling networks with CARNIVAL. *npj Systems Biology and Applications* *5*, 40.

Love, M.I., Huber, W., and Anders, S. (2014). Moderated estimation of fold change and dispersion for RNA-seq data with DESeq2. *Genome Biol* *15*, 550.

Lovitt, C.J., Shelper, T.B., and Avery, V.M. (2018). Doxorubicin resistance in breast cancer cells is

mediated by extracellular matrix proteins. *Bmc Cancer* 18, 41-41.

Lowe, S.W., Cepero, E., and Evan, G. (2004). Intrinsic tumour suppression. *Nature* 432, 307-315.

Lucchetta, E.M., Lee, J.H., Fu, L.A., Patel, N.H., and Ismagilov, R.F. (2005). Dynamics of *Drosophila* embryonic patterning network perturbed in space and time using microfluidics. *Nature* 434, 1134-1138.

Luszczak, S., Kumar, C., Sathyadevan, V.K., Simpson, B.S., Gately, K.A., Whitaker, H.C., and Heavey, S. (2020). PIM kinase inhibition: co-targeted therapeutic approaches in prostate cancer. *Signal Transduct Target Ther* 5, 7-7.

Lytovchenko, O., and Kunji, E.R.S. (2017). Expression and putative role of mitochondrial transport proteins in cancer. *Biochimica et Biophysica Acta (BBA) - Bioenergetics* 1858, 641-654.

Macosko, Evan Z., Basu, A., Satija, R., Nemesh, J., Shekhar, K., Goldman, M., Tirosh, I., Bialas, Allison R., Kamitaki, N., Martersteck, Emily M., *et al.* (2015). Highly Parallel Genome-wide Expression Profiling of Individual Cells Using Nanoliter Droplets. *Cell* 161, 1202-1214.

Marquart, J., Chen, E.Y., and Prasad, V. (2018). Estimation of the Percentage of US Patients With Cancer Who Benefit From Genome-Driven Oncology. *JAMA Oncol* 4, 1093-1098.

Martincorena, I., Raine, K.M., Gerstung, M., Dawson, K.J., Haase, K., Van Loo, P., Davies, H., Stratton, M.R., and Campbell, P.J. (2017). Universal Patterns of Selection in Cancer and Somatic Tissues. *Cell* 171, 1029-1041.e1021.

Mathur, L., Ballinger, M., Utharala, R., and Merten, C.A. (2019). Microfluidics as an Enabling Technology for Personalized Cancer Therapy. *Small* 16, 1904321.

Mathur, L., Salai, B., Utharala, R., Ballinger, M., Landry, J., Ryckelynck, M., Benes, V., Saez-Rodriguez, J., and Merten, C. (2021). Gene expression-based profiling of drug combinations using deterministic barcoding in picolitre sized droplets. Manuscript in review.

McFarland, J.M., Paoletta, B.R., Warren, A., Geiger-Schuller, K., Shibue, T., Rothberg, M., Kuksenko, O., Colgan, W.N., Jones, A., Chambers, E., *et al.* (2020). Multiplexed single-cell transcriptional response profiling to define cancer vulnerabilities and therapeutic mechanism of action. *Nature Communications*

11, 4296.

McLendon, R., Friedman, A., Bigner, D., Van Meir, E.G., Brat, D.J., M. Mastrogiannis, G., Olson, J.J., Mikkelsen, T., Lehman, N., Aldape, K., *et al.* (2008). Comprehensive genomic characterization defines human glioblastoma genes and core pathways. *Nature* 455, 1061-1068.

Meyers, D.E., Bryan, P.M., Banerji, S., and Morris, D.G. (2018). Targeting the PD-1/PD-L1 axis for the treatment of non-small-cell lung cancer. *Curr Oncol* 25, e324-e334.

Moasser, M.M. (2007). The oncogene HER2: its signaling and transforming functions and its role in human cancer pathogenesis. *Oncogene* 26, 6469-6487.

Montero, J., Sarosiek, K.A., DeAngelo, J.D., Maertens, O., Ryan, J., Ercan, D., Piao, H., Horowitz, N.S., Berkowitz, R.S., Matulonis, U., *et al.* (2015). Drug-induced death signaling strategy rapidly predicts cancer response to chemotherapy. *Cell* 160, 977-989.

Negrini, S., Gorgoulis, V.G., and Halazonetis, T.D. (2010). Genomic instability — an evolving hallmark of cancer. *Nature Reviews Molecular Cell Biology* 11, 220-228.

Nelson, B.H. (2008). The impact of T-cell immunity on ovarian cancer outcomes. *Immunological reviews* 222, 101-116.

Neumann, F., Bruennert, D.C., Koch, A.-M., Bruns, I., Gattermann, N., Kronenwett, R., and Haas, R. (2007). Transcriptional Changes Induced by Imatinib and Nilotinib in the Chronic Myelogenous Leukemia (CML) Cell Line K562. *Blood* 110, 4540-4540.

Nicolet, B.P., Guislain, A., van Alphen, F.P.J., Gomez-Eerland, R., Schumacher, T.N.M., van den Biggelaar, M., and Wolkers, M.C. (2020). CD29 identifies IFN- γ -producing human CD8(+) T cells with an increased cytotoxic potential. *P Natl Acad Sci USA* 117, 6686-6696.

O'Connor, R., Cesano, A., Lange, B., Finan, J., Nowell, P.C., Clark, S.C., Raimondi, S.C., Rovera, G., and Santoli, D. (1991). Growth factor requirements of childhood acute T-lymphoblastic leukemia: correlation between presence of chromosomal abnormalities and ability to grow permanently in vitro. *Blood* 77, 1534-1545.

Olivier, M., Hollstein, M., and Hainaut, P. (2010). TP53 mutations in human cancers: origins, consequences, and clinical use. *Cold Spring Harb Perspect Biol* 2, a001008-a001008.

Ozkumur, E., Shah, A.M., Ciciliano, J.C., Emmink, B.L., Miyamoto, D.T., Brachtel, E., Yu, M., Chen, P.I., Morgan, B., Trautwein, J., *et al.* (2013). Inertial Focusing for Tumor Antigen-Dependent and -Independent Sorting of Rare Circulating Tumor Cells. *Sci Transl Med* 5.

Pages, F., Galon, J., Dieu-Nosjean, M., Tartour, E., Sautes-Fridman, C., and Fridman, W. (2010). Immune infiltration in human tumors: a prognostic factor that should not be ignored. *Oncogene* 29, 1093-1102.

Parca, L., Pepe, G., Pietrosanto, M., Galvan, G., Galli, L., Palmeri, A., Sciandrone, M., Ferrè, F., Ausiello, G., and Helmer-Citterich, M. (2019). Modeling cancer drug response through drug-specific informative genes. *Scientific Reports* 9, 15222.

Pasche, B. (2001). Role of transforming growth factor beta in cancer. *Journal of cellular physiology* 186, 153-168.

Peck, D., Crawford, E.D., Ross, K.N., Stegmaier, K., Golub, T.R., and Lamb, J. (2006). A method for high-throughput gene expression signature analysis. *Genome Biol* 7, R61-R61.

Pemovska, T., Kontro, M., Yadav, B., Edgren, H., Eldfors, S., Szwajda, A., Almusa, H., Beshpalov, M.M., Ellonen, P., Elonen, E., *et al.* (2013). Individualized systems medicine strategy to tailor treatments for patients with chemorefractory acute myeloid leukemia. *Cancer Discov* 3, 1416-1429.

Picelli, S., Faridani, O.R., Björklund, Å.K., Winberg, G., Sagasser, S., and Sandberg, R. (2014). Full-length RNA-seq from single cells using Smart-seq2. *Nat Protoc* 9, 171-181.

Pon, J.R., and Marra, M.A. (2015). Driver and Passenger Mutations in Cancer. *Annual Review of Pathology: Mechanisms of Disease* 10, 25-50.

Popova, A.A., Dietrich, S., Huber, W., Reischl, M., Peravali, R., and Levkin, P.A. (2020). Miniaturized Drug Sensitivity and Resistance Test on Patient-Derived Cells Using Droplet-Microarray. *SLAS TECHNOLOGY: Translating Life Sciences Innovation* 26, 274-286.

Principe, D.R., Chiec, L., Mohindra, N.A., and Munshi, H.G. (2021). Regulatory T-Cells as an Emerging

Barrier to Immune Checkpoint Inhibition in Lung Cancer. *Frontiers in Oncology* 11.

Pui, C.-H., and Evans, W.E. (2013). A 50-year journey to cure childhood acute lymphoblastic leukemia. *Semin Hematol* 50, 185-196.

Rajer, M., and Kmet, M. (2005). Quantitative analysis of fine needle aspiration biopsy samples. *Radiology and Oncology* 39.

Ramanathan, N., Simakov, O., Merten, C.A., and Arendt, D. (2015). Quantifying Preferences and Responsiveness of Marine Zooplankton to Changing Environmental Conditions using Microfluidics. *PLOS ONE* 10, e0140553.

Ramensky, V., Bork, P., and Sunyaev, S. (2002). Human non-synonymous SNPs: server and survey. *Nucleic acids research* 30, 3894-3900.

Restifo, N.P., Esquivel, F., Kawakami, Y., Yewdell, J.W., Mulé, J.J., Rosenberg, S.A., and Bennink, J.R. (1993). Identification of human cancers deficient in antigen processing. *The Journal of experimental medicine* 177, 265-272.

Ritchie, M.E., Phipson, B., Wu, D., Hu, Y., Law, C.W., Shi, W., and Smyth, G.K. (2015). limma powers differential expression analyses for RNA-sequencing and microarray studies. *Nucleic Acids Research* 43, e47-e47.

Rodriguez-Revena, L., Mila, M., Rosenberg, C., Lamb, A., and Lee, C. (2007). Structural variation in the human genome: the impact of copy number variants on clinical diagnosis. *Genetics in Medicine* 9, 600-606.

Roskoski, R. (2019). Properties of FDA-approved small molecule protein kinase inhibitors. *Pharmacological Research* 144, 19-50.

Rotem-Yehudar, R., Groettrup, M., Soza, A., Kloetzel, P.M., and Ehrlich, R. (1996). LMP-associated proteolytic activities and TAP-dependent peptide transport for class 1 MHC molecules are suppressed in cell lines transformed by the highly oncogenic adenovirus 12. *The Journal of experimental medicine* 183, 499-514.

- Rowshanravan, B., Halliday, N., and Sansom, D.M. (2018). CTLA-4: a moving target in immunotherapy. *Blood* 131, 58-67.
- Schoenborn, J.R., and Wilson, C.B. (2007). Regulation of Interferon- γ During Innate and Adaptive Immune Responses. In *Advances in Immunology* (Academic Press), pp. 41-101.
- Seliger, B., Maeurer, M.J., and Ferrone, S. (1997). TAP off—tumors on. *Immunology today* 18, 292-299.
- Shay, J.W., and Bacchetti, S. (1997). A survey of telomerase activity in human cancer. *European Journal of Cancer* 33, 787-791.
- Shoemaker, R.H. (2006). The NCI60 human tumour cell line anticancer drug screen. *Nature Reviews Cancer* 6, 813-823.
- Shultz, M.D. (2019). Two Decades under the Influence of the Rule of Five and the Changing Properties of Approved Oral Drugs. *Journal of Medicinal Chemistry* 62, 1701-1714.
- Shum, D., Radu, C., Kim, E., Cajuste, M., Shao, Y., Seshan, V.E., and Djaballah, H. (2008). A high density assay format for the detection of novel cytotoxic agents in large chemical libraries. *J Enzyme Inhib Med Chem* 23, 931-945.
- Somasundaram, R., Caputo, L., Guerry, D., and Herlyn, D. (2005). CD8+, HLA-unrestricted, cytotoxic T-lymphocyte line against malignant melanoma. *Journal of Translational Medicine* 3, 41.
- Srivastava, S., and Riddell, S.R. (2015). Engineering CAR-T cells: Design concepts. *Trends in Immunology* 36, 494-502.
- Strebhardt, K., and Ullrich, A. (2008). Paul Ehrlich's magic bullet concept: 100 years of progress. *Nature Reviews Cancer* 8, 473-480.
- Subramanian, A., Narayan, R., Corsello, S.M., Peck, D.D., Natoli, T.E., Lu, X., Gould, J., Davis, J.F., Tubelli, A.A., Asiedu, J.K., *et al.* (2017). A Next Generation Connectivity Map: L1000 Platform and the First 1,000,000 Profiles. *Cell* 171, 1437-1452.e1417.
- Sun, X., Vilar, S., and Tatonetti, N.P. (2013). High-Throughput Methods for Combinatorial Drug Discovery. *Sci Transl Med* 5, 205rv201.

Sung, H., Ferlay, J., Siegel, R.L., Laversanne, M., Soerjomataram, I., Jemal, A., and Bray, F. (2021). Global Cancer Statistics 2020: GLOBOCAN Estimates of Incidence and Mortality Worldwide for 36 Cancers in 185 Countries. *CA: A Cancer Journal for Clinicians* 71, 209-249.

Syn, N.L., Teng, M.W.L., Mok, T.S.K., and Soo, R.A. (2017). De-novo and acquired resistance to immune checkpoint targeting. *The Lancet Oncology* 18, e731-e741.

Szalai, B., Subramanian, V., Holland, C.H., Alföldi, R., Puskás, L.G., and Saez-Rodriguez, J. (2019). Signatures of cell death and proliferation in perturbation transcriptomics data—from confounding factor to effective prediction. *Nucleic Acids Research* 47, 10010-10026.

Takayama, S., Ostuni, E., LeDuc, P., Naruse, K., Ingber, D.E., and Whitesides, G.M. (2001). Subcellular positioning of small molecules. *Nature* 411, 1016-1016.

Tarafdar, A., Hopcroft, L.E.M., Gallipoli, P., Pellicano, F., Cassels, J., Hair, A., Korfi, K., Jørgensen, H.G., Vetrie, D., Holyoake, T.L., *et al.* (2017). CML cells actively evade host immune surveillance through cytokine-mediated downregulation of MHC-II expression. *Blood* 129, 199-208.

Teng, M.W., Swann, J.B., Koebel, C.M., Schreiber, R.D., and Smyth, M.J. (2008). Immune-mediated dormancy: an equilibrium with cancer. *Journal of leukocyte biology* 84, 988-993.

Thiery, J.P. (2002). Epithelial–mesenchymal transitions in tumour progression. *Nature Reviews Cancer* 2, 442-454.

Tsamandouras, N., Chen, W.L.K., Edington, C.D., Stokes, C.L., Griffith, L.G., and Cirit, M. (2017). Integrated Gut and Liver Microphysiological Systems for Quantitative In Vitro Pharmacokinetic Studies. *AAPS J* 19, 1499-1512.

Unger, M.A., Chou, H.P., Thorsen, T., Scherer, A., and Quake, S.R. (2000). Monolithic microfabricated valves and pumps by multilayer soft lithography. *Science* 288, 113-116.

Untergasser, A., Nijveen, H., Rao, X., Bisseling, T., Geurts, R., and Leunissen, J.A.M. (2007). Primer3Plus, an enhanced web interface to Primer3. *Nucleic acids research* 35, W71-W74.

Utharala, R., Grab, A., Vafaizadeh, V., Peschke, N., Ballinger, M., Turei, D., Tuechler, N., Ma, W., Ivanova,

O., Gil Ortiz, A., *et al.* (2021). A microfluidic Braille valve platform for on-demand production, combinatorial screening and sorting of chemically distinct droplets. Submitted to Nature Protocols.

Utharala, R.C., Chawaree; Nögel, Lukas; Merten, Christoph A. (2016). Patent.

Vander Heiden, M.G., Cantley, L.C., and Thompson, C.B. (2009). Understanding the Warburg effect: the metabolic requirements of cell proliferation. *science* 324, 1029-1033.

Vollertsen, A.R., de Boer, D., Dekker, S., Wesselink, B.A.M., Haverkate, R., Rho, H.S., Boom, R.J., Skolimowski, M., Blom, M., Passier, R., *et al.* (2020). Modular operation of microfluidic chips for highly parallelized cell culture and liquid dosing via a fluidic circuit board. *Microsystems & Nanoengineering* 6, 107.

VR, P. (1958). The biochemical approach to the cancer problem. Paper presented at: Federation proceedings.

Waldmann, T.A. (2018). Cytokines in Cancer Immunotherapy. *Cold Spring Harb Perspect Biol* 10, a028472.

Wang, J., Fan, H.C., Behr, B., and Quake, Stephen R. (2012). Genome-wide Single-Cell Analysis of Recombination Activity and De Novo Mutation Rates in Human Sperm. *Cell* 150, 402-412.

Warburg, O.H. (1930). The metabolism of tumours: investigations from the Kaiser Wilhelm Institute for Biology, Berlin-Dahlem (Constable & Company Limited).

Watanakunakorn, C. (1984). Mode of action and in-vitro activity of vancomycin. *Journal of Antimicrobial Chemotherapy* 14, 7-18.

Whitesides, G.M. (2006). The origins and the future of microfluidics. *Nature* 442, 368-373.

Wiesner, T., Lee, W., Obenauf, A.C., Ran, L., Murali, R., Zhang, Q.F., Wong, E.W.P., Hu, W., Scott, S.N., Shah, R.H., *et al.* (2015). Alternative transcription initiation leads to expression of a novel ALK isoform in cancer. *Nature* 526, 453-457.

Wölfle, S.J., Strebovsky, J., Bartz, H., Sähr, A., Arnold, C., Kaiser, C., Dalpke, A.H., and Heeg, K. (2011). PD-L1 expression on tolerogenic APCs is controlled by STAT-3. *European Journal of Immunology* 41,

413-424.

Wonderlich, J., Shearer, G., Livingstone, A., and Brooks, A. (2006). Induction and Measurement of Cytotoxic T Lymphocyte Activity. *Current Protocols in Immunology* 72, 3.11.11-13.11.23.

Wong, A.H.H., Li, H.R., Jia, Y.W., Mak, P.I., Martins, R.P.D., Liu, Y., Vong, C.M., Wong, H.C., Wong, P.K., Wang, H.T., *et al.* (2017). Drug screening of cancer cell lines and human primary tumors using droplet microfluidics. *Scientific Reports* 7.

Wood, L.D., Parsons, D.W., Jones, S., Lin, J., Sjöblom, T., Leary, R.J., Shen, D., Boca, S.M., Barber, T., Ptak, J., *et al.* (2007). The Genomic Landscapes of Human Breast and Colorectal Cancers. *Science* 318, 1108.

Wu, Q., Liu, J., Wang, X., Feng, L., Wu, J., Zhu, X., Wen, W., and Gong, X. (2020). Organ-on-a-chip: recent breakthroughs and future prospects. *Biomed Eng Online* 19, 9-9.

Xia, Y., McClelland, J.J., Gupta, R., Qin, D., Zhao, X.-M., Sohn, L.L., Celotta, R.J., and Whitesides, G.M. (1997). Replica molding using polymeric materials: A practical step toward nanomanufacturing. *Advanced Materials* 9, 147-149.

Xu, C., Fu, H., Gao, L., Wang, L., Wang, W., Li, J., Li, Y., Dou, L., Gao, X., Luo, X., *et al.* (2014). BCR-ABL/GATA1/miR-138 mini circuitry contributes to the leukemogenesis of chronic myeloid leukemia. *Oncogene* 33, 44-54.

Yamawaki, T.M., Lu, D.R., Ellwanger, D.C., Bhatt, D., Manzanillo, P., Arias, V., Zhou, H., Yoon, O.K., Homann, O., Wang, S., *et al.* (2021). Systematic comparison of high-throughput single-cell RNA-seq methods for immune cell profiling. *BMC Genomics* 22, 66-66.

Yang, P.-M., Chou, C.-J., Tseng, S.-H., and Hung, C.-F. (2017). Bioinformatics and in vitro experimental analyses identify the selective therapeutic potential of interferon gamma and apigenin against cervical squamous cell carcinoma and adenocarcinoma. *Oncotarget* 8, 46145-46162.

Ye, C., Ho, D.J., Neri, M., Yang, C., Kulkarni, T., Randhawa, R., Henault, M., Mostacci, N., Farmer, P., Renner, S., *et al.* (2018). DRUG-seq for miniaturized high-throughput transcriptome profiling in drug discovery. *Nature Communications* 9, 4307.

Zhang, C., Tu, H.-L., Jia, G., Mukhtar, T., Taylor, V., Rzhetsky, A., and Tay, S. (2019). Ultra-multiplexed analysis of single-cell dynamics reveals logic rules in differentiation. *Science advances* 5, eaav7959.

Zheng, G.X.Y., Terry, J.M., Belgrader, P., Ryvkin, P., Bent, Z.W., Wilson, R., Ziraldo, S.B., Wheeler, T.D., McDermott, G.P., Zhu, J., *et al.* (2017). Massively parallel digital transcriptional profiling of single cells. *Nature Communications* 8, 14049.

Ziemnicka-Kotula, D., Xu, J., Gu, H., Potempska, A., Kim, K.S., Jenkins, E.C., Trenkner, E., and Kotula, L. (1998). Identification of a Candidate Human Spectrin Src Homology 3 Domain-binding Protein Suggests a General Mechanism of Association of Tyrosine Kinases with the Spectrin-based Membrane Skeleton. *Journal of Biological Chemistry* 273, 13681-13692.

Herewith I declare that I, Martine Ballinger, prepared this Ph.D. thesis:

Establishing microfluidics-based drug screening methods to determine drug sensitivities of cancer cells.

on my own and with no other sources and aids than quoted.

